ICFO – THE INSTITUTE OF PHOTONIC SCIENCES

DOCTORAL THESIS

Optomechanical resonators based on low dimensional materials

Author:
Slaven TEPSIC

Supervisor:
Dr. Adrian BACHTOLD

Quantum Nanomechanics

May 18, 2021

"Knowledge is the golden ladder over which we climb to heaven; knowledge is the light which illuminates our path through this life and leads to a future life of everlasting glory."

Mihajlo Idvorski Pupin's mother

ICFO – THE INSTITUTE OF PHOTONIC SCIENCES

Abstract

Mechanical resonators based on low dimensional materials have attracted a lot of attention due to their remarkable properties. Their ultra-low mass and high Q factors make them exceptional sensors, offering new possibilities in the studies of the material strength and the thermodynamic properties of low dimensional materials. The goal of this thesis is to shed light on the thermal and elastic properties of low dimensional materials across a wide temperature range.

The first part of the thesis is focused on the study of the temperature dependence of the stiffness of carbon nanotubes. By measuring the resonance frequency of singly clamped carbon nanotube resonators as a function of temperature, we can obtain information on the Young's modulus of the measured carbon nanotubes. We observe a relative shift of the Young's modulus over a large temperature range with a slope of $-(173 \pm 65)$ ppm/K, consistent with two different theoretical models based on the thermal dynamics of the lattice. The results show the dependence of the fundamental mechanical mode on the phonons in carbon nanotubes via the Young's modulus. The measured data also indicates the coupling between mechanical modes and the phonon thermal bath in nanotubes. The phonon thermal bath in our experiments likely operates in the Akhiezer limit.

In the second part of the thesis, we present the temperature dependence of the thermal conductivity and the specific heat capacity in the $MoSe_2$ monolayer in a larger temperature range. Both the thermal conductivity and the specific heat capacity measurements are consistent with predictions based on first-principles. The results show that the phonon transport in a $MoSe_2$ monolayer can be both diffusive and ballistic, depending on the temperature of the monolayer. The method used in this measurement can be used to investigate the thermal properties of many two-dimensional materials. Furthermore, it opens the possibility to investigate interesting thermal transport regimes in two-dimensional materials like hydro-dynamic regime or anomalous heat conduction.

ICFO – THE INSTITUTE OF PHOTONIC SCIENCES

Abstracto

Los resonadores mecánicos basados en materiales de baja dimensionalidad han llamado la atención de la comunidad científica debido a sus singulares propiedades. Su pequeña masa y sus altos factores de calidad (Q) los convierten en sensores excepcionales, ofreciendo un nuevo abanico de posibilidades en el estudio de las propiedades mecánicas y termodinamicas de los materiales de baja dimensionalidad. El objetivo de ésta tesis es el estudio de las propiedades térmicas y elásticas de los materiales de baja dimensionalidad en un amplio rango de temperaturas.

La primera parte de la tesis se centra en la evolución de la rigidez de los nanotubo de carbono en función de la temperatura. La medida de la frecuencia de resonancia de un resonador basado en un nanotubos de carbono con un único punto de anclaje en función de la temperatura, ofrece información sobre el módulo de Young de dicho nanotubo. Observamos un cambio relativo del módulo de Young en un amplio rango de temperaturas con una pendiente de $-(173 \pm 65)$ ppm/K, en acuerdo con dos modelos teóricos diferentes basados en la dinámica térmica de la red cristalina del material. Los resultados muestran la influencia de los fonones del nanotubo de carbono en el modo mecánico fundamental a través del módulo de Young. Los datos también indican el acoplamiento entre los modos mecánicos y el baño térmico de fonones en los nanotubos. Es probable que el baño térmico de fonones en nuestros experimentos opere en el límite de Akhiezer.

En la segunda parte de la tesis, presentamos la evolución de la conductividad térmica y la capacidad calorífica específica de una monocapa $MoSe_2$ en función de la temperatura para un rango más amplio. Tanto la conductividad térmica como las medidas de la capacidad calorífica específica concuerdan con las predicciones basadas en los primeros principios. Los resultados muestran que el transporte de fonones en la monocapa $MoSe_2$ puede ser difusivo o balístico, dependiendo de la temperatura de dicha monocapa. El método utilizado en esta medida se puede utilizar para investigar las propiedades térmicas de muchos materiales bidimensionales. Asimismo, abre la posibilidad de investigar distintos regímenes de transporte térmico en materiales bidimensionales cómo el régimen hidrodinámico o la conducción de calor anómala.

Acknowledgements

First, I would like to thank my thesis advisor, Prof. Adrian Bachtold, for giving me the opportunity to do my PhD in his group. He gave me an amazing possibility to work in a highly motivating environment. He was very patient with me and taught me to never give up. I would like to thank Prof. Peter Steeneken, Prof. Ho Bun Chan, and Prof. Frank Koppens for accepting to be part of my thesis committee. I would also like to thank Prof. Javier García de Abajo and Prof. Stephan Roche for agreeing to serve as substitute members.

I would like to thank Antoine Reserbat-Plantey, who was my mentor for a brief time at the beginning of my PhD. He introduced me to the world of optomechanics and gave me the necessary theoretical and practical knowledge needed for my further research. To Nicolás Morell with whom I worked closely during the first half of my PhD, who gave me a lot of motivation and knowledge.

Further, I greatly enjoyed working with Gernot Gruber and Christoffer Møller. Their guidance and positive attitude greatly contributed to my professional development. I thank them both for their extensive comments on this thesis.

Pierre Verlot, thank you for all your time and patience and for answering all the questions I had as a young PhD student. You were an irreplaceable teacher to me.

Overall, I am grateful to all past and present members of the group. Carles Urgell, Sergio de Bonis, Parmeshwar Prasad, Chandan Samanta, Roger Tormo Queralt, Lorenzo Vistoli, Wei Yang and Jil Schwender thank you for the wonderful company, for precious moments at group excursions and fruitful discussions.

Finally, I want to thank my family. Slavica and Sinisa, you were always by my side, giving me much-needed encouragement. And Milica, thank you for bringing a lot of happiness into my life.

Contents

To my family...

Chapter 1

Introduction

1.1 Nanotechnology

Nanotechnology is a term used to describe science, technology, and engineering that is focused on manipulating, understanding, and controlling matter on molecular and atomic scales.

The concept of nanotechnology goes back to 1959 when acclaimed physicist Richard Feynman gave his, now famous, talk *There is Plenty of Room at the Bottom*. In his talk, he described the possibility of manipulating individual atoms and molecules to perform synthesis. The actual term nanotechnology was used for the first time in 1974 by Norio Taniguchi when he described the process of thin-film deposition and ion beam patterning with nanometer precision. Two major achievements pushed nanotechnology into the modern era: the scanning electron microscope in 1981 by Gerd Binnig and Heinrich Rohrer and the discovery of fullerenes in 1985 by Harry Kroto, Richard Smalley, and Robert Curl. The scanning electron microscope provided an unprecedented tool for the visualization and manipulation of individual atoms. The discovery of fullerenes led to the discovery of carbon nanotubes with potential applications in nanoscale electronics and devices.

Nowadays, the imaging and manipulation of matter at the nanoscale have become a standard discipline around the world and many techniques for manipulation and imaging at the nanoscale have been developed. Notable examples include scanning tunneling and scanning electron microscopy, atomic force microscopy, electron- and ion-beam lithography, and molecular beam epitaxy. With the improved level of control, industries are

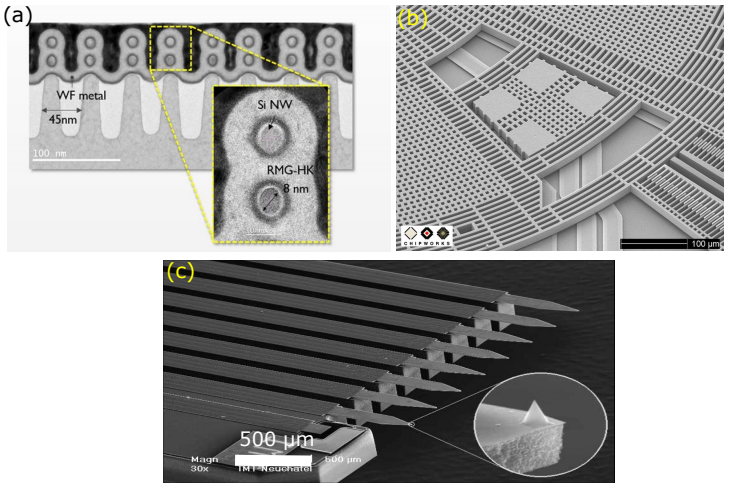

FIGURE 1.1: (a) Imec demonstrated field effect transistors with lateral silicon nanowires in the gate-all-around configuration. [1] (b) Part of the gyroscope chip used in various devices. [2] (c) Eight sharp tips of the NASA's Phoenix Mars Lander's AFM sent to Mars. [3]

pushing the boundaries of nanoscale systems. A prime example of this is the commercially available microprocessors manufactured using extreme ultraviolet lithography, which contain transistors with features of only 5 nm (Fig. 1.1a).

Another field where nanomechanical systems get a lot of attention is in sensing applications where they are routinely employed to measure force, charge, and mass. Nanomechanical resonators are especially well suited for sensing applications due to their low mass and high sensitivity. Miniaturization in these systems has led to higher sensitivity to external forces acting on them. Smaller dimensions have also enabled more integration with other devices, which has led to many industrial applications such as gyroscopes (see Fig. 1.1b), accelerometers, and blood sensors in hospitals.

1.2 Low dimensional materials as nanomechanical resonators

Mechanical resonators based on low dimensional materials have recently attracted considerable attention. In particular, two dimensional materials such as monolayers made of transition metal dichalcogenides (TMD) [4–6] and graphene [7–18] and one dimensional materials such as carbon nanotubes [19–30] and semiconducting nanowires [31–38]. Common to all these systems is their low mass, which makes them fantastic sensors of external forces and adsorbed mass [23, 25, 29, 39]. They have been successfully used in many different research fields such as surface science [37, 38, 40, 41], nano-magnetism [42, 43] and light-matter interaction [34].

Thermoelasticity Thermoelastic properties of materials are important when designing various mechanical structures. This includes large industrial structures such as spacecrafts [44] and nuclear plants [45], as well as modern, state-of-the-art nano- and micro-mechanical devices. In small structures, a rich set of properties has caught the interest of the research community like dissipation [46, 47], fluctuations [48, 49] and torque generation [50, 51]. Fundamentally, the thermal behavior of the stiffness of materials emerges from the complicated interactions of binding energy and lattice dynamics and it is quantified by the Young's modulus. **In this thesis** the Young's modulus of carbon nanotubes is investigated from room temperature down to a few Kelvins.

Thermal transport Heat transport is of interest in both industrial applications and fundamental research. One of the major challenges in industrial systems is the dissipation of heat. The heat generated by computer processors becomes increasingly important with higher transistor densities and clock speeds. The inability to properly dissipate the heat in processors has led to saturation in processor clock speed in recent years. This makes the study of thermal propagation in nanoscale devices very important for future miniaturization. Furthermore, fundamental aspects of heat propagation are also important to investigate. At low temperatures, heat transport can enter into interesting regimes such as transport without dissipation, called ballistic

transport [52–54] or the phonon hydrodynamic regime that has been predicted for two-dimensional materials [55, 56]. **In this thesis** a mechanical resonator based on TMD monolayer is used to investigate heat transport in two-dimensional materials.

1.3 Thesis motivation and outline

In this thesis, we used low dimensional materials to fabricate nanomechanical resonators and to study their thermodynamic and mechanical properties. First, we use the exquisite sensing capabilities of cantilevers made of carbon nanotubes to investigate the thermal behavior of their stiffness. Second, we investigate thermal transport in 2D materials over a large temperature range.

The structure of the thesis is as follows:

- Chapter 2 gives a brief introduction to the optical and mechanical properties of low dimensional materials such as graphene, TMD monolayer, and carbon nanotubes.
- Chapter 3 introduces the main theoretical concepts needed to understand linear and nonlinear resonators, as well as basic optomechanical concepts.
- Chapter 4 details the fabrication process of hybrid optomechanical resonators based on carbon nanotubes.
- Chapter 5 details the study of the thermal behavior of carbon nanotube Young's modulus.
- Chapter 6 presents the study of the thermal properties of TMD monolayers over a large temperature range.

Chapter 2

Low dimensional Materials

In this chapter, we will give a brief introduction to the physical properties of graphene, carbon nanotubes, and TMDs. We describe their mechanical and optical properties which arise from their unique crystallographic structure.

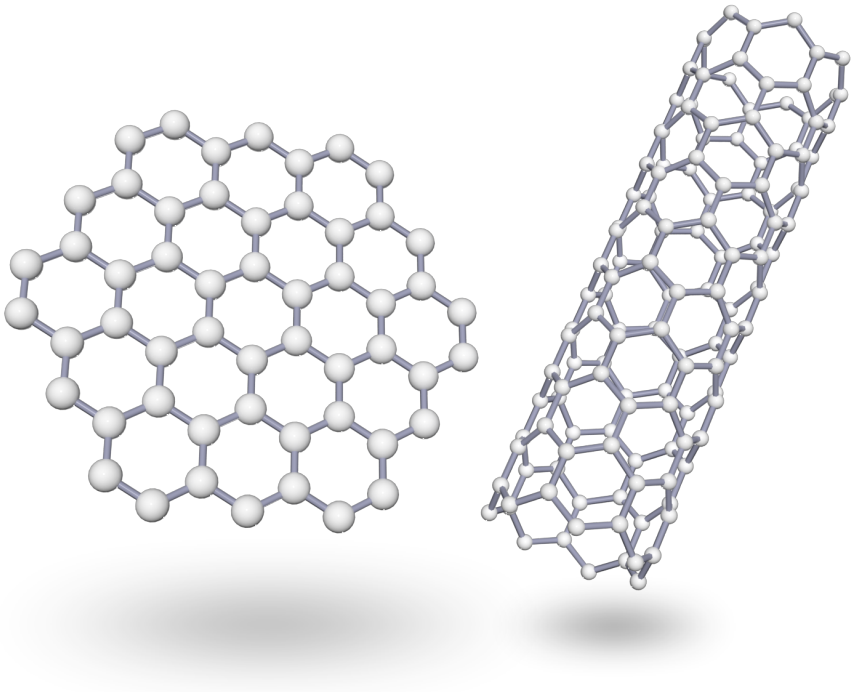

FIGURE 2.1: Visualisation of graphene hexagonal lattice (left) and carbon nanotube (right).

2.1 Carbon Nanotubes

2.1.1 Graphene

The discovery of graphene by Andre Geim and Konstantin Novoselov in 2004 brought a huge impact on research activities in 2D materials [57] and was rewarded with the Nobel prize in 2010. In the first experiments, they demonstrated interesting mechanical and electrical properties of graphene. Recently, twisted bilayer graphene has attracted attention in the scientific community because of the discovery of superconductivity in this system [58].

Graphene is a two-dimensional sheet of carbon atoms arranged in a hexagonal lattice. Graphene is the basic building block of most other carbon allotropes (see Fig. 2.2). The extraordinary mechanical, thermal, optical, and electrical properties of graphene come from the unique electronic structure of the carbon atom [59]. Carbon has four covalent electrons, occupying the 2s, $2p_x$, $2p_y$, $2p_z$ orbitals. Each carbon atom forms 3 sp^2 in-plane covalent, so-called, σ-bonds with the neighbouring atoms. The bond length is 1.42 Å and the angle between the bonds is 120°. These strong bonds give graphene its enormous mechanical strength.

The $2p_z$ orbital of each atom is orthogonal to the lattice plane and forms the electronic π-bonds of the crystal.

In 3D graphite, the spacing between the graphene layers is 3.35 Å.

2.1.2 From Graphene to Carbon Nanotubes

Already before the discovery of graphene, carbon nanotubes have been an object of intense research after their experimental discovery by Iijima et al. (1991) [60]. Single-wall carbon nanotubes can be seen as a single layer of graphene rolled up into a tube. Usually, we denote them as 1D objects with axial symmetry. Properties of carbon nanotubes depend on their chirality, which represents the difference between the orientation of the graphene lattice and the nanotube axis. We define the chiral vector as

$$\mathbf{C_h} = n_1\mathbf{a_1} + n_2\mathbf{a_2}.$$

The integer pair (n_1, n_2) uniquely determines the type of the nanotube. Special cases are armchair nanotubes, where $n_1 = n_2$

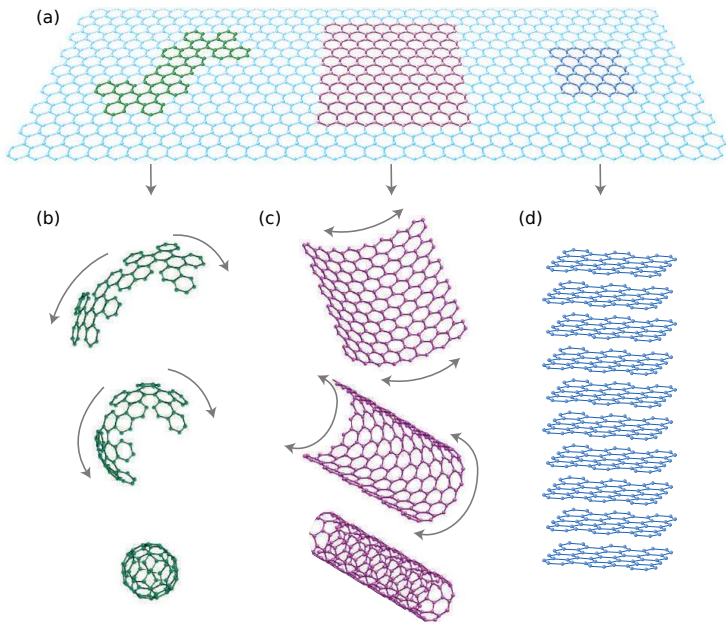

FIGURE 2.2: Graphene is the basic building block of other carbon materials with different dimensionality. (a) 2D graphene lattice, (b) 0D fullerene, also called buckyball, (c) 1D carbon nanotube, (d) graphene layer stacked in 3D graphite. Figure adapted from [57].

and zig-zag nanotubes, where $n_2 = 0$. All other nanotubes are called chiral nanotubes. An illustration of different nanotubes is shown in the Fig. 2.3.

The mechanical properties of carbon nanotubes are remarkable. The hybridized sp^2 bonds between carbon atoms are so strong that the intrinsic strength exceeds any other material [62]. Their very low mass density, high chemical stability, and mechanical strength make them an excellent choice for the implementation of various mechanical resonators [28, 63–65].

In addition to single-walled carbon nanotubes, there are also multi-walled carbon nanotubes. A multi-wall carbon nanotube can be seen as concentric single-walled carbon nanotubes stacked together, possibly with different chiralities. Multi-wall carbon nanotubes typically have a larger diameter and length when compared to single wall CNTs [66].

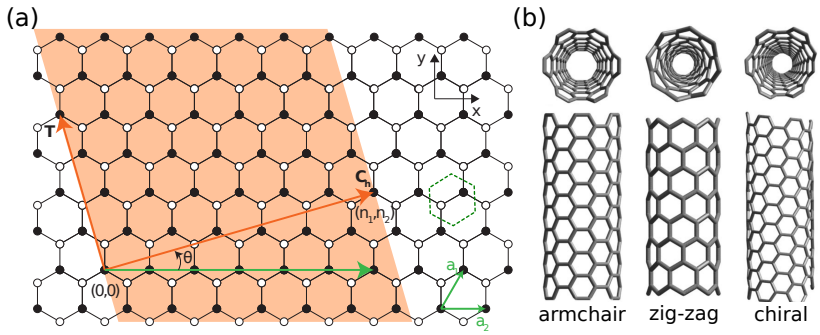

FIGURE 2.3: (a) Single wall carbon nanotube is defined by the chirality vector $\mathbf{C_h}$ and the translation vector $\mathbf{T}$. The unit cell (green dashed hexagon) is determined by the two lattice vectors $\mathbf{a_1}$ and $\mathbf{a_2}$ and contains two atoms. (b) The three geometric classes of carbon nanotubes, armchair (n, n), zigzag $(n, 0)$ and chiral (n_1, n_2). Adapted from [61]

2.2 Monolayer transition metal dichalcogenides

Transition metal dichalcogenides (TMDs) are a class of layered materials of significant interest due to their thickness-dependent electrical and optical properties. Similar to graphite, TMD bulk crystals are formed by monolayers bound to each other by van der Waals forces. New physical properties emerge when a bulk crystal of a macroscopic dimension is thinned down to the atomic layer.

Fabrication methods of single-layer TMDs include exfoliation, chemical vapor deposition (CVD), and molecular beam epitaxy. Exfoliation represents a top-down approach, that is usually not compatible with industrial processes. This technique usually produces high-quality samples that have a small size [68]. The CVD technique for growth introduces more complexity and expensive equipment, but it is often used to produce much larger monolayers compared to mechanical exfoliation [69, 70].

The general type of these monolayers is MX_2, where M is a transitional metal atom (W, Mo, etc.) and X is a chalcogen atom (Se, S, or Te). One layer of M atoms is sandwiched between two layers of X atoms as seen on 2.4. The thickness of a single layer of a TMD is calculated based on the interlayer separation in the bulk material and its value is $t \approx 0.6\,\text{nm}$. Due to their 2D nature, TMD monolayers are naturally very light. This makes

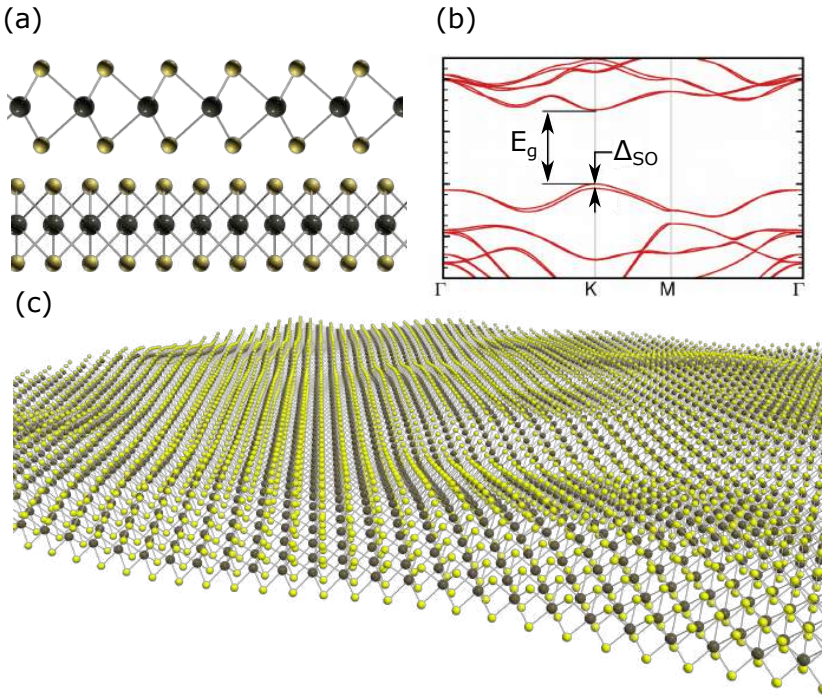

FIGURE 2.4: (a) Cross-section and (b) typical band structure of a TMD monolayer. It shows the valence band splitting due to spin-orbit coupling Δ_{SO} as well as the direct band gap E_g. (c) Visualisation of a TMD lattice. Adapted from [67]

them great candidates when designing mechanical resonators for sensing applications. For example, nanomechanical systems have successfully been used in mass sensing applications [23]. The smallest detectable adsorbed mass on the mechanical resonator is given by [39]:

$$\delta m = 2m_{\text{eff}}\frac{\delta f}{f_{\text{m}}}, \tag{2.1}$$

where m_{eff} is the effective mass of the resonator, f_0 is resonance frequency and δf is the frequency noise of the resonator. We can see that the mass resolution δ_{m} is directly proportional to the effective mass of the resonator.

The Young's modulus and strain are important parameters in the context of mechanical resonators. The Young's modulus gives the ratio between strain and stress in the material. The

Young's modulus of WSe_2 is $E_{WSe_2} = 116\,\mathrm{Nm}^{-1}$ and for $MoSe_2$ it is $E_{MoSe_2} = 104\,\mathrm{Nm}^{-1}$ [71]. They also exhibit high in-plane strength as TMD monolayers can be strained up to 20 % before breaking [72, 73]. By controlling the tension in the resonator we can change the resonance frequency of the mechanical resonator. In a drum-like resonator, this can be achieved by applying a voltage between the monolayer and the back gate. Another way would be to cool the resonator so that the thermal contractions change the tension in the monolayer and therefore the resonance frequency of the resonator.

Unlike a single sheet of graphene, TMDs are semiconductors with a direct bandgap at the K point (Fig. 2.4b). The bandgap of TMD monolayers is in the range of 600-1500 nm [74].

When a photon of a specific wavelength is absorbed in a TMD monolayer, an electron is created in the conduction band and a hole in the valence band. These two particles with opposite charge are attracted by the *Coulomb* interaction and they form a bound state called an exciton [75]. The excitons are well known in traditional semiconductors (like GaAs or ZnO), but in TMD monolayers their binding energy is much larger. The large binding energy is explained by the dielectric screening and the confinement of electrons within the monolayer and the resulting electron screening that is weaker than that in 3D systems. [76–79].

These excitons greatly increase the absorption of light in TMD monolayers. The absorption of the TMD monolayer is in the range of 5-10 % for white light but can be as high as 20 % at 561 nm [80], which is unprecedented for such thin material.

In photoluminescence (PL) experiments, the recombination of the excited electron and the hole in the TMD monolayer emits a photon that corresponds to the exciton energy. In TMD multilayers, because of their indirect bandgap, photoluminescence is reduced by several orders of magnitude [81]. This effect enables us to distinguish between TMD monolayers and multilayers with great accuracy.

Chapter 3

Nanomechanics and Optomechanics

In this chapter, we will introduce some basic concepts of nanomechanics that are necessary to understand the dynamical properties of resonators at the nanoscale. We will begin with the simple model of a linear harmonic resonator. We will then investigate its response to incoherent fluctuating thermal forces. Next, we will discuss nonlinear vibrations. Finally, we will discuss optomechanical effects in the resonators.

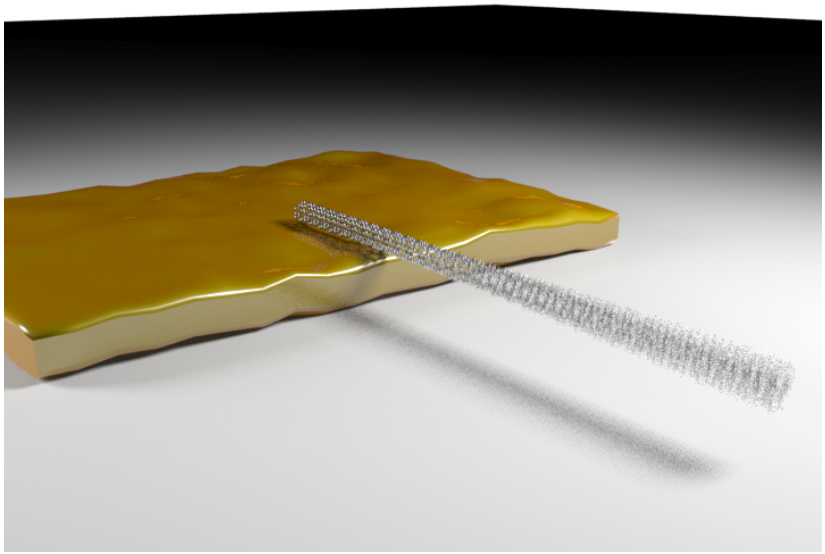

FIGURE 3.1: Visualisation of a single clamped carbon nanotube resonator.

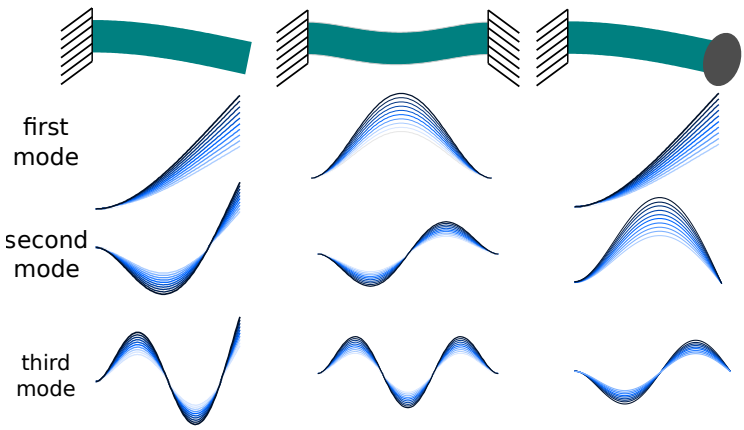

FIGURE 3.2: Schematic of the first three flexural modes of a single clamped beam (left), a doubly clamped beam (middle) and single clamped beam with extra mass at the free end (right). Adapted from [83].

3.1 Introduction

To make modern nano- and micro-resonators, engineers use a wide variety of different materials and geometries, from single- and doubly-clamped beams, drums made out of single-layer 2D nanomaterials, like graphene and TMDs, to more complicated and highly integrated systems. The simplest model to describe the properties of these systems is the damped harmonic oscillator. A harmonically oscillating system is described by a linear relationship between its restoring force and displacement [82]. By solving the Euler-Bernoulli equation for mechanical resonators, we can obtain the set of orthogonal eigenmodes, where each one has a distinct eigenfrequency and mode shape (see Fig. 3.2). For a small subset of simple geometries, we can calculate analytical solutions, but for the geometrically more complex systems, finite-element simulations can be used to obtain the eigenfrequencies and eigenshapes. Analytical solutions can also be found for carbon nanotube resonators by treating them as one-dimensional strings and for drum-like resonator made of TMDs by treating them as two-dimensional membranes.

3.2 Linear driven oscillator

The equation of motion of a damped harmonic oscillator driven by a time-dependent force $F(t)$ is given by

$$m_{\text{eff}}\frac{d^2x(t)}{dt^2} + m_{\text{eff}}\gamma_{\text{m}}\frac{dx(t)}{dt} + kx(t) = F(t) \tag{3.1}$$

where the constant γ_{m} represents the linear mechanical dissipation rate, k is the mechanical spring constant, m_{eff} is effective mass and $x(t)$ is the position as a function of time t. $F(t)$ represents any external time dependent force which can be a random noise force or a coherent oscillating force. From here we can define the undamped angular resonance frequency as

$$\omega_0 = \sqrt{\frac{k}{m_{\text{eff}}}}, \tag{3.2}$$

which is determined by the elastic properties, the mass and the boundary conditions of the system. Both ω_0 and γ_{m} are given in radial units. When presenting the experimental data in this thesis, the ordinary frequency $f_0 = \frac{\omega_0}{2\pi}$ will be used, expressed in Hz units.

Interaction of the mechanical resonator with the environment is characterised by the term $m_{\text{eff}}\gamma_{\text{m}}\frac{dx(t)}{dt}$ in Eq. 3.1, where γ_{m} defines the rate of the energy exchange between them. The Q factor is a dimensionless figure of merit that quantifies the damping of the system. The Q factor is defined by

$$Q = 2\pi\left(\frac{\text{Total energy}}{\text{Energy lost in one cycle}}\right). \tag{3.3}$$

In the limit of a small damping rate, $\gamma_{\text{m}} \ll \omega_0$, the Q factor simplifies to $Q = \omega_0/\gamma_{\text{m}}$. This number essentially represents the number of oscillations before the system loses its energy to the environment. This gives us the characteristic decay time τ of the resonator as $\omega_0\tau = 1/Q$.

Quite often it is convenient to convert equations in the frequency domain. If we perform Fourier transform of Eq. 3.1 we get

$$x(\omega) = \chi(\omega)F(\omega) \tag{3.4}$$

The expression describes how the force $F(\omega)$ gives rise to a linear

mechanical response $x(\omega)$, where χ is the mechanical susceptibility and is given by

$$\chi(\omega) = \frac{1}{m_{\text{eff}}[\omega_0^2 - \omega^2 - i\gamma_{\text{m}}\omega]}. \tag{3.5}$$

To measure susceptibility, we usually measure the power spectral density spectrum $S_{xx}(\omega)$ of a time-varying signal $x(t)$. The power spectral density gives us the distribution of power in the frequency space of the measured signal $x(t)$. The Wiener-Khinchin theorem states that the power spectral density of $x(t)$ is given by the Fourier transform of the autocorrelation of $x(t)$

$$S_{xx}(\omega) = \int_{-\infty}^{\infty} d(\tau) \left\langle x(t)x^*(t-\tau)\right\rangle e^{-\omega\tau}, \tag{3.6}$$

where <...> represents statistical mean. The variance of the measured signal $x(t)$ is the area under one-sided power spectral density

$$\left\langle x^2\right\rangle = \frac{1}{2\pi}\int_0^{\infty} d\omega S_x(\omega) = \int_0^{\infty} df S_x(f). \tag{3.7}$$

If the Fourier transform of the signal is $x(\omega)$, from 3.6, we get

$$S_{xx}(\omega) = \left\langle x(\omega)x(-\omega)\right\rangle. \tag{3.8}$$

From 3.8 and 3.4 we get

$$S_{xx}(\omega) = |\chi(\omega)|^2 S_{FF}(\omega), \tag{3.9}$$

where the S_{FF} is the power spectral density of the force noise acting on the resonator.

3.2.1 Thermal motion in carbon nanotube resonators

The coupling of the mechanical resonator with its environment leads to the dissipation of the energy quantified by the damping of the system. In other words, the resonator exchanges energy with the thermal bath. This coupling also leads to the thermal force, which is a random fluctuating force $\delta F^{th}(t)$. This force acts on the resonator, which leads to thermal or Brownian motion. This phenomenon is described by the fluctuation-dissipation theorem, which relates the fluctuations of the physical system

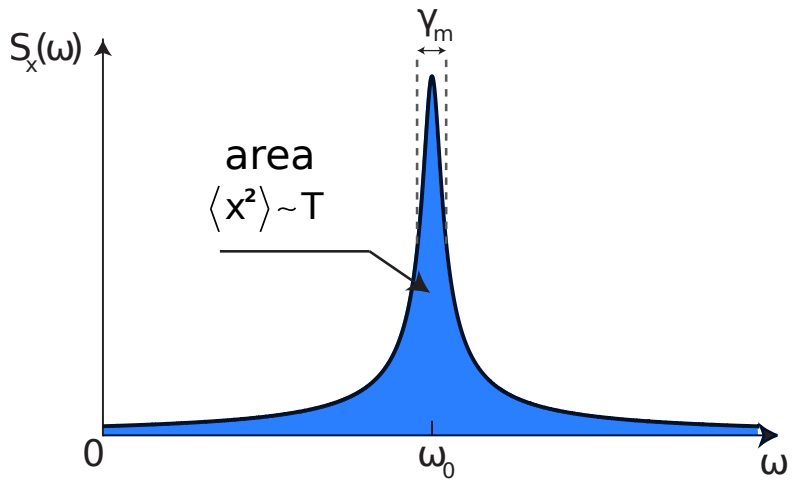

FIGURE 3.3: The area under the displacement power spectral density is proportional to the temperature of the mechanical mode. Adapted from [84].

in thermal equilibrium to the dissipative part in the equation of motion (Eq. 3.1) of the mechanical resonator. Following linear response theory [82], we can obtain the single-sided thermal force noise power spectral density

$$S_F^{\text{th}}(\omega) = -\frac{4k_B T}{\omega} Im\left(\frac{1}{\chi(\omega)}\right), \tag{3.10}$$

where k_B is the Boltzmann constant and T is the temperature. In the limit of weak damping, $\gamma_m \ll \omega_0$, this equation becomes

$$S_F^{\text{th}}(\omega) = 4m_{\text{eff}}\gamma_m k_B T. \tag{3.11}$$

The spectrum of the thermal noise is white and depends only on the bath temperature T, dissipation rate γ_m and the effective mass of the resonator m_{eff}. The result resembles the Johnson-Nyquist noise [85] of voltage fluctuations across an electrical resistor. Now, using the Eq. 3.11 we get the thermal power spectral density of the mechanical resonator

$$S_x^{\text{th}}(\omega) = \frac{4\gamma_m k_B T}{m_{\text{eff}}[(\omega_0^2 - \omega^2)^2 + (\gamma_m^2\omega^2)]]}. \tag{3.12}$$

We can use this equation to relate the variance of the displacement and the temperature of the thermal equilibrium. From the equipartition theorem we get

$$\frac{1}{2}m_{\text{eff}}\left\langle \dot{x}_{\text{th}}^2 \right\rangle = \frac{1}{2}k\left\langle x_{\text{th}}^2 \right\rangle = \frac{1}{2}k_{\text{B}}T. \tag{3.13}$$

Using the last equation and $k = m_{\text{eff}}\omega^2$ we obtain

$$\left\langle x_{\text{th}}^2 \right\rangle = \frac{k_{\text{B}}T}{m_{\text{eff}}\omega_0^2}. \tag{3.14}$$

Further, from Eq. 3.7 we get that the variance of the displacement is equal to the area under the single-sided displacement spectrum

$$\left\langle x_{\text{th}}^2 \right\rangle = \int_0^\infty \frac{1}{2\pi} d\omega S_x(\omega) = \frac{k_{\text{B}}T}{m_{\text{eff}}\omega_0^2} \tag{3.15}$$

This result is illustrated in Fig. 3.3

3.2.2 Duffing oscillator

So far we only looked at the harmonic oscillator model where there is a linear relationship between force and position, obeying Hooke's law. For most systems, this is a very good approximation, because most of the materials used in these systems can sustain very large displacements before the linear relation breaks down. However, at large displacement amplitudes, nonlinearities in the restoring force have to be taken into account. These forces find their origin in geometrical nonlinearities or nonlinear external potentials [87, 88]. In general, nonlinearities are not desirable in practical applications, because they tend to decrease the dynamic range of the system [89]. To model this behaviour, we add a restoring force term that is proportional to the cube of the displacement into the equation of motion. This is called the Duffing oscillator model and is written as

$$m_{\text{eff}}\frac{d^2x(t)}{dt^2} + kx(t) + m_{\text{eff}}\gamma_{\text{m}}\frac{dx(t)}{dt} + \alpha x(t)^3 = F(t), \tag{3.16}$$

where α is Duffing nonlinear coefficient. Solving this equation gives us the displacement amplitude.

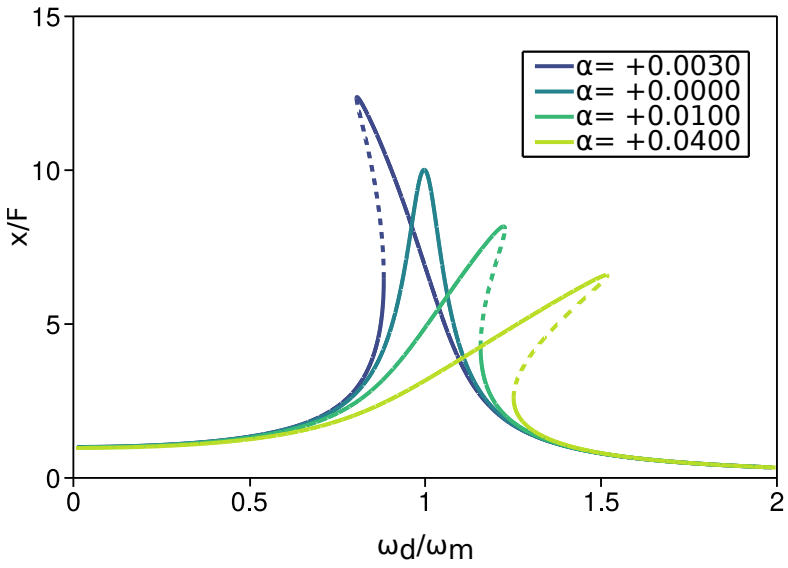

FIGURE 3.4: Frequency response x/F as a function of ω_d/ω_m for the Duffing equation for different value of Duffing coefficient. The dashed parts of the frequency response are unstable. [86]

$$x(\omega_d) = \frac{F_0/m_{eff}}{\sqrt{\left(\omega_0^2 + \frac{3}{4}\alpha x(\omega_d)^2 - \omega_d^2\right)^2 + \gamma_m^2\omega_d^2}} \tag{3.17}$$

The nonlinear amplitude is illustrated in the Fig. 3.4. At low drive force, the amplitude scales linearly with the driving force. Exceeding a critical amplitude, we get into a regime where the displacement amplitude equation $x(\omega_d)$ has three solutions out of which only two are stable. This leads to bistable behaviour, where the amplitude is oscillating between the two stable solutions. As we increase the driving force the resonance frequency shifts towards a higher or lower value based on the sign of the Duffing constant α (see Fig. 3.4). This frequency shift from the mechanical resonance frequency ω_m can be calculated using

$$\Delta\omega = \frac{3}{8}\frac{\alpha_{eff}}{m_{eff}\omega_m} z_{max}^2. \tag{3.18}$$

3.3 CNT as single clamped resonators

The Euler-Bernoulli partial differential equation (PDE) that describes the motion $y(x,t)$ of a vibrating beam is

$$\frac{\partial^2 y}{\partial t^2} + \frac{YI}{\rho A}\frac{\partial^4 y}{\partial x^4} = 0, \tag{3.19}$$

where Y is the Young's modulus, I is the beam's banding moment, A is the cross-sectional area, ρ is the density and l is the length of the resonator (see Fig. 3.5). The solution of Eq. 3.19 can be represented in the form of pure cosine (and sine) waves $y(x,t) = A\cos(\alpha x - \omega t)$. From here we obtain the dispersion relation as

$$\omega_0 = \sqrt{\frac{YI}{\rho A}}\alpha^2. \tag{3.20}$$

The nonlinear relation between the wavevector α and the frequency ω means that the waveform phase velocity is now a function of the frequency. The effect of this is that an arbitrary waveform (one that is not sinusoidal) will change shape as it propagates. The general solution of Eq. 3.19 is

$$y(x,t) = \cos\omega_n t\left[a\cos\alpha_n x + b\sin\alpha_n x + c\cosh\alpha_n x + d\sinh\alpha_n x\right], \tag{3.21}$$

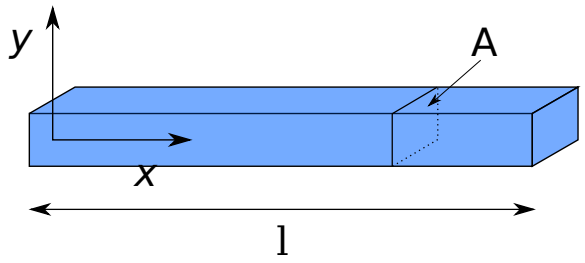

FIGURE 3.5: A beam of length L with transverse displacement $y(x)$.

where the radial frequency of mode n is $\omega_n = \sqrt{\frac{YI}{\rho A}}{\alpha_n}^2$, α_n are the wave numbers whereas a, b, c, d are constants that will be determined by satisfying the boundary conditions. Four boundary conditions are necessary to solve the equation.

The first example is a beam that is clamped only at one end and free at the other end. The boundary conditions, in this case, are given by

$$\left.\begin{aligned} y\,|_{x=0} &= 0, \\ \partial y/\partial x\,|_{x=0} &= 0, \\ \partial^2 y/\partial x^2\,|_{x=l} &= 0, \\ \partial^3 y/\partial x^3\,|_{x=l} &= 0. \end{aligned}\right\} \tag{3.22}$$

Using these boundary conditions and the general solution (Eq. 3.21) we obtain a discrete set of frequencies that satisfy the equation

$$\cos \alpha_n l \cosh \alpha_n l + 1 = 0. \tag{3.23}$$

The zeros of this function can be found numerically, with $\alpha_n l = 1.875, 4.694, 7.855, 10.996 \ldots$. In Fig. 3.2 we display the first three modes for this problem.

3.3.1 Cantilever with an added mass at the free end

In the presence of a particle with mass m_{bead} at the free end of a cantilever beam, the boundary conditions to satisfy become:

$$\left.\begin{aligned} y\,|_{x=0} &= 0, \\ \partial y/\partial x\,|_{x=0} &= 0, \\ \partial^2 y/\partial x^2\,|_{x=l} &= 0, \\ -YI\left.\frac{\partial^3 y}{\partial x^3}\right|_{x=l} &= m_{\mathrm{bead}} c^2 {\alpha_n}^4 y_{x=l}, \end{aligned}\right\} \tag{3.24}$$

in which the effect of the bead's rotary inertia is neglected [90]. Implementing these conditions in Eq. 3.21 leads to the following characteristic equation

$$\begin{aligned} &\cos \Omega_n \cosh \Omega_n + 1 \\ &\quad + m^* \Omega_n \left(\sinh \Omega_n \cos \Omega_n - \sin \Omega_n \cosh \Omega_n\right) = 0, \end{aligned} \tag{3.25}$$

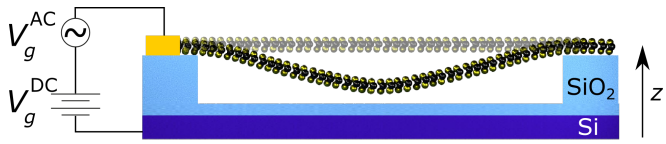

FIGURE 3.6: Cross section of a circular resonator based on the TMD monolayer. Adapted from [91].

where the eigenvalues $\Omega_n = \alpha_n l$ are solutions of Eq. 3.25 with $m^* = m_{bead}/m_{beam}$. The eigenmodes associated with the eigenvalues can then be obtained as

$$\Phi_n(x) = \cos(\Omega_n x) - \cosh(\Omega_n x) - \frac{\cos(\Omega_n) + \cosh(\Omega_n)}{\sin(\Omega_n) + \sinh(\Omega_n)}(\sin(\Omega_n x) - \sinh(\Omega_n x)). \quad (3.26)$$

Figure 3.2 shows the first three eigenmodes where $m^* = 20$. When the ratio between the mass of the bead at the free end and the mass of the beam becomes large, the mode shapes approach those of a beam clamped at one end and hinged at the other. The profile of the fundamental eigenmode is basically unchanged when increasing m^*, in contrast to what happens for the other eigenmodes. The influence of the mass of the bead at the free end is further discussed in the chapter A.1.1.

3.4 TMD as a circular resonator

TMDs can be used to make drum-like circular resonators with a metallic backgate [13, 92]. If we apply the voltage difference V_g between the membrane and the back gate it will create a force that can bend the elastic membrane (see Fig. 3.6). This capacitive force F_{el} can be modelled as

$$F_{el} = \frac{1}{2}\frac{dC}{dz}\left(V_g + \Delta\phi\right)^2, \quad (3.27)$$

where $\Delta\phi$ is the work function difference and C is the capacitance between the membrane and the gate. We can apply a DC or AC voltage, which can be used to bend or electrically drive the resonator when the oscillating voltage is around the resonance

frequency of the resonator. In the small signal approximation, $V_g^{AC} \ll V_g^{DC}$ the force can be written as

$$F_{el}(f) = \frac{1}{2}\frac{dC}{dz}\left(V_g^{DC} + V_g^{AC}(f) + \Delta\phi\right)^2 \approx \frac{dC}{dz}V_g^{DC}V_g^{AC}(f). \tag{3.28}$$

By applying a DC voltage, we can statically bend the membrane, which introduces tension in the membrane and changes its resonance frequency. If we assume that the membrane is well clamped along the edge and that the membrane is under initial tension (these are good assumptions for the device described later in this thesis) we can describe the resonance frequency as

$$f_0 = \frac{1}{2\pi}\sqrt{\frac{4.92E_{2D}}{m_{eff}}\epsilon - \frac{\varepsilon_0}{d^3}\frac{0.271\pi R_0^2}{m_{eff}}\left(V_g^{DC} + \Delta\phi\right)^2}, \tag{3.29}$$

where E_{2D} is the 2D young modulus of the TMD membrane, m_{eff} is the effective mass, ϵ is the initial strain, R_0 is the drum diameter, ε_0 is the vacuum permitivity and $d = d_{air}/\epsilon_0 + d_{SiO_2}/\epsilon_{SiO_2}$ is the effective distance between the membrane and the gate, which takes into account the different refractive indices of the air and the SiO_2 substrate (see Fig. 3.6). Due to thermal expansion the strain will change as

$$\epsilon = \epsilon_0 + \int_{T_0=300\,K}^{T} \alpha(T_0)dT, \tag{3.30}$$

where α is the thermal expansion coefficient. This change in tension leads to change in resonance frequency of the mechanical resonator as we cool it down to cryogenic temperatures.

The Q factor of the resonator is also affected by the voltage V_g^{DC} applied between the membrane and the back gate. The mechanical motion generates a displacement current in the membrane, which causes Joule heating. This has the effect of lowering the Q factor which is now given by the expression

$$Q_{eff}^{-1} = Q^{-1} + R_{el}C_z'^2\frac{\left(V_g^{DC} + \Delta\phi\right)^2}{2\pi f_m m_{eff}}, \tag{3.31}$$

where C_z' is the derivative of the capacitance, f_m is resonance frequency, Q is the quality factor without the voltage applied

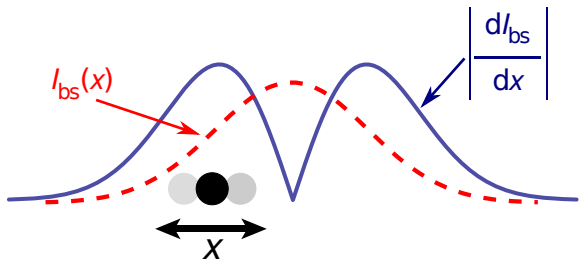

FIGURE 3.7: Schematic of optomechanical coupling. The resonator (black dot) is placed in the laser beam with the intensity profile I_{BS}. The thermal force that acts on the resonator is proportional to the derivative of I_{BS} with respect to the displacement.

and R_{el} is the effective electrical resistance of the membrane [20].

3.5 Optomechanics

Optomechanics is a field of research that studies the coupling of mechanical systems and electromagnetic radiation. Here we will focus on a mechanical oscillator coupled to a laser beam via photothermal back action [93–97]. Back-action refers to the effect of the detector on the measurements itself; the detector is not just making the measurements but is also affecting the outcome of the measurements. In our measurements, the laser used to detect the mechanical vibrations induces heating of the resonator. This can change the resonance frequency and the damping of the resonator.

3.5.1 Photothermal back-action

The dynamical photothermal back-action effect [98] becomes important when the mechanical resonator oscillates in the presence of a strong force gradient, especially when the effect of the force on the resonator is delayed with respect to the displacement modulation (the photothermal force is typically delayed by the characteristic time τ) [35, 99]. Large mechanical vibration amplitudes of the nanotube resonator in the laser focal plane result in a motion dependent optical force (ponderomotive force), which leads to a modified mechanical response [28]:

$$\chi_{\text{eff}}^{-1}[\omega] = \chi^{-1}[\omega] - \sum_j H_j[\omega] \left.\frac{\partial F_j}{\partial x}\right|_{x_0}, \tag{3.32}$$

where x_0 is the equilibrium position (see Fig. 3.7), $\chi[\omega]$ is the intrinsic mechanical susceptibility, F_j is the force associated with the jth optical forces and $H_j[\omega]$ is the Fourier transform of the response function taking into account any delay in the application of F_j [93].

In our case, there is a force F_{p} due to the conversion of electromagnetic radiation into heat, which leads to mechanical deformation that is similar to the displacement of the resonator. The effect of the photothermal force F_{p} is typically delayed by the characteristic time τ, which is usually modelled using the first-order function

$$H_{\text{p}}[\omega] = \frac{1}{1 - i\omega\tau}. \tag{3.33}$$

The effective mechanical susceptibility χ_{eff} remains Lorentzian if the mechanical quality factor is sufficiently large, which holds true in our experiments. The effective mechanical frequency ω_{eff} and effective damping rate Γ_{eff} are given by

$$\omega_{\text{eff}} = \omega_{\text{m}} + \delta\omega_{\text{p}}, \tag{3.34}$$

$$\Gamma_{\text{eff}} = \Gamma_{\text{m}} + \Gamma_{\text{p}}, \tag{3.35}$$

$$\delta\omega_{\text{p}} = -\frac{1}{2m_{\text{eff}}\omega_{\text{eff}}} \operatorname{Re}\{H_{\text{p}}[\omega]\} \left.\frac{\partial F_{\text{p}}}{\partial x}\right|_{x_0}, \tag{3.36}$$

$$\Gamma_{\text{p}} = \frac{1}{m_{\text{eff}}\omega_{\text{eff}}} \operatorname{Im}\{H_{\text{p}}[\omega]\} \left.\frac{\partial F_{\text{p}}}{\partial x}\right|_{x_0}, \tag{3.37}$$

where ω_{m} and Γ_{m} are the intrinsic resonance frequency and the dumping rate, respectively, m_{eff} is the effective mass of the resonator, $\delta\omega_{\text{p}}$ is the frequency shift due to the photothermal force F_{p} and Γ_{p} is the damping due to F_{p}. Using Eq. 3.33 for H_{p}, we can simplify Eqs. 3.37 and 3.36 with:

$$\delta\omega_{\text{p}} \approx -\omega_{\text{m}} \frac{k_{\text{p}}}{2k_{\text{m}}(1 + \omega_{\text{m}}^2\tau^2)}, \tag{3.38}$$

$$\Gamma_{\mathrm{p}} \approx \omega_{\mathrm{m}} \frac{\omega_{\mathrm{m}}\tau}{1+\omega_{\mathrm{m}}^2\tau^2}\frac{k_{\mathrm{p}}}{k_{\mathrm{m}}}, \tag{3.39}$$

where $k_{\mathrm{p}} = (\partial F_{\mathrm{p}}/\partial x)|_{x_0}$ and $k_{\mathrm{m}} = m_{\mathrm{eff}}\omega^2$. This gives a linear dependence of ω_{p} and Γ_{p} with respect to the input laser power. Also, moving the equilibrium position to the maximum of the other detection lobe (see Fig. 3.7) changes the sign of the k_{p} (see Eq. 3.36 and 3.37). This leads to the opposite effect, for example heating instead of cooling of the mechanical resonant mode.

We have omitted the quasi-instantaneous force acting on the particle due to the gradient of the electric field distribution of the laser beam and the polarisability of the particle as it does not affect the motion of the nanotube [28].

Photothermal back-action can be used for cooling the resonator mode, enabling thermal noise cancellation. This effect can be of interest in, for example, cavityless nanomechanical sensing systems [37, 100].

Chapter 4

Fabrication and Setup

Parts of this chapter were published in:

Mass sensing for the advanced fabrication of nanomechanical resonators
G. Gruber, C. Urgell, A. Tavernarakis, A. Stavrinadis, S. Tepsic, C. Magén, S. Sangiao, J. M. de Teresa, P. Verlot, and A. Bachtold
Nano Letters 2019 19 (10), 6987-6992

In this chapter, we will present the details about the fabrication technique as well as the measurement setup layout. First, we will describe the technique for growing the carbon nanotubes and the technique for Pt particle deposition. Next, we will describe the fabrication of devices based on TMD monolayers. Finally, we will describe the measurement setup.

4.1 Carbon nanotube mechanical resonator fabrication

Here we will describe the fabrication process of a mechanical resonator made of carbon nanotubes. The device consists of a single clamped suspended carbon nanotube with a Pt nanoparticle at the tip. The Pt nanoparticle serves as an efficient optical scatterer, which makes it possible to detect the motion of the carbon nanotube without using a cavity [28]. This system enables ultrasensitive detection of the thermally driven vibrations of a carbon nanotube mechanical resonator. An additional benefit is the ultra-low laser probe power, below 1 μW, which enables us to reduce the effects of the heating and the photothermal backaction on the resonator.

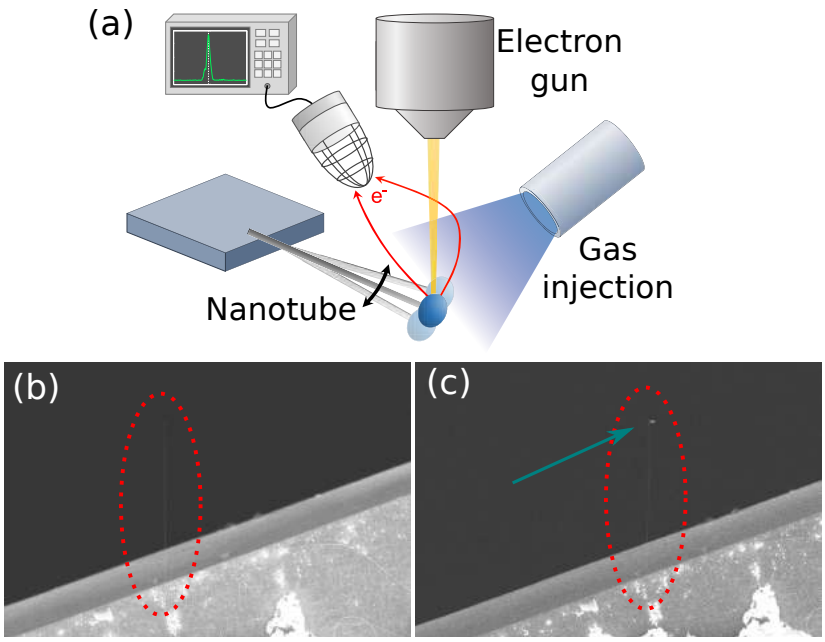

FIGURE 4.1: (a) Schematic of the setup. The electron beam is positioned on the free end of the suspended carbon nanotube cantilever, generating a secondary electron (SE) current, which is detected and analyzed using a spectrum analyzer. Using the gas injection system (GIS), a nanoparticle is grown on the nanotube. SEM image of the nanotube before (b) and (c) after deposition.

4.1.1 CNT growth

We grow the nanotubes using a CVD technique. The catalyst consists of a solution of methanol (CH_3OH) containing iron (Fe) catalyst nanoparticles mixed with molybdenum (Mo) which is used to enhance the catalytic behavior of the Fe. A few droplets of the catalyst solution are deposited on a piece of a silicon wafer and are left to dry for a couple of minutes. The silicon chip is then placed in a CVD oven for growth, where methane gas (CH_4) is decomposed into carbon and hydrogen in the presence of the iron catalyst. Devices were typically grown at 900 °C using a gas flux of 100 sccm H2, 500 sccm Ar and 550 sccm CH4. These parameters were chosen to increase the amount of low diameter few-walled carbon nanotubes. CNTs grow in all directions from the catalyst islands and only a fraction of them will be single

clamped and suspended at the edge of the substrate. In Fig. 4.1 we can see a suspended single clamped CNT after growth.

4.1.2 Characterization using scanning electron microscopy

We use scanning electron microscopy (SEM) for the initial characterization of the suspended devices. All the SEM fabrication is done in a Zeiss Auriga field emission electron microscope equipped with a gas injection system (GIS). The schematic of the fabrication setup is depicted in Fig. 4.1. The electron beam can be focused to a spot size similar to the diameter of the nanotube resonator. The collisions between the electron beam and the nanotube create the emission of secondary electrons, which result from inelastic scattering mechanisms. The displacement of the tube in the electron beam creates a modulation of the secondary electron current. This fluctuation can be detected using a high bandwidth secondary electron detector.

First, we operate in the scanning mode, where the electron beam is scanned across the surface of the sample. The acceleration voltage of the electron beam was 5 kV and the typical beam current was 200 pA. From SEM images we can measure the length of nanotubes (see Fig. 4.2). The length of the typical devices is in the range between 1 and 15 µm and the diameter from 2 to 6.5 nm. Fig. 4.2 shows the typical image obtained with the scanning mode. The image looks blurred as we get towards the free end of the sample, which is the consequence of the mechanical vibration [101, 102]. If the position noise is larger than the extension of the electron beam, the integrated current becomes proportional to the probability to find the object at the electron beam position [103]. For a single clamped beam vibrating in the scanning plane and at the thermal equilibrium, this probability is given by

$$P(\mathbf{r}) = u(\mathbf{r}\cdot\mathbf{e}_{\mathrm{CNT}})\frac{1}{\sqrt{2\pi}\sigma_{\mathrm{th}}}e^{-\frac{(\mathbf{e}_{\mathrm{P}}\mathbf{e}_1)^2}{2\sigma_{\mathrm{th}}^2}}, \tag{4.1}$$

where $\mathbf{e}_{\mathrm{CNT}}$ and $\mathbf{e}_1$ are vectors of the axis and the direction of vibration of carbon nanotube respectively, $\mathbf{r}$ is the vector of the position of the electron beam, u is the fundamental mode shape [104] and σ_{th}^2 is the displacement variance of the thermal motion. Fig. 4.2c shows the Gaussian cross section measured at

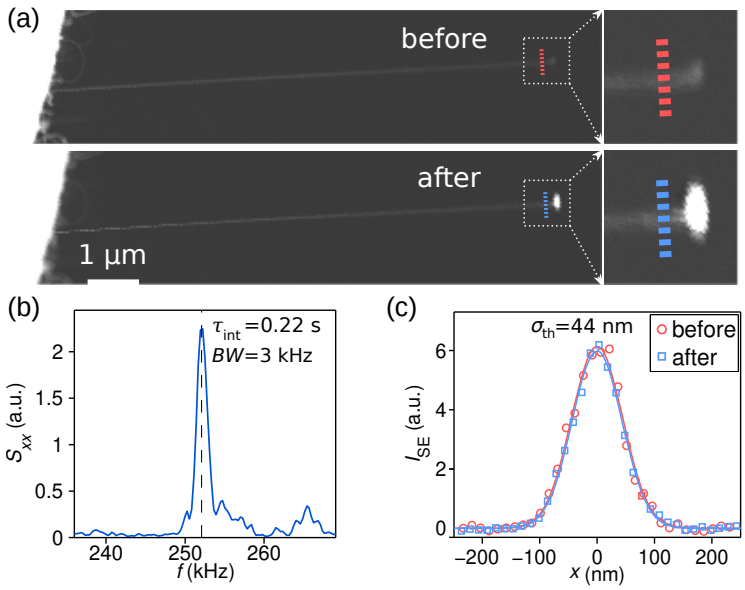

FIGURE 4.2: (a) SEM images of a carbon nanotube before and after depositing a Pt particle; magnified view of the free end is shown on the right side. (b) A typical signal on the signal analyzer used to measure the resonance frequency. (c) SE current profiles along the dashed lines marked in (a) with Gaussian fits (solid lines).

the tip of the nanotube, which enables us to extract the quantitative value of the displacement variance.

Next, we use the SEM in spot mode, where we place the electron beam at the tip of the resonator and measure the secondary electron fluctuations using a spectrum analyzer (Agilent N9020A) [35, 105]. Fig. 4.2b shows the peak at $\omega_0/2\pi \approx 250\,\text{kHz}$, which is the expected frequency for a tube of this dimension. The combination of the scanning mode and spot mode allows us to determine the mechanical properties of the carbon nanotube resonator. The motional variance can be written as [106]

$$\sigma_{\text{th}}^2 = \frac{k_B T}{k}, \tag{4.2}$$

TABLE 4.1: Mechanical properties of the nanotube cantilever devices discussed in the main text. These include the length L, the standard deviation of the thermal displacement σ, the spring constant k, and the mass ratio m^* between the Pt particle and the nanotube.

Device	f_m[kHz]	L [μm]	σ [nm]	k [N/m$\times 10^{-7}$]	m^*
A	54.5	8.2	87.4	5.42	3.7
B	96.1	6.5	22.8	79.2	4.6
C	194	2.4	16.0	164	83.0
D	77.2	7.8	55.8	13.3	5.5
E	57.1	10.0	44.2	21.0	4.6
F	107	5.0	34.9	33.9	8.8
G	44.5	5.2	80.1	6.46	18.3
H	58.4	4.6	73.5	7.63	60.9
I	48.1	11.9	90.0	5.11	3.7

which yields the spring constant $k = 2.1 \times 10^{-6}$ N/m. From here we can calculate the effective mass m_{eff} as

$$m_{\text{eff}} = \frac{k}{\omega_0^2}. \tag{4.3}$$

The variance of motion can also be related to the physical properties of the nanotube with the following equation [104]

$$\sigma_{\text{th}}^2 = 0.1061 \frac{L^3 k_B T}{Y r^3 G}, \tag{4.4}$$

where r is the radius of the nanotube, G is the thickness of graphene, T is the temperature, Y is the Young's modulus, L is the length, and k_B is Boltzmann's constant.

In Table 4.1 we can see the mechanical parameters of common devices measured using the technique above.

4.1.3 Particle growth using GIS

Next, we start the procedure of depositing the Pt particle on the free end of the nanotube. Methylcyclopentadienyl-(trimethyl)-platinum(IV) was used as a precursor gas to deposit Pt onto the sample surface when illuminated by the electron beam [107].

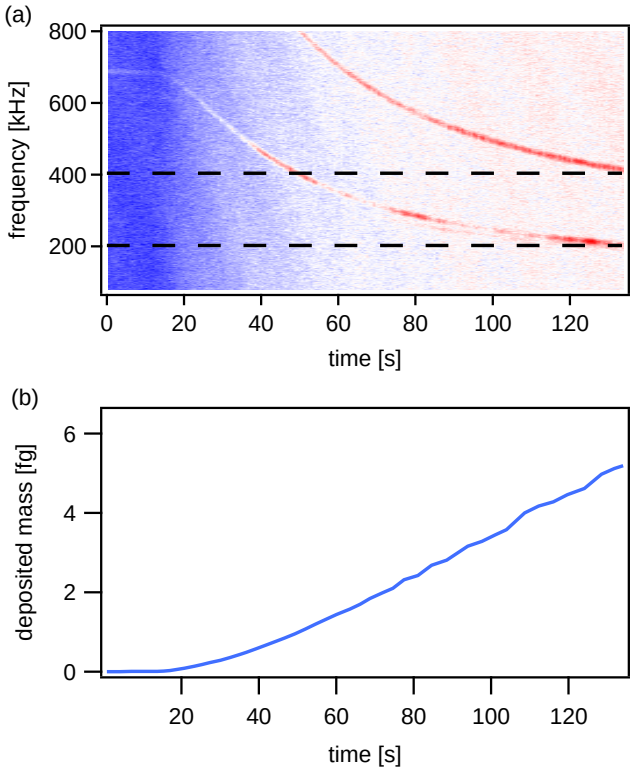

FIGURE 4.3: (a) Measurement of the resonance frequency during the deposition process; at $t \approx 20\,\mathrm{s}$ the GIS valve was opened and at $t \approx 135\,\mathrm{s}$ it was closed and the beam exposure stopped. (b) Deposited mass determined from (a) using Eq. 4.6

The GIS nozzle is positioned $\approx 500\,\mu\mathrm{m}$ away from the substrate. While depositing, the mass of the Pt particle is monitored in real-time using a custom computer program. We continuously acquire the resonance spectrum of the thermal motion of the nanotube. The resonance frequency changes with the deposited mass as

$$f_\mathrm{m} = \frac{1}{2\pi}\sqrt{\frac{k}{m_\mathrm{eff}}}. \tag{4.5}$$

It is important to note that the estimated spring constant is the same when measured before and after the deposition, see Fig. 4.2c. This shows that the spring constant is not affected by the deposition process and the change in resonance frequency

TABLE 4.2: Atomic and mass fraction of carbon, platinum and oxygen, determined by the EDXS measurements.

element	atomic fraction [%]	mass fraction [%]
carbon	84.6	41.5
oxygen	8.8	5.8
platinum	6.6	52.7

is due to mass deposition [106, 108]. A typical measurement is shown in Fig. 4.3a. The gas nozzle is opened at $t \approx 20\,\mathrm{s}$. As the particle grows the detection becomes strongly nonlinear and higher harmonics appear. This can be explained by higher interaction volume due to the deposition process. The fundamental frequency decreases over time which is consistent with mass absorption. We can calculate the deposited mass from

$$\Delta m(t) = \frac{k}{(2\pi)^2}\left(\frac{1}{f_{\mathrm{m,t}}^2} - \frac{1}{f_{\mathrm{m},0}^2}\right), \tag{4.6}$$

where $f_{\mathrm{m,t}}$ is resonance frequency measured at time t and $f_{\mathrm{m},0}$ is resonance frequency measured before starting the deposition process.

Fig. 4.3b shows the deposited mass from the measurements in Fig. 4.3a using the equation above. Here we can see that the mass deposition is linear in time and we can determine the deposition rate [108]. After the deposited mass of the Pt particle reaches the desired value we close the gas nozzle and stop the electron beam to prevent spurious growth. The deposited mass divided by the cantilever mass of different devices can be seen in the table 4.1.

Chemical analysis was conducted via energy-dispersive X-ray spectroscopy (EDXS) using an EDAX detector. The results are shown in the table 4.2. Platinum accounts for 52.7 percent of the mass of the particle. The observed oxygen content is attributed to the air molecules that diffuse into the particle during the transfer of the device from the SEM to the STEM [108].

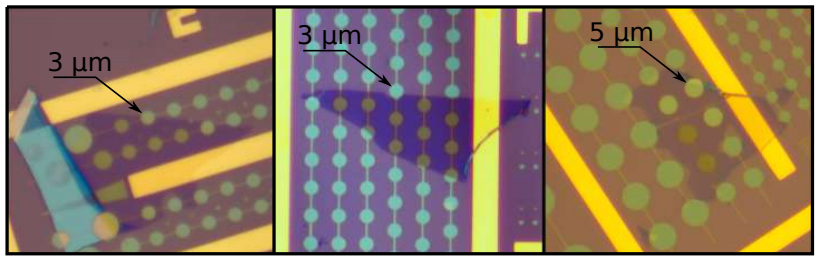

FIGURE 4.4: Optical images of various fabricated mechanical resonators based on TMD monolayers. The device in the left image is made of WSe_2, and other devices are mode $MoSe_2$. The diameter of the resonator is marked in the figure. Adapted from [109].

4.2 TMD monolayer mechanical resonator fabrication

Here we will describe the fabrication process of TMD monolayer mechanical resonators. The devices consists of a TMD monolayer, specifically $MoSe_2$ or WSe_2 monolayers, suspended over holes with the diameters in range from 2-5 µm (see Fig. 4.4).

The fabrication process consists of three different steps: fabrication of the substrate with holes and electrodes, mechanical exfoliation of a monolayer from bulk material, and dry transfer of the monolayer onto the substrate. Details of these steps are given below.

4.2.1 Fabrication substrate

For the fabrication of the substrate, we use a Si^{++}/SiO_2 wafer. The thickness of the Si layer is 1 µm and of the SiO_2 is 285 nm. The fabrication process includes the deposition of gold electrodes and the etching of holes over which we suspend TMD monolayers.

To evaporate the gold electrodes we start by designing and then patterning a PMMA mask using electron beam lithography. Once the PMMA mask is patterned and developed we proceed with the thermal evaporation of electrodes. First, we use a thin adhesive layer (5 nm) of Titanium, followed by a 50 nm thick layer of gold. The final step is to lift off the PMMA and the

residual gold, which leaves gold electrodes on the substrate. Next, we proceed with the fabrication of the holes.

Similar to the fabrication of the electrodes, the fabrication of holes in the substrate also starts by patterning the mask using electron beam lithography and developing it. The exposed parts of SiO_2 are then etched using reactive ion etching. The depth of the hole is $\sim$ 180 nm and is chosen to optimize the motion detection of the monolayer. We clean the PMMA off the chip, which leaves the substrate with holes and electrodes. Finally, we proceed with the dry transfer.

4.2.2 Mechanical exfoliation

We use bulk crystals $MoSe_2$ and WSe_2 obtained from *hqgraphene* and *2D semiconductors*. During the process of exfoliation, we use PDMS (polydimethylsiloxane). This material is widely used for mechanical exfoliation as it leaves a very small amount of contamination on the monolayers.

We start by placing a small piece of bulk crystal onto a 2 mm thick layer of homemade PDMS. TMD crystal is then covered by a thin layer (0.1 mm) of PDMS, which we use to peel off layers from the bulk crystal. This process is repeated until we are left with monolayers on top of the thick PDMS layer. The thickness of the crystal is verified by optical contrast measurements and is also confirmed later in the experimental setup by measuring the photoluminescence of the monolayers.

4.2.3 Dry transfer

The final device is made by transferring the monolayer from PDMS over the holes and electrodes on the substrate. First, we use a micromanipulator to align and position the monolayer flake over the pre-patterned structure of holes and electrodes. Then we slowly bring the monolayer and substrate in contact with each other. Once the monolayer is in contact we start lifting the PDMS, which leaves the monolayer on the substrate. This process is very robust and the success rate is around 70-80 % for holes with a diameter of 3 µm. The success rate drops as we increase the diameter of the holes, as the monolayer tends to collapse more often. Figure 4.4 shows some devices fabricated using this technique.

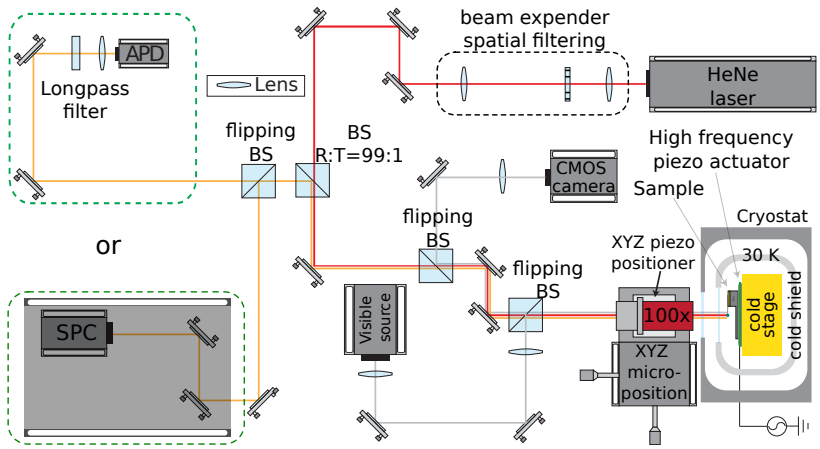

FIGURE 4.5: Schematic of the optical setup used for the experiment. Details are given in the main text. Adapted from [84].

4.3 Measurement setup

We developed a low-temperature optical setup that is based on a 3 K base-temperature cryostat with optical and electrical access. The setup in the configuration outlined below has been optimized for the detection of nanotube resonators at low temperatures. Due to the strong interaction between the Pt particle attached at the free end of the nanotube cantilever with the light, the collection efficiency of the setup had to be optimized to minimize the backaction effects. The main parts of the setup are described below (Fig. 4.5).

The excitation source is a continuous wave HeNe laser with the wavelength of $\lambda = 633\,\text{nm}$. The output of the laser is passed through a beam expander with a pinhole for spatial filtering. Following the beam expander is a high reflection polarizing beam splitter (reflection to transmission ratio is 99:1). This splitter essentially defines the excitation and the collection path. In the reflection path, it collects 99 % of the reflected light.

The next part of the setup consists of two beam splitters, a CMOS camera, and a LED light source. These elements greatly facilitate the initial search and alignment of the sample. Both beam splitters are mounted on a flipping stage so that they can be removed during the experiment.

The objective used to focus the light onto the sample is 100X

Mitutoyo Plan Apo NIR HR infinity-corrected objective, with a numerical aperture of $NA = 0.7$ and a working distance of 10 mm. The objective is placed outside of the cryostat due to limited space available in the cryo chamber. The objective is placed on an XYZ piezo stage (Jena NV40 3 CLE) with a resolution of 2 nm. The piezo is used to move the laser beam with high accuracy. The objective and the piezo are placed on top of a millimeter accuracy XYZ positioner for coarse positioning.

The cryostat is a low vibration closed-cycle Helium optical cryostat from Montana Instruments. The samples are mounted on a stage which has a base temperature of 3 K, but the temperature can also be set anywhere between 3 K and 295 K. A radiation shield is attached to the stage that keeps the temperature at 30 K. Furthermore, one RF line is connected to a fast piezoelectric stage inside the cryostat that is used to actuate the nanotubes through inertia forces.

After reflection, the light can be focused onto a high gain avalanche photodetector (APD440A2, APD130A2) or a single-photon counter (Excelitas Technologies, SPCM-AQRH-15). We feed the output of the APD into a Zurich lock-in amplifier or a spectrum analyzer (Agilent N9020A).

The interfacing of the setup was done in Python using QTLab, an IPython based measurement environment.

4.3.1 Detection principle

Carbon nanotube resonator motion detection The detection principle is presented on the Fig. 4.6a. The intensity profile of the laser beam is described by a Gaussian distribution [28]. The fluctuation of the resonator in this Gaussian profile results in the modulation of the back-scattered intensity, proportional to the displacement. The optomechanical transduction is proportional to the derivative of the Gaussian intensity profile along the motion direction; the sensitivity is minimal at the center of the intensity profile, while it is maximum at the slopes of the profile as seen in the Fig. 4.6a. Fig. 4.6b shows the results obtained while displacing the focal point in the focal plane. Two lobes are separated by the symmetry axis which is orthogonal to the motion direction.

One can see asymmetry between the two detection lobes in the Fig. 4.6b. This is the consequence of the dynamical backaction

described in chapter 3.5, which leads to cooling or heating of the thermal vibrations in different lobes. This effect becomes even more prominent as we cool down the device and the Q factor becomes larger. To avoid backaction cooling or heating of the mode it is necessary to reduce input laser power. This leads to a detection problem as the back-scattered light intensity falls below the noise floor of the APD used in the experiment. For this situation, we developed a measuring technique using the single-photon counter as the detector.

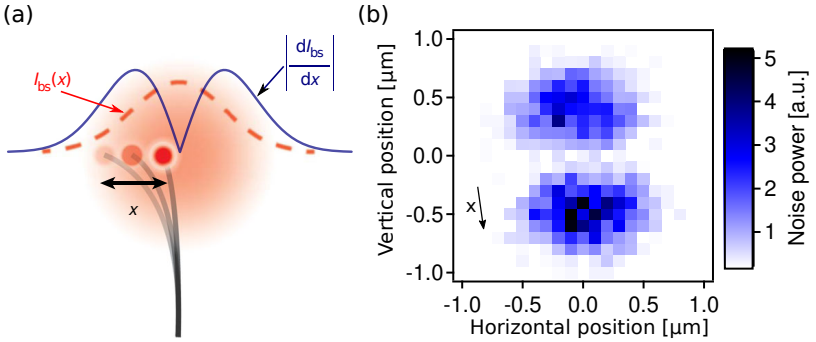

FIGURE 4.6: (a) Schematic illustration of the optical detection principle of the motion of a nanomechanical resonator. As the nanoparticle (red dot) displaces in the beam it scatters light proportional to the local intensity of the laser beam (red, dashed line). Displacement x of the resonator results in fluctuation of the scattered intensity that is proportional to the intensity gradient dI_{bs}/dx. (b) The fluctuation of the back-scattered intensity as the particle is moved in the waist of the focused laser. The obtained intensity fluctuation identifies the resonator displacement direction and laser waist intensity gradient (black arrow), as depicted in (a). Adapted from [28].

TMD monolayer resonator motion detection The detection of the mechanical vibrations of a TMD monolayer is achieved by placing the monolayer in the gradient of an input laser power. The gradient is the consequence of the interference of the incoming and the reflected beam from the Si/SiO_2 substrate. Fig. 4.7b shows the simulation of the interference pattern for the particular substrate and laser wavelength used in our experiments. As the TMD monolayer displaces in this gradient it will absorb different amount of light depending on its position (the TMD monolayer

has constant absorption coefficient at 633 nm, around 5-10 % for WSe_2 and $MoSe_2$ [80]. This absorption effect will modulate the reflected laser beam intensity at the resonance frequency, which is later detected using an APD.

As with a carbon nanotube mechanical resonator, the absorption and backaction effects can strongly influence mechanical vibrations. High Q mechanical resonators based on TMD monolayers are very sensitive to temperature variations induced by laser power absorption. Therefore, it is very important to minimize the power of the input laser beam, especially at low temperatures.

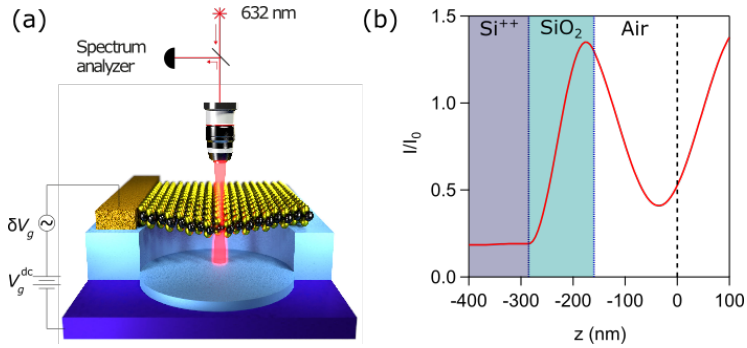

FIGURE 4.7: (a) Illustration of the TMD monolayer mechanical resonator probed by a laser beam. (b) Numerical simulation of interference pattern created by the Si/SiO_2 substrate. Black dashed line at $z = 0$ presents the position of the TMD monolayer in the pattern. Adapted from [91].

4.3.2 Single photon counter

When measuring the nanotube cantilever at low temperature it is necessary to use ultra-low powers (10 nW of the input laser power) to avoid optical backaction and heating of the nanotube.

To overcome this problem we use the single-photon counter mentioned above, which operates in the Geiger mode and has a dark rate of approximately 50 counts per second, corresponding to $\approx$ 15 nW at $\lambda = 633$ nW. Fig. 4.8 schematically compares the signal of the APD to the signal of the single-photon counter. Instead of a continuously varying voltage signal, we have a sequence of photon pulses, whose density varies over time. This

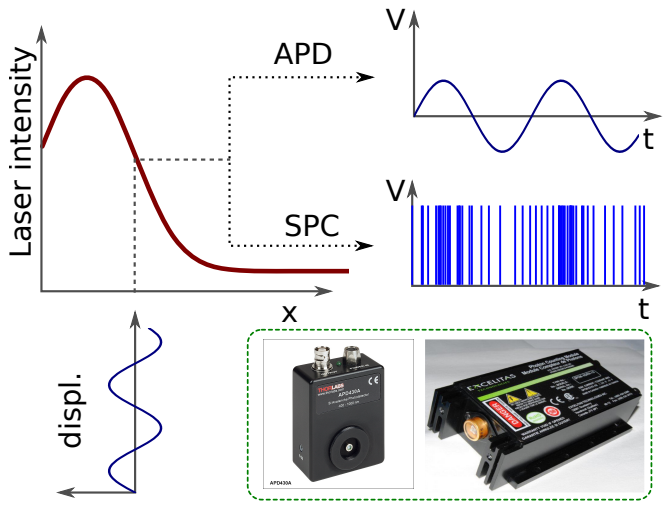

FIGURE 4.8: Schematic comparison of the difference between the single photon counter SPC and APD signal. The APD signal is a continuous voltage signal linearly proportional to the displacement, while the SPC signal gives the sequence of photon pulses whose density is proportional to the displacement of the tube. In the green inset are Excelitas single photon counter and Thorlabs APD used in the experiment.

kind of signal is called pulse density modulation. They can be low pass filtered, to obtain a mean photon flux (in cps or $Hz^{-}1$). The signal is analyzed with time-stamping devices to acquire the full temporal statistics or resolved with a spectrum analyzer. Here we acquired the full temporal statistic which is later numerically averaged to obtain the mean photon flux. We then performed an FFT to analyze the mean photon flux signal.

The single-photon counter is also used to measure the photoluminescence of TMD monolayers with very high efficiency. The photoluminescence of the TMD monolayer is enhanced by several orders of magnitude when compared with a TMD crystal with two or more layers [81]. This is a consequence of the crossover from indirect- to a direct-gap semiconductor in the monolayer limit. The photoluminescence measurement of the TMD crystal provides an easy way to distinguish a monolayer from a multilayer TMD.

Chapter 5

Interrelation of elasticity and thermal bath in nanotube cantilevers

Parts of this chapter are published in:

Interrelation of elasticity and thermal bath in nanotube cantilevers
S. Tepsic, G. Gruber, C. B. Møller, C. Magén, P. Belardinelli, E. R. Hernández, F. Alijani, P. Verlot and A. Bachtold
PRL

In this chapter, we report the first study on the thermal behavior of the stiffness of individual carbon nanotubes, which is achieved by measuring the resonance frequency of their fundamental mechanical bending modes. We observe a reduction of the Young's modulus over a large temperature range with a slope $-(173 \pm 65)$ ppm/K in its relative shift. These findings are reproduced by two different theoretical models based on the thermal dynamics of the lattice. These results reveal how the measured fundamental bending modes depend on the phonons in the nanotube via the Young's modulus. An alternative description based on the coupling between the measured mechanical modes and the phonon thermal bath in the Akhiezer limit is discussed.

5.1 Introduction

In engineering, thermoelasticity is central in determining the elastic limits of structures ranging from large scale spacecrafts [44] and nuclear plants [45] down to nano-structured systems. A rich underlying phenomenology emerges for small structures, including dissipation [46, 47], fluctuations [48, 49] and torque generation [50, 51], which are key to the development of state-of-the-art nano- and micro-electromechanical technologies [110, 111]. Thermoelasticity has also been used with success in condensed matter physics, where thermal measurements of the stiffness unveil the phase transition of charge-density waves and superconductivity in transition metal dichalcogenides and high-T_c superconductors [112–114]. From a fundamental point of view, the thermal behavior of the stiffness – quantified by the Young's modulus – emerges from the non-trivial interplay of the binding energy and the lattice dynamics. However, the effect of the thermal lattice dynamics on the stiffness has remained elusive in individual nanoscale systems due to experimental challenges related to manipulating and measuring such small objects.

In this work, we use the exquisite sensing capabilities of mechanical resonators based on nanoscale systems [14, 23, 25, 29, 32, 37, 38, 115–123] to resolve the small effect associated with the thermal behaviour of their stiffness. Using the resonance frequency measured by optomechanical spectroscopy, we estimate the Young's modulus of micrometer-long nanotube cantilevers from room temperature down to a few Kelvins. These results agree with the temperature dependence of the resonance frequency predicted by molecular dynamics simulations, which take into account the lattice dynamics of the nanotube. Our measurements are also consistent with the Young's modulus directly computed from a quasi-harmonic approximation of the free energy of the phonon modes. This work not only shows how the stiffness of an individual nanotube is related to its phonons, but it also highlights the role of the phonon thermal bath in nanotube cantilevers, which is a topic of importance in the field of nanomechanical resonators [14, 23, 25, 29, 32, 37, 38, 115–123].

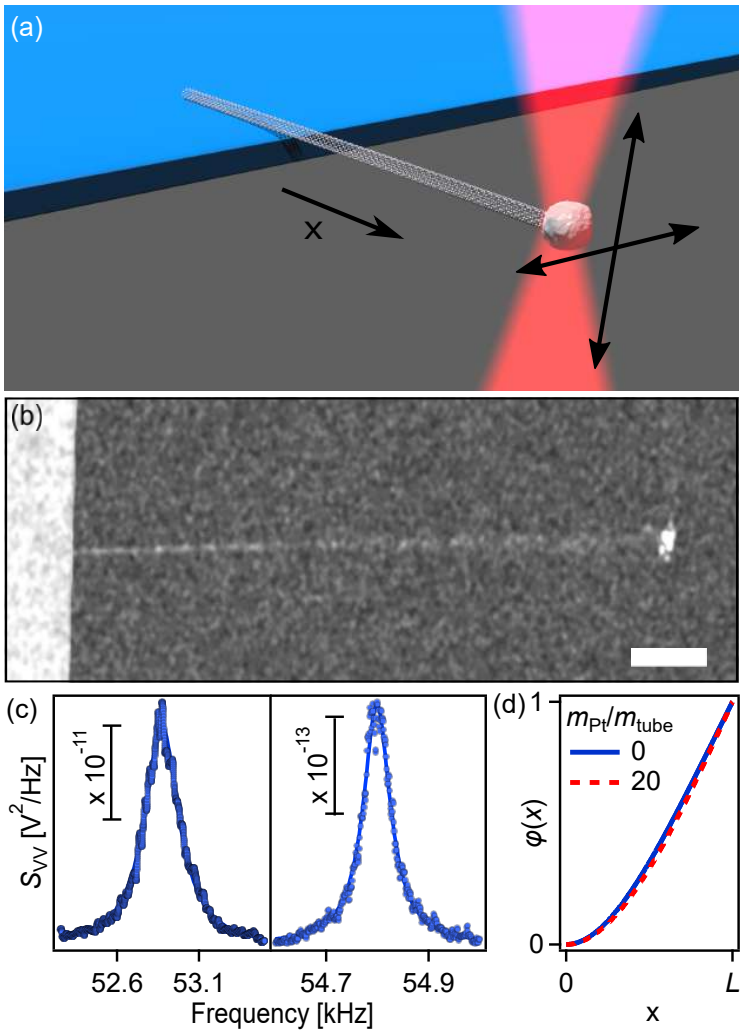

FIGURE 5.1: (a) Schematic of the experimental setup. The two double arrows represent the polarization of the fundamental mode doublet. (b) Device A imaged by SEM after the deposition of a platinum nanoparticle; the scale bar is 1 µm [108]. (c) Power spectra of the optical reflection from device A showing the resonance of the thermal motion of the fundamental mode doublet at 300 K. The two spectra are recorded using different positions of the nanotube in the laser waist to enhance the signal [28] (d) Calculated profile $\varphi(x)$ of the fundamental mode shape along the nanotube axis estimated for two different platinum particle masses normalized by the nanotube mass.

5.2 Characterization of nanotube cantilevers

We use the single clamped resonator layout, where one end of the nanotube is attached to a silicon chip and the other end is free. This layout avoids prestress in the nanotube built-in during fabrication, in contrast to what may happen with the double clamped layout. As a result, the restoring force is given solely by the bending rigidity. This enables us to probe the Young's modulus Y by measuring the resonance frequency, $\omega_0 \propto \sqrt{Y}$ [124]. Such a resonance-based methodology is also employed in thermoelasticity studies on larger scale systems [112–114, 125].

We engineer a platinum particle at the free end of the nanotube so that the resonator can be measured by scattering optomechanical spectroscopy (Fig. 5.1a) [28]. We grow the particle by focused electron beam-induced deposition [108]. Figure 5.1b shows a scanning electron microscopy image of device A. Transmission electron microscopy (TEM) indicates that nanotubes can be made from one to a few walls, with a median value of two walls. The vibrations are detected by measuring the backscattered intensity from a 633 nm laser beam focused onto the particle. Figure 5.1c shows the optomechanical spectrum of device A. The resonance frequencies of the fundamental modes polarized in perpendicular directions are about 52.9 kHz and 54.8 kHz. The platinum particle does not affect the restoring force nor the eigenmode shape of the two fundamental modes (Fig. 5.1d), in contrast to what happens for higher frequency modes (Sec. A.1). In this work, we use low laser power so that the resonance frequency is not affected by absorption heating and optical backaction [28].

The carbon nanotubes were grown on silicon substrates via chemical vapor deposition. A Zeiss Auriga scanning electron microscope (SEM) was used to select suitable nanotube cantilevers. The SEM is equipped with a gas injection system, which was used to deposit platinum particles at the apex of the nanotubes for their optomechanical functionalization [28, 108]. Figure 5.2(a) shows a pristine nanotube cantilever (device A). Figure 5.2(b) shows the same cantilever after the deposition of a Pt particle. The free end of the cantilever is blurred in the SEM images due to the thermally driven motion. The displacement profile was measured by an SEM line trace across the nanotube at the tip. Figure 5.2(c) shows the observed Gaussian distribution in the secondary electron current I_{SE}, as expected for thermal vibrations [106]. The

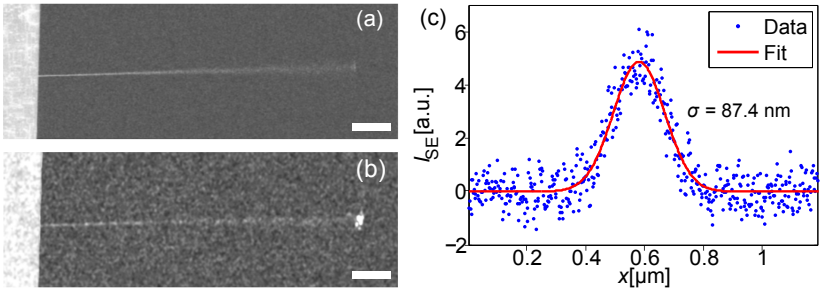

FIGURE 5.2: Device A imaged by SEM (a) before and (b) after deposition of a Pt nanoparticle; the scale bars are 1 µm. (c) Secondary electron signal I_{SE} across the apex of the nanotube; from a Gaussian fit the displacement variance $\sigma^2 = (87.4\,\mathrm{nm})^2$ is determined.

displacement variance $\sigma^2 = (87.4\,\mathrm{nm})^2$ was obtained from a fit of the data. The spring constant $k = 5.42 \times 10^{-7}\,\mathrm{N/m}$ was determined from the equipartition theorem $k = k_B T/\sigma^2$ where k_B is the Boltzmann constant and T is the temperature [106]. The mass of the deposited Pt particle was controlled during its growth by monitoring the mechanical resonance frequency of the lowest flexural mode of the nanotube; the thermal vibrations were measured by pointing the electron beam onto the apex of the nanotube in spot mode while recording the noise of I_{SE} [108]. The initial effective mass of the nanotube was $m_0^* = 243\,\mathrm{ag}$ and the mass of the deposited particle visible in Fig. 5.2(b) was $m_{Pt} = 3.6(11)\,\mathrm{fg}$. All discussed samples were fabricated as described above. The mechanical properties of the samples that were optomechanically characterized at low temperature (devices A-I) are summarized in Table 5.1.

We performed high-resolution transmission electron microscopy (HRTEM) to assess the microscopic structure of nanotube cantilevers. The samples were fabricated on silicon aperture windows using the identical procedure as outlined above. HRTEM imaging was conducted using a Thermo Fisher Titan Cube 60-300, equipped with an image aberration corrector CETCOR from CEOS. The microscope was operated at 80 kV to minimize beam damage and achieve a spatial resolution below 1.4 Å. Figure 5.3 shows atomically resolved images obtained for different devices near the clamping point where the thermal displacement is

TABLE 5.1: Mechanical properties of the measured nanotube cantilever devices. These include the length l, the standard deviation of the thermal displacement σ, the spring constant k and the mass ratio m^* between the Pt particle and the nanotube as defined in Supplementary Section A.1.

Device	l [μm]	σ [nm]	k [N/m]	m^*
A	8.2	87.4	5.42×10^{-7}	3.7
B	6.5	22.8	7.92×10^{-6}	4.6
C	2.4	16.0	1.64×10^{-5}	83.0
D	7.8	55.8	1.33×10^{-6}	5.5
E	10.0	44.2	2.10×10^{-6}	4.6
F	5.0	34.9	3.39×10^{-6}	8.8
G	5.2	80.1	6.46×10^{-7}	18.3
H	4.6	73.5	7.63×10^{-7}	60.9
I	11.9	90.0	5.11×10^{-7}	3.7

negligible. The devices shown are a single wall device, a seven wall device, and a triple wall device. The latter device was also characterized optomechanically at low temperature before conducting the HRTEM experiments and is referred to as device C in table 5.1. The amorphous material visible in Figs. 5.3 (a) and (c) presumably consists of hydrocarbons adsorbed during their exposure to air and the particle growth [108].

Using such HRTEM images, we determined the number of walls and the associated diameters for six different devices ranging from a single wall to seven wall nanotubes. Table 5.2 shows the diameters obtained by HRTEM together with other parameters obtained by SEM. The calculation of the Young's modulus in the table is outlined in Section 5.3.

5.3 Estimation of Young's modulus

The estimated Young's modulus is similar to previously predicted and measured values [101, 104, 126–129]. This indicates that the contamination adsorbed on the nanotube surface has little contribution to the stiffness of the nanotube. The contamination, which is localized along some portions of nanotubes as observed by TEM, presumably consists of hydrocarbons adsorbed during their exposure to air and the particle growth. The

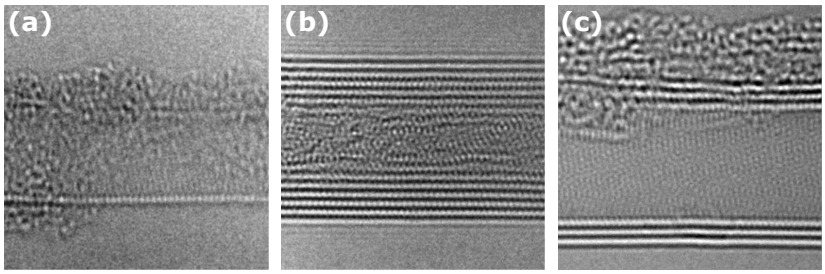

FIGURE 5.3: HRTEM images recorded near the clamping point of single wall device T1 (a), seven wall device T6 (b) and triple wall device C (c). In order to enhance the signal-to-noise ratio multiple images were overlaid and averaged. All image dimensions are 10 nm by 10 nm.

TABLE 5.2: Properties of different nanotube cantilevers. Cantilever length l and spring constant k were obtained by SEM imaging. Number of walls N and associated diameters d_i were obtained by HRTEM. The Young's modulus Y was calculated as described in section 5.3.

Dev	N	l [μm]	k [N/m]$\times 10^{-}7$	d_i [nm]	Y [TPa]
T1	1	2.8 ± 0.1	6.51 ± 1.53	3.24 ± 0.14	1.04 ± 0.49
T2	2	2.2 ± 0.1	19.3 ± 4.2	3.37 ± 0.16, 2.58 ± 0.16	0.91 ± 0.46
T3	2	1.8 ± 0.1	33.3 ± 5.2	3.58 ± 0.11, 2.80 ± 0.09	0.79 ± 0.34
T4	2	3.8 ± 0.1	7.42 ± 1.73	3.75 ± 0.19, 2.89 ± 0.22	1.31 ± 0.64
C	3	2.4 ± 0.1	164 ± 38	5.84 ± 0.09, 5.15 ± 0.08, 4.38 ± 0.11	1.35 ± 0.55
T6	7	7.1 ± 0.1	7.36 ± 1.83	6.24 ± 0.07, 5.55 ± 0.07, 4.88 ± 0.09, 4.20 ± 0.10, 3.53 ± 0.09, 2.88 ± 0.09, 2.15 ± 0.14	0.96 ± 0.33

typical stiffness reported for such amorphous material is comparatively low $Y \approx (50 - 300)$ GPa [130].

We determine the Young's modulus at $T = 300$ K for various nanotube cantilevers. We use the geometrical parameters determined by SEM and HRTEM as described in Sec. 5.2 (see table 5.2). The spring stiffness k of a nanotube cantilever composed of N concentric shells is the sum of the spring constant k_i of each shell,

$$k = \sum_{i=1}^{N} k_i, \tag{5.1}$$

where we assume that the interaction between the concentric shells has negligible contribution to the spring stiffness. We determine Y of a nanotube cantilever with N shells from its measured spring stiffness, its length and the diameter d_i of each shell, using

$$Y = 0.8488 \frac{k l^3}{\sum_{i=1}^{N} (d_i^3 g + g^3 d_i)}, \tag{5.2}$$

where we assume that all the shells have the same Young's modulus and the wall thickness is $g = 0.34$ nm. This expression can be obtained from Sec A.1.

Figure 5.4 shows the resulting Y for the six measured devices plotted as a function of the cantilever length. The error bars represent the standard error ΔY for each measurement, which is determined by expanding Eq. 5.2 and calculating the propagation of the measurement uncertainties in l, k and d (see table 5.2). The solid line is the mean Young's modulus $\bar{Y} = \sum Y/N = 1.06$ TPa whereas the dashed lines indicate the confidence intervals $\Delta\bar{Y}$. The latter is estimated by summing the standard error of the Y value of the different cantilevers and the mean of their standard error ΔY divided by $\sqrt{N}$, which yields $\Delta\bar{Y} = \pm 0.28$ TPa.

5.4 Measuring the stiffness at low temperature

Figure 5.5 shows the variation of the resonance frequency of device A when sweeping the temperature T. The variation is remarkably similar for both fundamental modes, independent of the temperature sweep direction and of whether the motion is thermal or driven with a piezo-actuator. This variation of the resonance frequency $\omega_0 = \sqrt{k/m}$ is associated with the change

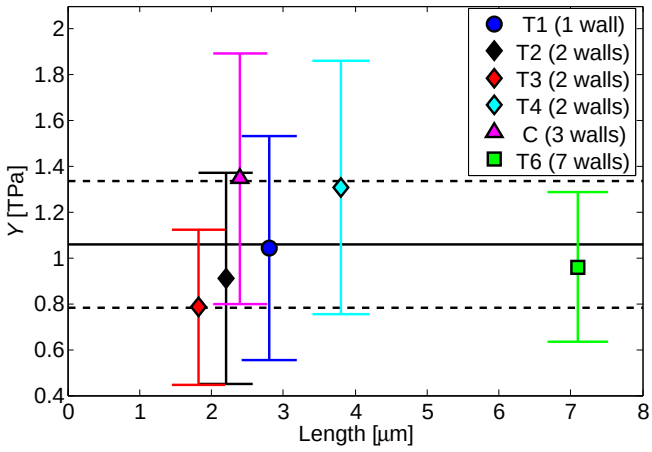

FIGURE 5.4: Y determined from SEM and HRTEM for six different nanotube cantilevers. The error bars represent the standard error for each measurement. The solid black line marks the mean value $\bar{Y} = 1.06\,\text{TPa}$ of all the measurements and the dashed black lines indicate the corresponding confidence intervals $\Delta\bar{Y} = \pm 0.28\,\text{TPa}$.

of the spring constant k, which is linearly proportional to Y in the single clamped layout. We extract the relative shift of the Young's modulus from the relation $\frac{\Delta Y(T)}{Y(T_{min})} = 2\frac{\Delta\omega_0(T)}{\omega_0(T_{min})}$, where T_{min} is the lowest temperature at which we record the vibrations. Figure 5.6a shows the measurements of nine different devices. They all feature the same trend with a reduction of the Young's modulus when increasing temperature. The dependence is essentially linear above about 100 K; the slope averaged over devices is $\Delta Y(T)/Y \cdot 1/T = -(173 \pm 65)$ ppm/K.

These measurements are related to neither the mass adsorbed on the nanotube nor the diffusion of adsorbed atoms along the nanotube nor the thermal expansion of the nanotube nor the combination of the Duffing nonlinearity and the thermal motion, as discussed now. The measured T dependence of ω_0 could originate from the variation of the mass m adsorbed on the nanotube. However, mass adsorption, which occurs when lowering T, would lead to a reduction of ω_0 [40, 41, 108, 131], which is just the opposite of what is measured. Moreover, we do not observe any hysteresis in ω_0 when cooling the device from 300 K to

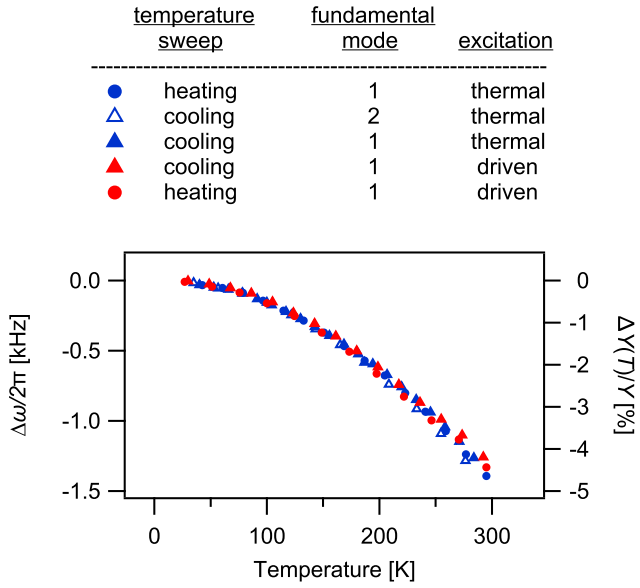

FIGURE 5.5: Resonance frequency and relative change of the Young's modulus of device A as a function of cryostat temperature. The legend indicates the direction of the temperature sweep (cooling or heating), which fundamental mode is measured, and whether the detected vibrations are thermal or driven with a piezo-actuator.

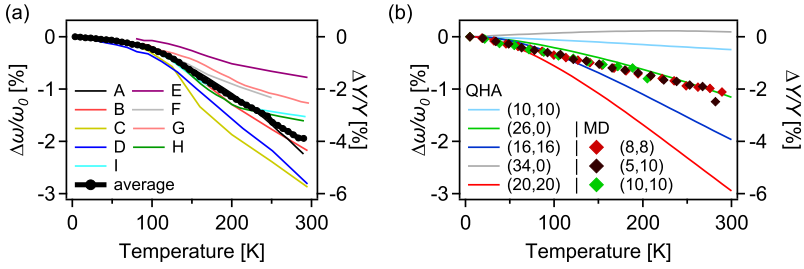

FIGURE 5.6: Comparison of the relative change of the resonance frequency and the Young's modulus between experiment (a) and theory (b) for different nanotubes. The theoretical results are obtained for different nanotube chiralities with either molecular dynamics (MD) simulations or quasi-harmonic approximation (QHA) calculations. The MD simulations and the QHA calculations quantify $\Delta\omega_0/\omega_0$ and $\Delta Y/Y$, respectively.

cryogenic temperatures and then heating it back to 300 K, which shows that temperature-induced mass adsorption and desorption plays a negligible role [41]. Thus, the measured variation of $\omega_0(T)$ is not accounted for by adsorbed mass changes.

The measurements could be related to the change in the length of the nanotube when the thermal environment is varied since the spring constant depends on the nanotube length as $k \propto l^{-3}$. However, the measured resonance frequency reduction at room temperature $\Delta\omega_0(T = 300\ K)/\omega_0 \simeq -2.2 \times 10^{-2}$ for device A is much larger than the predicted reduction $\Delta\omega_0(T = 300\ K)/\omega_0 = -1.25 \times 10^{-3}$ based on the longitudinal expansion of the nanotube in different thermal conditions obtained from our molecular dynamics simulations for an (8,8) CNT. The predicted relative change in stiffness $k(T)/k_{5K}$ associated with the thermal expansion of the nanotube as a function of temperature is shown in Fig. 5.7. The results are obtained by calculating the elongation of the nanotube for different thermalization temperatures. Here we assume that the stiffness ratio $k(T)/k_{5K}$ is proportional to the cube of the function $(l_{5K}/l(T))$ in which l_{5K} and $l(T)$ are the length of the CNT at 5 K and at temperature T, respectively. The decreasing behavior reported in Fig. 5.7 suggests that the nanotube stretches with the increase in temperature. Overall, this shows that the thermal expansion is not the cause of the measured $\omega_0(T)$ reduction.

Another possible origin could be the nanotube resonance frequency change that arises from the combination of the Duffing nonlinearity and the thermal motion. Figure 5.8a shows the measured variation of the resonance frequency as a function of driven vibrational amplitude $\langle x^2_{\text{vibra}} \rangle$, which allows us to quantify the Duffing constant γ_{eff} using

$$\Delta\omega = \frac{3}{8}\frac{\gamma_{\text{eff}}}{\omega_0}\langle x^2_{\text{vibra}} \rangle . \tag{5.3}$$

The driven amplitude is calibrated following the procedure described in Ref. [28]. We compute the linear temperature dependence of the resonance frequency expected from the combination of the Duffing nonlinearity and the thermal vibrations using

$$\Delta\omega = \frac{3}{8}\frac{\gamma_{\text{eff}}}{\omega_0}\langle x^2_{\text{th}} \rangle = \frac{3}{8}\frac{\gamma_{\text{eff}}}{\omega_0}\frac{k_{\text{B}}T}{k}. \tag{5.4}$$

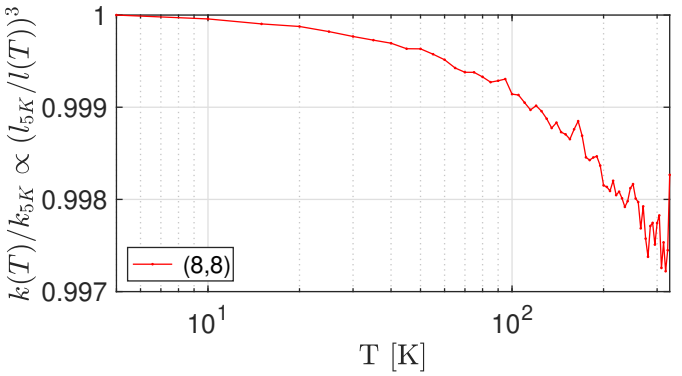

FIGURE 5.7: Predicted relative change in stiffness with respect to temperature induced by the nanotube elongation. MD simulations for a (8,8) CNT fully clamped at one end and free on the other.

Figure 5.8b shows that the slope of the expected dependence is positive, in contrast to what we measure. Moreover, the frequency shift $\Delta\omega_0(T = 300\ \mathrm{K})/\omega_0 = 3.0 \times 10^{-5}$ is much smaller in magnitude than the measured value $\Delta\omega_0(T = 300\ \mathrm{K})/\omega_0 \simeq -2.2 \times 10^{-2}$. This shows that the Duffing nonlinearity together with the thermal vibrations cannot describe our experimental findings.

Another explanation for our data could be related to the diffusion of adsorbed atoms along the nanotube. Mechanical vibrations lead to a force that pushes atoms towards the antinode of the mode [132]. Enhancing the vibrational amplitude of the fundamental mode results in more atoms near the nanotube free end and, therefore, a larger effective mass of the mode and a lower resonance frequency. However, we observe the opposite behavior in Fig. 5.8a. This shows that the effect of the diffusion of adsorbed atoms is smaller than that of the Duffing nonlinearity so that it cannot account for the measured T dependence of ω_0.

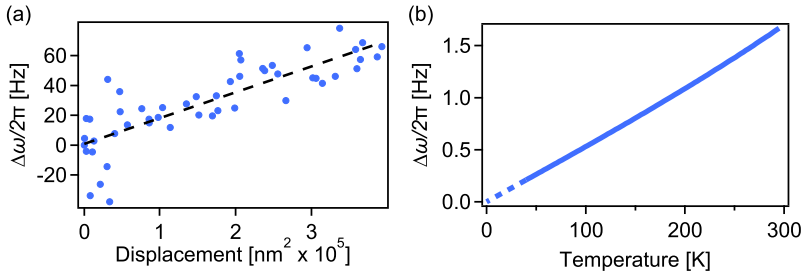

FIGURE 5.8: Estimation of the Duffing constant and its effect on the temperature dependence of the resonance frequency for device A. (a) Variation of the resonance frequency measure as a function of driven vibrational amplitude measured at $T = 100\,\mathrm{K}$. (b) Estimated frequency shift as a function of temperature due to the Duffing constant and the thermal vibrations.

5.5 Comparing the measurements with numerical simulations

These measurements can be captured by molecular dynamics (MD) simulations of the nanotube cantilever dynamics. The temperature dependence of the resonance frequencies of the lowest energy bending modes obtained from the MD simulations behaves in the same way as those we measure (Figs. 5.6a,b). The associated slope estimated for different nanotube chiralities leads to $\Delta Y(T)/Y \cdot 1/T = -(79 \pm 6)$ ppm/K, which is rather similar to the measured value. This suggests that the thermal behavior of the Young's modulus in our measurements is related to the lattice dynamics of nanotubes.

We employ a second method to directly compute the Young's modulus from the energy dispersion of the nanotube phonon modes. For this, we evaluate the free energy $F(T, \epsilon)$ of the phonon modes at T and strain ϵ with the quasi-harmonic approximation, yielding

$$Y(T) = \frac{1}{V_0(T)} \left(\frac{\partial^2 F(T, \epsilon)}{\partial \epsilon^2} \right)_{\epsilon=0}, \tag{5.5}$$

where $V_0(T)$ is the equilibrium volume at this temperature. The resulting $Y(T)$ dependence is also consistent with the measurements (Figs. 5.6a,b). The slope for different chiralities is $\Delta Y(T)/Y \cdot$

$1/T = -(104 \pm 102)$ ppm/K. The variation of the slope is larger than that obtained with molecular dynamics; this difference may be due to the infinite nanotube length and the purely linear vibrational dynamics considered in the quasi-harmonic approximation method, while the lengths in the molecular dynamics simulations are much shorter, that is, less than 40 nm. Overall, the experimental findings are fairly consistent with both models considering the typical differences between the values of Y of nanotubes obtained with different experimental and theoretical methods [101, 104, 126–129]. Both theoretical models are described in more detail in Sec. A.2.

5.6 Discussion of results

These results show how the measured fundamental mechanical modes are linked to phonons via the Young's modulus. An alternative way to describe this link is to consider the coupling of the measured mechanical modes with the thermal bath made of the phonons of the nanotube. In other words, the measured T dependence of ω_0 is related to the phonon thermal bath. The phonon thermal bath in our experiments likely operates in the Akhiezer limit [133]. As discussed in the next paragraph, over the temperature range that we measure, the phonon modes in nanotubes with energy $\hbar\omega_k$ similar to $k_B T$ have decay rates $1/\tau_k$ larger than ω_0, since $\tau_k \approx 10$ ns was measured for breathing modes at $T = 5$ K [134] and we estimate τ_k to be typically in the $10 - 1000$ ns range for the longitudinal and twist modes [135] (The estimation of τ_k for high-energy bending modes is complicated and beyond the scope of this work.) This sets the Akhiezer limit $\omega_0 \tau_k \ll 1$ at least for the breathing, longitudinal, and twist modes [132]. It involves three-phonon processes, where one vibration quantum of the measured mode is absorbed together with the absorption and the emission of high-energy phonons with frequencies ω_k and $\omega_{k'}$, respectively. The sizeable decay rates of the high-energy phonons lead to uncertainty in their energy. This lifts to some extent the restriction associated with the energy conversation of the three-phonon process, $\omega_0 = \omega_k - \omega_{k'}$, which holds in the Landau-Rumer limit when $\omega_0 \tau_k \gg 1$. For this reason, the resonance frequency reduction and the relaxation in the Akhiezer limit are expected to be larger than that in the

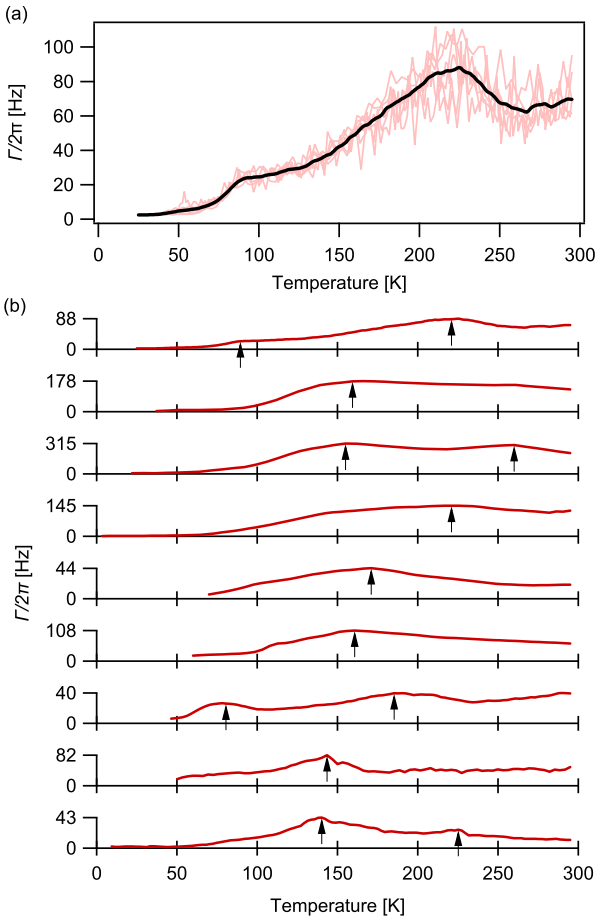

FIGURE 5.9: (a) Temperature dependence of the mechanical linewidth for device A. The black line is the average of different temperature traces (red lines). (b) Temperature dependence of the linewidth for all the measured nanotubes, from device A at the top to device I at the bottom; the associated resonance frequencies are 54 kHz, 96 kHz, 194 kHz, 77 kHz, 57 kHz, 108 kHz, 44 kHz, 58 kHz, 48 kHz. The arrows indicate peaks in dissipation.

Landau-Rumer limit over the studied temperature range. The thermoelastic limit [47] does not apply for nanotubes, since the model relies on phonons that locally reach thermal equilibrium at different temperatures on the two sides of the beam cross-section, which is not realistic for such narrow resonators.

We estimate the decay rates for different phonon modes using the expressions derived by de Martino et al. [135]. For the longitudinal phonon modes, the decay rate due to phonon-phonon interactions is given by

$$\tau_{\mathrm{L}}^{-1} = \frac{\hbar}{4\pi\rho r^4}\left\{\frac{\sqrt{k_{\mathrm{ph}}r}}{2^{5/4}}\coth\left(\frac{\hbar v_{\mathrm{L}}k_{\mathrm{ph}}}{4k_{\mathrm{B}}T}\right) + \sqrt{2}\exp\left(\frac{-\hbar v_{\mathrm{L}}}{2\sqrt{2}rk_{\mathrm{B}}T}\right)\sinh\left(\frac{\hbar v_{\mathrm{L}}k_{\mathrm{ph}}}{2}\right)\right\}, \quad (5.6)$$

where $\hbar$ is the reduced Planck constant, $\rho = 3.8 \times 10^{-7}\,\mathrm{kg/m^2}$, r is the nanotube radius, k_{ph} is the phonon wave number and $v_{\mathrm{L}} = 1.99 \times 10^4\,\mathrm{m/s}$ is the longitudinal speed of sound. For the twist phonon modes the decay rate is

$$\tau_{\mathrm{T}}^{-1} = \frac{\hbar}{2\rho}\left(\frac{v_{\mathrm{T}}}{v_{\mathrm{L}}}\right)^{7/2}\frac{2^{1/4}\left(k_{\mathrm{ph}}r\right)^{3/2}}{8\pi r^4}\left\{\coth\left(\frac{\hbar v_{\mathrm{T}}k_{\mathrm{ph}}}{4k_{\mathrm{B}}T}\right) + 2^{5/4}\left(\frac{v_{\mathrm{T}}}{v_{\mathrm{L}}k_{\mathrm{ph}}r}\right)^{3/2}\exp\left(-\frac{\hbar v_{\mathrm{T}}^2}{2\sqrt{2}v_{\mathrm{L}}rk_{\mathrm{B}}T}\right)\sinh\left(\frac{\hbar v_{\mathrm{T}}k_{\mathrm{ph}}}{2k_{\mathrm{B}}T}\right)\right\} \quad (5.7)$$

where $v_{\mathrm{T}} = 1.23 \times 10^4\,\mathrm{m/s}$. We calculate the decay rates for different phonon energies E_{ph}. The wave number is $k = E_{\mathrm{ph}}/\hbar v_{\mathrm{L}}$ for longitudinal and $k = E_{\mathrm{ph}}/\hbar v_{\mathrm{T}}$ for twist phonons and $r = 1\,\mathrm{nm}$. Figs. 5.10 (a)-(b) show the respective temperature dependencies of τ_{L} and τ_{T}.

It is expected that the phonon thermal bath significantly contributes to the measured dissipation via the Akhiezer relaxation, since a thermal bath results in a resonance frequency reduction as well as dissipation, both of them being related through the Kramers–Kronig relations [82]. Figures 5.9a,b show the measured temperature dependence of the mechanical linewidth of the different measured devices. The measurements feature one

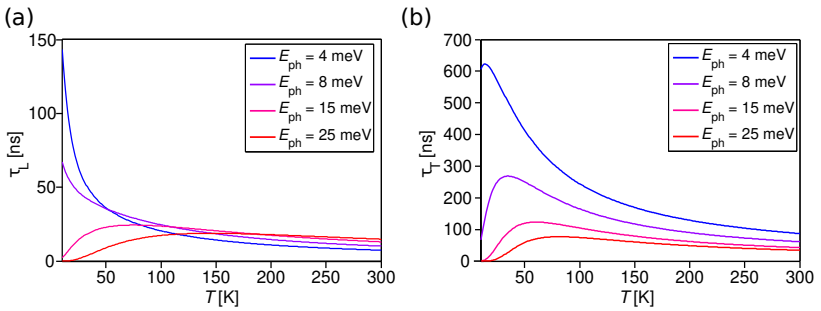

FIGURE 5.10: Temperature dependence of the phonon decay times of the (a) longitudinal and (b) twist phonon modes for different phonon energies E_{ph}.

or two peaks of dissipation at some specific temperatures. These observed peaks could arise from the Akhiezer relaxation. The Akhiezer dissipation rate depends in a complicated way on the number of phonon modes with energy $\hbar\omega_k \leq k_B T$, their population, and their decay rate [132]. The temperature dependence of the Akhiezer dissipation rate could feature one or more peaks in dissipation, especially since the phonon density of states varies up and down as a function of energy [135, 136] and the temperature behavior of the decay rate changes for different phonon modes. In addition, the dissipation peaks could emerge at different temperatures for different nanotube chiralities, since the phonon energy dispersion is chirality dependent.

We show here that the measured temperature dependence of the dissipation cannot be described by the model that is used in the literature [137, 138] to quantify dissipation due to defects. Peaks in dissipation when sweeping temperature is often attributed to microscopic defects. These defects are modeled by double-well potentials with barrier height V_0 and asymmetry Δ between the two wells. At the high temperature of our experiments, the passage from one well to the other well is thermally activated with a characteristic time

$$\tau_d = \tau_{d0} \exp\left(V_0/k_B T\right), \tag{5.8}$$

with $1/\tau_{d0}$ the attempt rate to overcome the barrier. Assuming that all defects have similar V_0, Δ, and τ_{d0}, a peak in dissipation occurs when the characteristic rate $1/\tau_d$ of the defects

matches the mechanical resonance frequency, $1/\tau_d = \omega_0$. Our measurements in Fig. 5.9b show dissipation peaks at different temperatures. Using the values of these temperatures together with $1/\tau_d = \omega_0$, we construct a plot of τ_d as a function of T (Fig. 5.11a). Despite the relatively large spread in the values of τ_d in Fig. 5.11a, the data cannot be described by an exponential behavior, suggesting that $\exp V_0/k_BT \sim 1$ in the measured temperature range in order to force a reasonable description of the data by Eq. 5.8. Such an analysis would lead to an unrealistically long $\tau_{d0} \sim 2 \times 10^{-6}$ s, considering that τ_{d0} is typically in the 10^{-13} s – 10^{-11} s range [137–139]. If we were considering two or three different types of defects, each of them with well-defined characteristics V_0, Δ and τ_{d0}, we would also obtain τ_{d0} in the μs range. Therefore, the model based on defects with narrow characteristics distribution cannot account for our measurements. Another possibility with the double-well potential model is to assume a broad distribution of the defect characteristics V_0 and Δ [137–139]. A peak in dissipation can be obtained in a specific parameter space region. The peak always features a negative curvature between $T = 0$ K and the peak temperature (Fig. 5.11b), which is just the opposite of what is observed in our experiments (Fig. 5.9). Overall, our measurements cannot be explained by the double-well potential model with neither a narrow nor a broad defect characteristics distribution.

5.7 Conclusion and Outlook

In conclusion, we report the first experimental study of the temperature dependence of the Young's modulus of a nanoscale system. The measurements are consistent with theoretical predictions based on the nanotube lattice dynamics. This indicates that the phonon thermal bath plays an important role in the dynamics of nanotube cantilevers, including thermal vibrational noise, dissipation, and resonance frequency reduction. Further theoretical work is needed to compute the Akhiezer relaxation in nanotubes beyond the models used so far, where a single decay rate is employed for all the high-frequency phonon modes [138, 140, 141]. This may be achieved with a microscopic theory [132] taking into account the phonon energy dispersion [136] and the

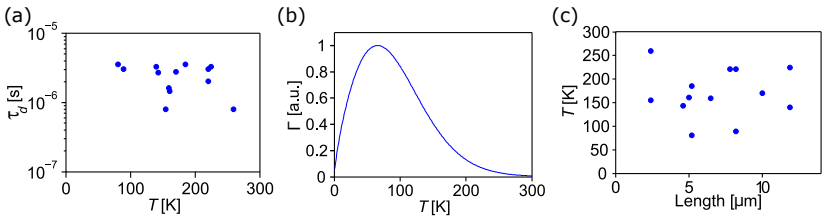

FIGURE 5.11: (left) Characteristic time τ_d to overcome the barrier height as a function of temperature, obtained from all the measured devices as explained in the text. (right) Mechanical dissipation due to a distribution of defects as a function of temperature, calculated using Eq. A1 from reference [139] with $\tau_{d0} = 10^{-12}$ s, $V_0 = 100$ meV, $\Delta = 20$ meV, $\omega_0/2\pi = 100$ kHz and $\zeta = 0.25$. (c) The temperature of the dissipation peaks as a function of the nanotube cantilever length. The data do not indicate any correlation between the dissipation peak temperature and the length. The same is observed for other geometric properties of the nanotubes, such as radius, number of walls and radius/length ratio (not shown).

energy decay of high-frequency phonons [135]. It will be interesting to see whether such a model leads to dissipation peaks at specific temperatures as observed in our work.

Chapter 6

Thermal transport in TMD monolayers

Parts of this chapter were published in:

Optomechanical measurement of the thermal transport proprieties of transition metal dichalcogenide monolayers
N. Morell, S. Tepsic, A. Reserbat-Plantey, A. Cepellotti, M. Manca, A. Isacsson, X. Marie, F. Mauri, A. Bachtold
Nano Letters 2019 19 (5), 3143-3150

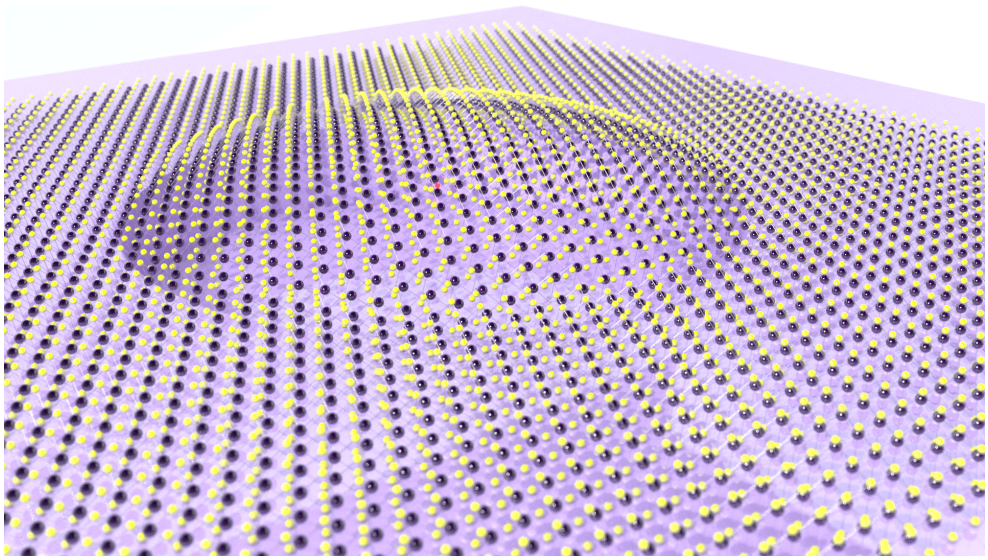

FIGURE 6.1: Visualisation of a 2D drum like TMD resonator.

6.1 Introduction

Mechanical resonators based on suspended nanoscale objects, such as monolayer semiconductors [4–6, 142], graphene [7–18], nanotubes [19–30] and semiconducting nanowires [31–38], have attracted considerable interest. Because of their small mass, such resonators become fantastic sensors of external forces and the adsorption of mass [23, 25, 29, 39]. The sensing capabilities of nano- and micro-resonators have been used with great success in recent advances in various fields. These include nano-magnetism [42, 43], surface imaging [37, 38], surface science [40, 41], light-matter interaction [34], persistent currents in normal metal rings [143] and engineered electron-phonon coupling [27]. In this work, we show how optomechanical systems can be used to study heat transport in individual low-dimensional materials.

Heat transport at the nanoscale is of major fundamental interest for a broad range of research fields, such as nanophononics [144–146], spintronics [147], quantum electron devices [148, 149] and quantum thermodynamics [150]. Heat can be controlled and measured with good accuracy in devices micro-fabricated from bulk material. By contrast, heat transport in devices based on low-dimensional materials cooled at low temperature is still in its infancy. Measuring their thermal conductance at cryogenic temperature is a challenging task. It requires the fabrication of sophisticated devices, which incorporate local heaters and thermometers and careful calibration of the latter [151, 152]. The difficulty of fabricating reliable devices has hindered progress in the field for many years.

Lattice vibrations are the main carriers of heat in a large variety of low-dimensional materials, including carbon nanotubes [152, 153], graphene [154] and semiconductor monolayers [155]. Heat transport has been intensively studied at room temperature and above using Raman measurements [156–163] and scanning probe microscopy [164, 165]. Heat transport enters into interesting regimes at low temperatures, such as the dissipationless transport through low-dimensional materials in the ballistic regime [151, 152, 166] and the phonon hydrodynamic regime predicted in monolayers [55, 56]. The interpretation of heat transport measurements can be difficult since the thermal conductance depends on various quantities that have not been

measured independently thus far. These include the heat capacity and the phononic mean-free path. Recently, new methods have been reported to measure the electron contribution of the thermal conductivity of graphene down to low temperature [167, 168].

Heat transport measurements in low-dimensional materials have mainly consisted of probing the thermal conductance K, that is, how well the system conducts heat. In optomechanics, it is possible to measure how quickly the mechanical resonator conducts heat [96, 119, 169]. The characteristic time τ for the heat to travel out of the resonator introduces a retarded force acting on the mechanical resonator [93, 95].

Here, we combine two methods to measure K and τ in an optomechanical resonator based on a vibrating $MoSe_2$ monolayer. This allows us to unravel the thermal properties of low-dimensional materials down to cryogenic temperature and with a device that is simple to fabricate. Our measurements indicate that the phonon transport is diffusive above ~ 100 K, while the majority of phonon carriers are ballistic over the size of the device at low temperature. The temperature dependence of the specific heat capacity approaches a quadratic dependence, the signature of two-dimensional lattices. Both the thermal conductance and the specific heat capacity measurements can be described by predictions based on first-principles.

6.2 TMD resonator

The mechanical resonator consists of a $MoSe_2$ monolayer drum as depicted in Fig. 6.2. The drum is fabricated with the dry transfer of $MoSe_2$ monolayers using PDMS stamp [170] over a highly doped Si substrate with pre-patterned holes. $MoSe_2$ monolayers are obtained from mechanical exfoliation of crystals purchased from 2D Semiconductors. The device is measured in a cryostat whose temperature can be set between 3 and 300 K. Photoluminescence spectra at 3 K feature narrow peaks associated with two-dimensional excitons and trions with a wavelength at ~ 762 nm and ~ 748 nm [91], respectively, which is in agreement with previous reports [171, 172]. Photoluminescence maps are homogeneous [6]. These measurements confirm that the drums are made from $MoSe_2$ monolayers. The metal electrode attached

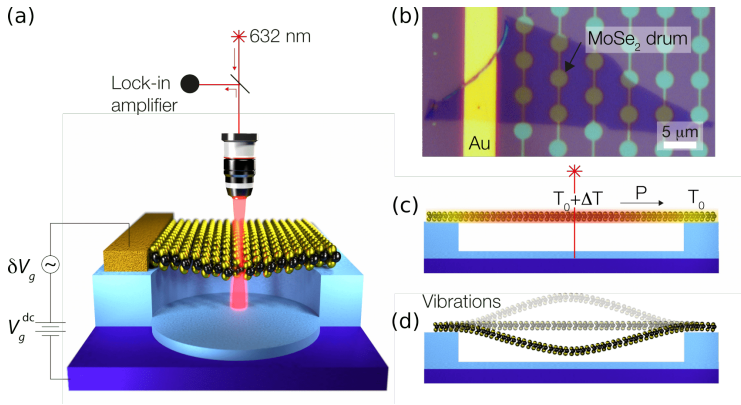

FIGURE 6.2: (**a**) Schematic of the optomechanical device. The mechanical vibrations are driven capacitively and detected by optical interferometry [6]. The $MoSe_2$ monolayer is a mobile absorber in an optical standing wave produced by a 633 nm probe laser. The modulated laser reflection intensity is measured with an avalanche photo-detector feeding a lock-in amplifier. (**b**) Optical microscopy image of a typical device. (**c**) Heat transport induced by the absorption of the laser power. A temperature difference ΔT is created from the heat flow. (**d**) Detection of the laser-induced temperature rise ΔT using the fundamental mechanical mode of the optomechanical resonator.

to the $MoSe_2$ flake is used to apply an electrostatic force on the drum (Fig. 6.2a,b); it does not affect the thermal transport.

Mechanical vibrations are detected by optical interferometry [6, 95]. A continuous-wave laser impinges on the center of the $MoSe_2$ membrane and the reflected laser light intensity is modulated by an amount proportional to the displacement of the resonator. The laser forms a standing wave pattern in the direction perpendicular to the Si substrate, such that the displacement of the monolayer modifies its optical absorption. The laser spot has a measured radius of about 350 nm. The fact of measuring the mechanical resonator with the laser beam modifies the dynamics of the mechanical vibrations by a small amount – increasing the laser power modifies the resonance frequency and the resonance linewidth. This backaction has two components, the static and the dynamical backaction. The former allows us to quantify K and the latter τ.

6.3 Thermal conductance

We measure the thermal conductance in a way similar to the well-established method based on Raman measurements employed at room temperature [156, 157]. The static backaction of the laser beam is a simple absorption heating effect, which results in a temperature gradient ΔT between the center of the membrane and its circular clamp (Fig. 6.2c). The heat flow is given by the power P absorbed in the membran [91]. In a Raman measurement, ΔT is quantified by the frequency shift of Raman-active peaks. In our case, ΔT is measured by the frequency shift Δf_{T} of the fundamental mechanical mode (Fig. 6.2d). As a result, the equivalent thermal conductance is $K = P/\Delta T$. Mechanical $MoSe_2$ drums with their high-quality factor [6] are extremely good temperature sensors, allowing us to measure the linear thermal conductance down to 3 K. This is a significant improvement compared to Raman measurements, which are typically operated at 300 K or above because the detection of the frequency shift of Raman-active peaks requires comparatively large P.

Figures 6.3a,b show the temperature dependence of the equivalent thermal conductance. The conductance is obtained from the slope $\Delta f_{\mathrm{m}}/\Delta P$ in Fig. 6.3a using the calibration slope $\Delta f_{\mathrm{m}}/\Delta T$ in Fig. 6.4c. The conductance is measured in the linear regime because the applied P is low. The largest ΔT remains below 1 K. We also show that the absorption coefficient is independent of temperature and gate voltage at the laser wavelength $\lambda = 633$ nm. To ensure that the resonance frequency and the resonance linewidth Γ_{m} depend linearly on the laser power, we estimate $\Delta f_{\mathrm{m}}/\Delta P$ and $\Delta \Gamma_{\mathrm{m}}/\Delta P$ for absorbed laser powers below 35 nW when the temperature is below 40 K and 60 nW otherwise. We emphasize that the temperature profile over the surface of the drum in the measurement of $\Delta f_{\mathrm{m}}/\Delta P$ differs from that of $\Delta f_{\mathrm{m}}/\Delta T$. This results in a prefactor in the conversion from the equivalent thermal conductance K into the thermal conductivity of the monolayer, as described below.

The temperature dependence of the thermal conductance suggests diffusive transport at high temperature (Fig. 6.3b). Upon increasing temperature above ~ 100 K, the conductance decreases, which is attributed to the reduction of the mean-free path due to phonon-phonon scattering [174]. Below ~ 100 K, the conductance gets larger when increasing temperature. This indicates

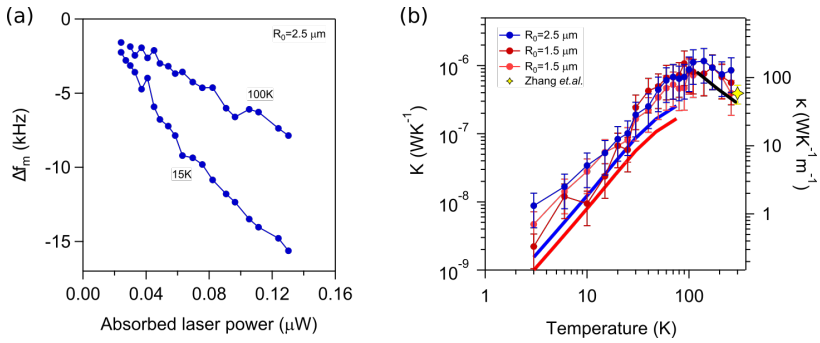

FIGURE 6.3: (**a**) Shift of the resonance frequency Δf_{m} as a function of absorbed laser power P when the drum is in the straight configuration. (**b**) Thermal conductance $K = P/\Delta T$ as a function of temperature. The right axis shows the conductivity in the diffusive regime, which is obtained using Eq. 6.4 with η=0.61. The yellow star symbol at 300 K corresponds to the thermal conductivity measured with the Raman method [161]; we are not aware of another measurement of the thermal conductivity of $MoSe_2$ monolayers. The black line shows the conductivity in the diffusive regime for an infinitely large monolayer computed by solving the Boltzmann transport equation as in Ref. [173]. The red and the blue line corresponds to the conductance in the ballistic regime computed from first principles for the 1.5 and the 2.5 μm radius drum, respectively, using Eq. 6.5 with $\alpha = 2.1$ and $\alpha = 3.2$.

that phonon-phonon scattering is no more relevant so that the mean-free path could be limited by e.g. the device size or the grain boundaries of the crystal. The error bars of the thermal conductance in Fig. 6.3b comes from the uncertainty in the absorption coefficient A of the monolayer (Section 2 of Supplementary Information). Since we cannot measure the absorption coefficient, we choose a large uncertainty, that is, $A = 0.057 \pm 0.03$. Figure 6.3b shows that this affects the measured temperature dependence of the thermal conductance only weakly.

6.4 Photothermal characteristic time

We measure τ from the effect of the dynamical backaction on the electrostatically driven vibrations. Absorption heating from the laser beam expands the $MoSe_2$ crystal [6], which is equivalent to a force acting on the membrane. The crystal expansion responds to a change in the absorbed laser power with delay, that is, the time τ for the membrane to heat up or to cool down. The absorbed laser power oscillates in time because of the oscillating motion of the membrane in the laser interference pattern used to detect the vibrations. Overall, the photothermal force oscillates with a finite phase shift compared to the motion of the membrane. The in-phase photothermal force modifies the resonance frequency by Δf_{B} and the out-of-phase photothermal force modifies the resonance linewidth by $\Delta\Gamma_{\mathrm{B}}$ as

$$\Delta f_{\mathrm{B}} = -\frac{1}{2} f_{\mathrm{m}} \frac{\partial_{\mathrm{z}} F^{\mathrm{z}}_{\mathrm{photo}}}{k} \frac{1}{1+(2\pi f_{\mathrm{m}}\tau)^2}, \tag{6.1}$$

$$\Delta\Gamma_{\mathrm{B}} = f_{\mathrm{m}} \frac{\partial_{\mathrm{z}} F^{\mathrm{z}}_{\mathrm{photo}}}{k} \frac{2\pi f_{\mathrm{m}}\tau}{1+(2\pi f_{\mathrm{m}}\tau)^2}. \tag{6.2}$$

Here, f_{m} is the resonance frequency of the mechanical mode, k its spring constant, z the coordinate in the direction perpendicular to the membrane and $\partial_{\mathrm{z}} F^{\mathrm{z}}_{\mathrm{photo}}$ the derivative of the z-component of the photothermal force with respect to z. We infer τ from Δf_{B} and $\Delta\Gamma_{\mathrm{B}}$ for a fixed laser power using

$$\tau = -\Delta\Gamma_{\mathrm{B}}/4\pi f_{\mathrm{m}}\Delta f_{\mathrm{B}}.$$

The key to quantifying Δf_{T} and Δf_{B} is to deform the static profile of the drum with an electrostatic force (Fig. 6.4a). The

drum is straight when it is not subject to a sizeable electrostatic force. This is because the drum is mechanically stretched by the circular clamp, as shown by the strong temperature dependence of f_m (Figs. 6.4b,c); the tensile strain in the membrane is quantified by the measured dependence of f_m on the electrostatic force [6, 91]. The absorbed laser power generates a photothermal force F_{photo} that reduces the stretching force. When the drum is straight, the photothermal force is perpendicular to the motion of the vibrations, so that $\Delta f_B = 0$ (Eq. 6.1); in this straight configuration, we only measure Δf_T associated with the thermal conductance. When the drum is bent, the photothermal force modifies both Δf_T and Δf_B. We obtain Δf_B by subtracting the frequency shifts measured in the bending and the straight configurations (Section 4 of Supplementary Information). We go from a straight configuration to a bending configuration by applying a voltage V_g^{dc} onto the gate electrode.

We measure τ by comparing the resonance frequency and the resonance linewidth measured with the resonator in the straight configuration ($V_g^{dc} = 0$ V) and in the bending configuration ($V_g^{dc} = 4$ V) (details are described in Section 4 of Supplementary Information in ref. [91]). Here $V_g^{dc} = 4$ V is the largest voltage that we apply, since a larger voltage may collapse the drum onto the bottom of the trench. The associated strain is less than 1% [91]. Such a small strain is expected to have no sizeable effect on the thermal transport properties [52].

Figures 6.5(a-c) show that τ remains constant when varying temperature within the error bars of the measurements. We cannot measure τ above 100 K, since the reduced quality-factor prevents us to resolve Δf_B. Using the averaged phonon velocity $v \simeq 1300$ m/s computed by first principle [91], the average time $\langle\tau\rangle = 3.3 \pm 2.1$ ns results in a mean-free path of about 4.3 ± 2.7 μm, which is consistent with the 2.5 μm radius of the drum. This suggests that the majority of the phonon carriers are ballistic over the size of the drum.

These measurements allow us to directly quantify the equivalent heat capacity of an individual $MoSe_2$ monolayer using $C = \langle\tau\rangle K$. Figure 6.5d shows that the temperature dependence of the heat capacity approaches a T^2 dependence. This is consistent with the T^d dependence expected for two-dimensional systems in its simplest form, where $d = 2$ is the dimensionality. Previous measurements of the phononic heat capacity of

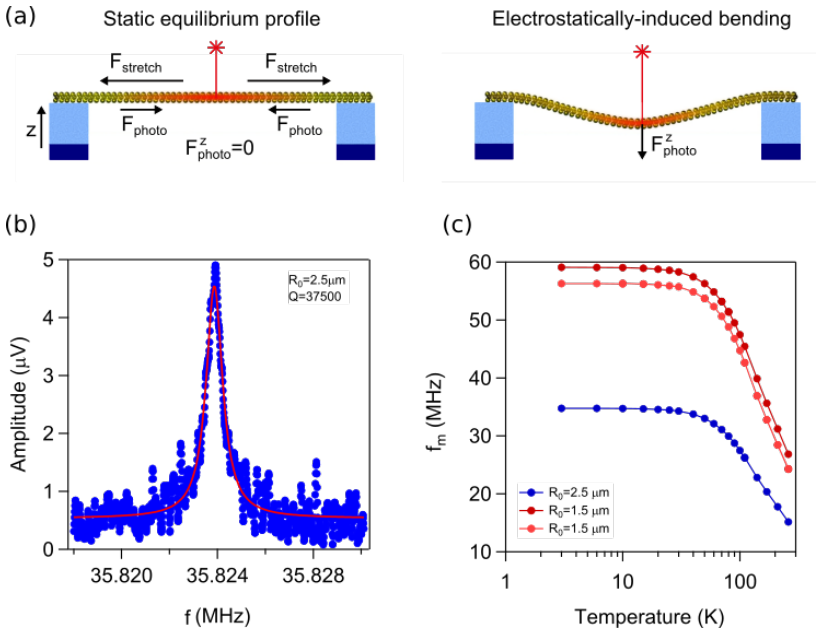

FIGURE 6.4: (**a**) Static profile of the drum controlled with an electrostatic force, by applying the tension V_g^{dc} on the back gate (Fig. 1a). In the straight configuration, the measured frequency shift is solely related to static backaction, which allows us to quantify the thermal conductance. The drum is stretched by the force F_{strech} from the circular clamp. The force F_{photo} produced by the laser beam reduces the stretching. In the bending configuration, the frequency shift also depends on dynamical backaction, because $\partial_z F^z_{photo}$ is finite. This allows us to quantify the time τ for the heat to travel out from the drum. The amplitude of the mechanical vibrations (< 1 nm) is smaller than the static displacement ($\lesssim 10$ nm) in the bending configuration. (**b**) The response of the displacement amplitude of the mechanical mode as a function of the frequency of the driving force at 3 K. (**c**) The resonance frequency of the mechanical mode as a function of temperature for three different devices when the drum is in the straight configuration.

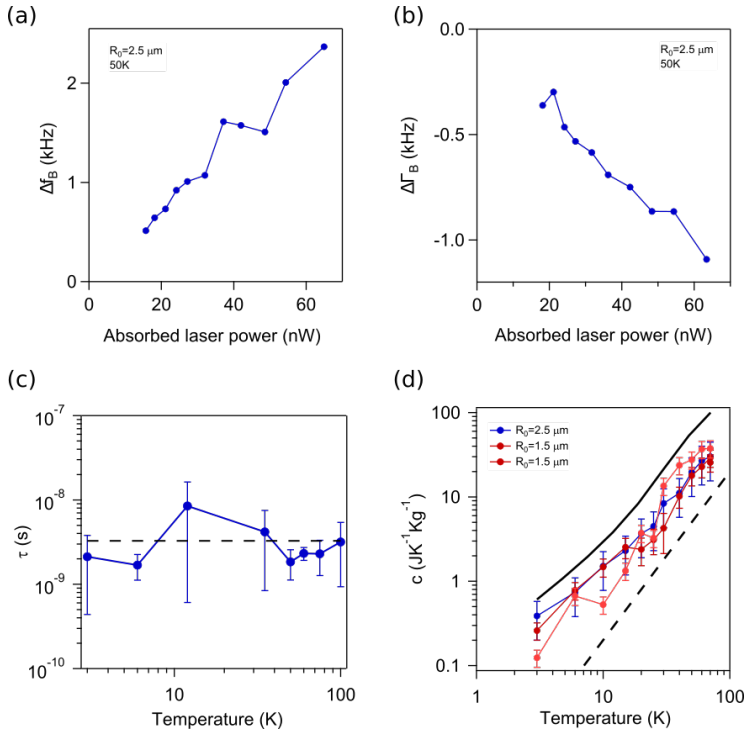

FIGURE 6.5: (**a,b**) Shifts of the resonance frequency Δf_B and the mechanical bandwidth $\Delta\Gamma_B$ as a function of absorbed laser power P. We obtain Δf_B and $\Delta\Gamma_B$ by subtracting the frequency shift and the bandwidth shift measured in the bending configuration from that measured in the straight configuration. (**c**) Time for the heat to travel out of the drum as a function of temperature. The large error bars at 12 and 35 K are due to the drift of the resonance frequency caused by the automatized heating and cooling switches in our cryofree cryostat. The dashed black line corresponds to the averaged τ. (**d**) Specific heat capacity as a function of temperature. We convert $C = \langle\tau\rangle K$ into c using Eq. 6.3 with $\beta = 0.86$. The black dashed line corresponds to the T^2 dependence. The black continuous line corresponds to the specific heat capacity computed from first-principles. Since the displacement sensitivity of the 1.5 μm radius drums was not good enough to measure τ, we estimate $\langle\tau\rangle$ from the value measured with the 2.5 μm radius drum and the radius ratio. The error bars come from the uncertainty in $\langle\tau\rangle$ and K.

nano-materials were carried out by packing them in macroscopic ensembles, such as films of nanotube ropes [175] and powders of $MoSe_2$ multilayered crystals [176]. Such ensemble measurements suffer from the coupling between nano-systems, which modifies the heat capacity at low temperature.

6.5 Thermal conductivity and specific heat capacity

The temperature profile along the heat flow has to be considered when evaluating the specific heat capacity c and the thermal conductivity κ of $MoSe_2$ monolayers (Figs. 6.3b and 6.5d). The temperature is non-uniform over the surface of the drum when measuring the slope $\Delta f_m/\Delta P$, while it is uniform during the measurement of the calibration slope $\Delta f_m/\Delta T$. These different temperature profiles add a geometrical constant in the conversion from C and K into c and κ. In the ballistic regime, the temperature is taken as constant within a disc corresponding to the region illuminated by the laser beam of radius r_0; outside this region, the temperature drops as $1/r$ along the radial coordinate r because of the conservation of heat flow in our disc geometry [91]. This contrasts with the constant temperature profile along ballistic conductors with uniform width. In the diffusive regime, the temperature decreases logarithmically along r due to phonon scattering events [157, 177, 178]. The measured C and K are converted into c and κ using

$$c = \frac{C}{\pi R_0^2 t \rho}\beta, \tag{6.3}$$

$$\kappa = \frac{K}{2\pi t}\eta, \tag{6.4}$$

where R_0 is the radius of the suspended drum, $t = 0.64$ nm the thickness of the monolayer, and ρ the mass density of $MoSe_2$. The geometrical constants β and η are of the order of one and depend on R_0, r_0 and the temperature profile [91]. The conductivity in Fig. 6.3b is determined in the diffusive regime only.

The measured temperature dependence of κ above ~ 100 K can be described by first-principles calculations on $MoSe_2$ monolayers in the diffusive regime (Fig. 6.3b), whereas the measured

temperature dependencies of c and K below $\sim$ 100 K are consistent with predictions in the ballistic regime (Figs. 6.3b and 6.5d). For the comparison between measurements and theory, we derive the ballistic conductance in our peculiar disc geometry assuming that the inner reservoir is given by the radius r_0 and the outer reservoir by R_0. We obtain

$$K = 2\pi r_0 t\alpha \cdot \frac{\rho c v}{2}, \tag{6.5}$$

$$v = \frac{\sum_{q,s} C_{q,s} \frac{2|v_{q,s}|}{\pi}}{\sum_{q,s} C_{q,s}}, \tag{6.6}$$

where $C_{q,s} = \frac{dn_{q,s}}{dT}\hbar\omega_{q,s}$ is the specific heat of the phonon of the branch s with momenta q, $\omega_{q,s}$ the phonon pulsation, $n_{q,s}$ the Bose occupation factor and $v_{q,s}$ the group velocity. The constant α is another geometric factor of the order of one like β and η. These three geometrical factors are described in ref. [91]. The phonon properties of the monolayer lattice are calculated using density functional perturbation theory. Instead, in the diffusive regime, the conductivity is derived by an exact solution of the Boltzmann transport equation taking into account three-phonon interactions and isotopic scattering [173]. In such a calculation, we use scattering rates derived by first principles that depend on the energy and momentum of the involved phonons, in contrast to the single empirical effective time τ used in Eqs. 6.1 and 6.2, which describes the characteristic time for the heat to travel out of the resonator. The conductivity derived with a homogenous temperature gradient (∇T) can be compared to the measured conductance through Eq. 6.4, which maps transport with non-homogenous ∇T to that with homogenous ∇T. The derivation of Eqs. 6.3-6.6 and information on the first-principle calculations can be found in Section 5 of Supplementary Information. The reasonably good agreement between measurement and theory in Fig. 6.3b suggests that the resistance at the interface between the monolayer and the substrate does not contribute significantly to the thermal transport. Future work will be carried out on smaller diameter drums where the resistance of the interface is expected to become comparatively larger.

6.6 Conclusion

Our optomechanical measurements provide a detailed picture of thermal transport in monolayer $MoSe_2$ lattices down to cryogenic temperature. Our work opens the possibility to measure thermal properties in a large variety of different two-dimensional materials because the devices required for these measurements are simple to fabricate. We will improve the quality factor of drums by e.g. increasing their diameter to measure τ and the heat capacity up to room temperature. This new measurement method may allow the exploration of the phonon hydrodynamics regime, which is expected to be robust in monolayer systems [55, 56]. This regime is interesting because heat is carried by collective excitations of phonon states. This gives rise to a new type of sound propagation, called second sound. The measurement of τ should enable the direct access of the velocity of the second sound. Besides, this new measurement method may shed light on the divergence of the thermal conductivity in two dimensions, when the size of the system increases [151]. The origin of this behavior is under active investigation with different interpretations based on either the dimensionality of the system or the special phononic states that remain ballistic over extraordinarily long distances [52–54]. Optomechanical measurements also enable the study of the anisotropic thermal conductivity, as recently demonstrated in 10-100 nm thick black phosphorus crystals at room temperature [179].

Chapter 7

Conclusion

7.1 Summary

In this thesis, we studied nanomechanical resonators based on low dimensional materials in a temperature range from room temperature down to a few Kelvins. Extraordinary sensing capabilities of these systems are used to investigate the thermal dependence of the crystal properties of low dimensional materials.

In Chapter 5 we employed the hybrid optomechanical scheme to investigate the thermal behavior of stiffness in carbon nanotubes. We demonstrated that the stiffness of the nanotubes is related to its phonon thermal bath. Phonon thermal bath also plays important role in the dynamics of nanotube cantilevers, such as thermal vibrational noise, dissipation, and resonance frequency reduction. We show evidence that the phonon thermal bath in our experiments operates in the Akhiezer limit.

In Chapter 6 we used excellent sensing capabilities of mechanical resonators based on TMD monolayer to investigate thermal properties of TMD monolayers down to cryogenic temperature. We measured the temperature dependence of thermal conductivity and phonon mean free path in $MoSe_2$ monolayer. These measurements indicate the crossover between the diffusive and the ballistic regime in thermal transport.

7.2 Outlook

The work presented in this thesis offers possibilities for a variety of future experiments and theoretical work.

Regarding the work in chapter 5, further theoretical work is necessary to investigate the role of phonon thermal bath in the

dynamics of nanotube resonators. It is of interest to compute the Akhiezer relaxation in nanotubes beyond the models used so far. This may be achieved with a microscopic theory taking into account the phonon energy dispersion and the energy decay of high-frequency phonons. It would be interesting to see whether such a model leads to dissipation peaks at specific temperatures as observed in our work.

Our work in chapter 6 opens the possibility to study thermal properties in a variety of different two-dimensional materials. By fabricating 2D mechanical resonators with bigger diameters it would be possible to measure interesting thermal transport regimes like phonon hydrodynamics transport. This regime is interesting because heat is carried by collective excitations of phonon states. Optomechanical measurements can also open the possibility to investigate other types of 2D materials like superconducting $NbSe_2$ and its superconducting phase transition.

Appendix A

Additional information on chapter 5

A.1 Eigenmodes and spring constant of the device

In this section, we discuss in more depth the eigenmode shape of the nanotube cantilever with the platinum particle at the free end.

A.1.1 Model

The Euler-Bernoulli partial differential equation (PDE) that describes the motion $y(x,t)$ of a vibrating beam is

$$\frac{\partial^2 y}{\partial t^2} + \frac{YI}{\rho A}\frac{\partial^4 y}{\partial x^4} = 0. \tag{A.1}$$

In Eq. A.1, Y is the Young's modulus, I is the second moment of the cross-sectional area A and ρ is the density of the carbon nanotube (CNT) with length l. Solution of Eq. A.1 is

$$y(x,t) = \cos\omega_n t\,[c_1\cos\alpha_n x + c_2\sin\alpha_n x + c_3\cosh\alpha_n x + c_4\sinh\alpha_n x], \tag{A.2}$$

with radial frequency $\omega_n = c{\alpha_n}^2$ and $c = \sqrt{\frac{YI}{\rho A}}$. In Eq. A.2, α_n is the wave number whereas $c_1,..c_4$ are constants that will be determined by satisfying boundary conditions. In the presence of a particle with mass m_{bead} at the free end, the boundary conditions to satisfy become: $y\mid_{x=0} = \partial y/\partial x\mid_{x=0} = 0$ and $\partial^2 y/\partial x^2\mid_{x=l} = 0$,

$-YI\frac{\partial^3 y}{\partial x^3}\ |_{x=l} = m_{\text{bead}} c^2 {\alpha_n}^4 y_{x=l}$ [90], in which the effect of the bead's rotary inertia is neglected. Implementing these conditions in Eq. A.2 leads to the following characteristic equation

$$\cos\Omega_n \cosh\Omega_n + 1 + m^*\Omega_n \left(\sinh\Omega_n \cos\Omega_n - \sin\Omega_n \cosh\Omega_n\right) = 0, \quad \text{(A.3)}$$

where eigenvalues $\Omega_n = \alpha_n l$ are solutions of Eq.A.3 with $m^* = m_{bead}/m_{beam}$. The eigenmodes associated with the eigevalues can then be obtained as

$$\Phi_n(x) = \cos(\Omega_n x) - \cosh(\Omega_n x) - \frac{\cos(\Omega_n) + \cosh(\Omega_n)}{\sin(\Omega_n) + \sinh(\Omega_n)}(\sin(\Omega_n x) - \sinh(\Omega_n x)). \quad \text{(A.4)}$$

Figure A.1 shows the variation of the first three eigenfrequencies as a function of m^*. When the ratio between the mass of the bead at the free end and the mass of the beam becomes large, the mode shapes approach those of a beam clamped at one end and hinged at the other. The mode shapes for an increasing m^* are shown in Figs. A.2. The profile of the fundamental eigenmode is basically unchanged when increasing m^*, in contrast to what happens for the other eigenmodes.

The equivalent spring constant associated with the free-end CNT deflection for the *n-th* eigenmode, k_n, can be calculated as follows [180]:

$$k_n = \frac{YI}{l^3}\frac{\int_0^1 (\Phi_n''(x))^2 dx}{\Phi_n(1)^2}. \quad \text{(A.5)}$$

By letting $I = \pi\left(d^3 g + d g^3\right)/8$ in Eq. A.5, with g and d the thickness and the diameter of the CNT, respectively, the explicit

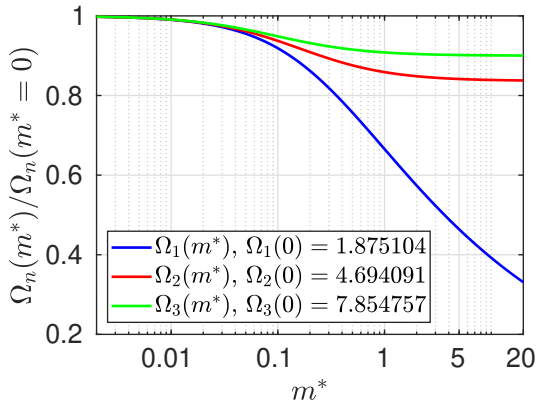

FIGURE A.1: Influence of m^* on the first three eigenfrequencies of a beam with added mass (m_{bead}) at the free end.

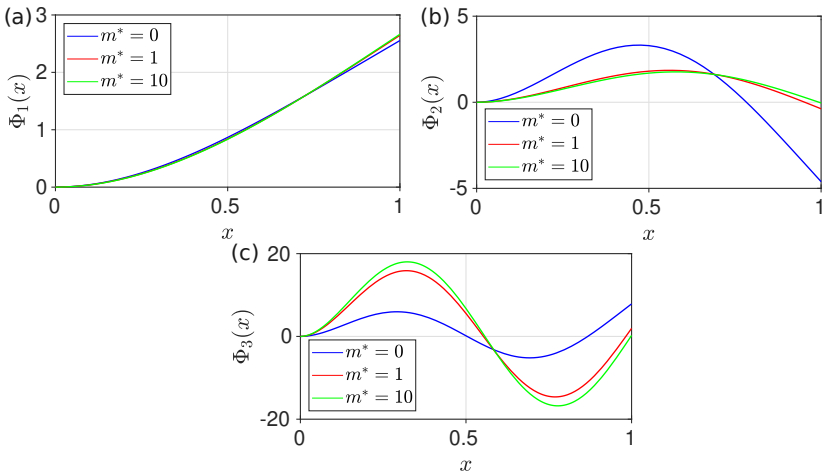

FIGURE A.2: Influence of m^* on the first three eigenmodes: (a) $\Phi_1(x)$; (b) $\Phi_2(x)$; (c) $\Phi_3(x)$. Functions normalized such that $\int_0^1 \Phi_n(x) = 1$.

form of k_n becomes

$$\begin{aligned} k_n = & \frac{\pi \Omega_n^3 Y \left(d^3 g + d g^3\right)}{64 l^3} \\ & \times \frac{-\Omega_n \cos(2\Omega_n) + \Omega_n \cosh(2\Omega_n)}{(\sin\Omega_n \cosh\Omega_n - \cos\Omega_n \sinh\Omega_n)^2} \\ & \times \frac{4\Omega_n \sin\Omega_n \sinh\Omega_n - 2\cos\Omega_n \sinh\Omega_n}{(\sin\Omega_n \cosh\Omega_n - \cos\Omega_n \sinh\Omega_n)^2} \\ & \times \frac{\sin(2\Omega_n) \cosh^2\Omega_n}{(\sin\Omega_n \cosh\Omega_n - \cos\Omega_n \sinh\Omega_n)^2} \\ & + \frac{2\cosh\Omega_n \left(\sin\Omega_n - \cos^2\Omega_n \sinh\Omega_n\right)}{(\sin\Omega_n \cosh\Omega_n - \cos\Omega_n \sinh\Omega_n)^2}. \end{aligned} \tag{A.6}$$

The effect of the added particle at the free end of the CNT on the standard deviation equation can be now obtained using the equipartition theorem:

$$\sigma_n{}^2 = \frac{k_B T}{k_n}. \tag{A.7}$$

The expression in the special case of $m^* = 0$ reduces to Eq.27 of [104]:

$$\sigma_n{}^2 = \frac{32 k l^3 T}{\pi Y \left(d^3 g + d g^3\right) \Omega_n{}^4}. \tag{A.8}$$

The resultant standard deviation σ of the cantilever can be obtained by summing up all the independent contributions of eigenmodes. Considering the first 10 flexural modes the expression becomes:

$$\sigma^2 = \sum_{n=1}^{N=10} \sigma_n{}^2 = 0.84879167978 \frac{k_B l^3 T}{\left(d^3 g + d g^3\right) Y}. \tag{A.9}$$

The numerical coefficient in Eq. A.9 is function of the number of modes considered in the summation N and depends on the influence of the added mass. This is illustrated in Figure A.3 and reported in Tab. A.1. The standard deviation of the cantilever is primarily given by that of the fundamental eigenmode independently of the particle mass at the free end.

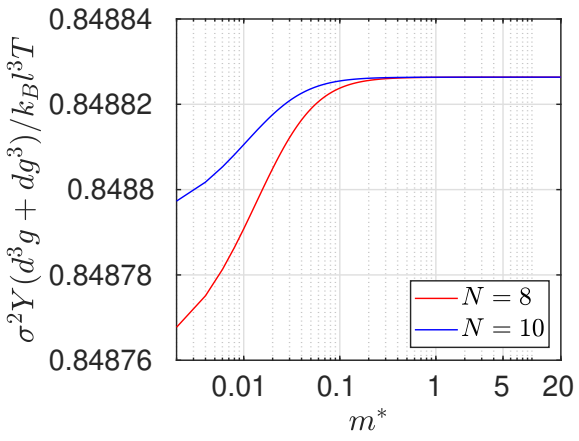

FIGURE A.3: Variation of the coefficient of Eq. A.9 as a function of m^* and while considering a different number of modes N in the summation.

TABLE A.1: Numerical values for the coefficient of the standard deviation in Eq. A.9 when taking into account the fundamental eigenmode only ($N = 1$, middle column) and the first ten eigenmodes ($N = 10$, right column).

m^*	${\sigma_1}^2 \frac{Y\left(d^3g + dg^3\right)}{k_B l^3 T}$	$\sum_{n=1}^{N} {\sigma_n}^2 \frac{Y\left(d^3g + dg^3\right)}{k_B l^3 T}$
0	0.8239457176	0.8487916797
0.1	0.8363888890	0.8488254732
0.2	0.8414352614	0.8488261068
0.5	0.8462500190	0.8488263184
1	0.8479201355	0.8488263516
2	0.8485513611	0.8488263602
5	0.8487764942	0.8488263627
10	0.8488133432	0.8488263630
20	0.8488230357	0.8488263631

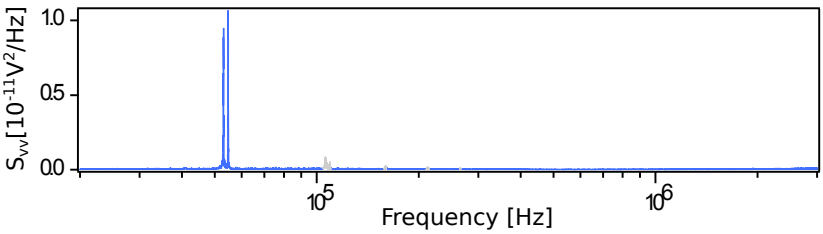

FIGURE A.4: Power spectrum of the optical reflection from device A undergoing thermal motion at 300 K. The two near-degenerate peaks are associated with the fundamental modes polarized in perpendicular directions. The spectrum is shown over a narrower frequency range in Fig. 5.1c. The nonlinearity in the detection results in higher harmonics of these modes, which are marked in gray.

A.1.2 Experiment

The model of the previous subsection indicates that the platinum particle does not affect the restoring force nor the eigenmode shape of the two fundamental eigenmodes, which are polarized in perpendicular directions, while the shapes of the higher frequency eigenmodes are strongly modified by the platinum particle. For the higher frequency eigenmodes, the displacement amplitude at the free end is suppressed to zero when the particle has a larger mass than the nanotube. For this reason, our detection method based on the reflection at the free end can only measure the two fundamental modes. This is what we observe in Fig. A.4 for device A. The resonances of the fundamental mode doublet are clearly visible, whereas the resonance frequencies of the second bending mode doublet are expected to be about 900 kHz but cannot be detected.

A.2 The theory

In this section, we give more information on the theory describing the temperature dependence of the Young´s modulus.

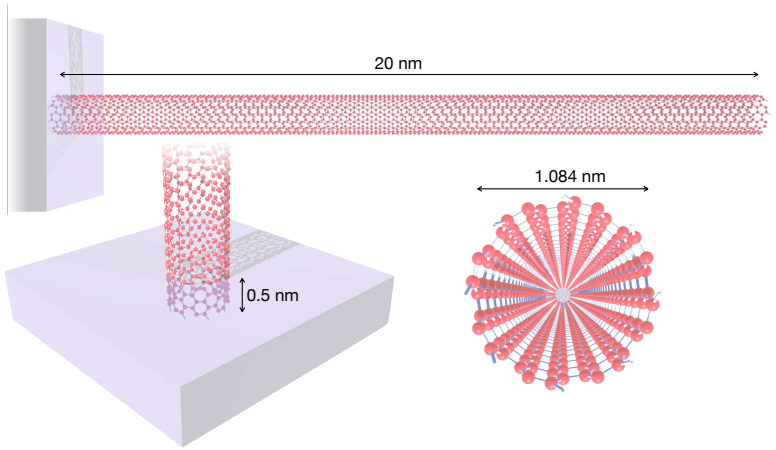

FIGURE A.5: (8,8) CNT with a total of 2624 atoms. Atoms at one end are clamped for a length of 0.5 nm. The (8,8) CNT has a radius of 0.542 nm and a total length of 20 nm.

A.2.1 Molecular dynamics simulations

We report molecular dynamics simulations of the Brownian motion of carbon nanotubes over a finite temperature range. Simulations are carried out in the Large-scale Atomic/Molecular Massively Parallel Simulator (LAMMPS) software [181] for single layer CNTs of different chirality. In Figure A.5 we showcase the geometry of one such CNT.

To account for atom-atom interactions, we use the Tersoff potential [182] with optimized parameters for lattice dynamics and phonon thermal transport [183]. We note that this potential is commonly used for simulating atomic interactions and predicting mechanical properties of carbon-based nanomaterials [184, 185].

To track the Brownian motion of the nanotube, the system is initially relaxed to ensure equilibrium at the minimum potential state. The minimization of the total potential energy is performed via the Polak-Ribiere conjugate gradient algorithm [186]. The starting point for the minimization procedure is the initial configuration of the atoms and the potential energy of the system is considered to be in a local minimum when its energy is less than 1×10^{-10} eV or when the forces are less than 1×10^{-10} eV/Å. After the relaxation, at one end, the translational degrees

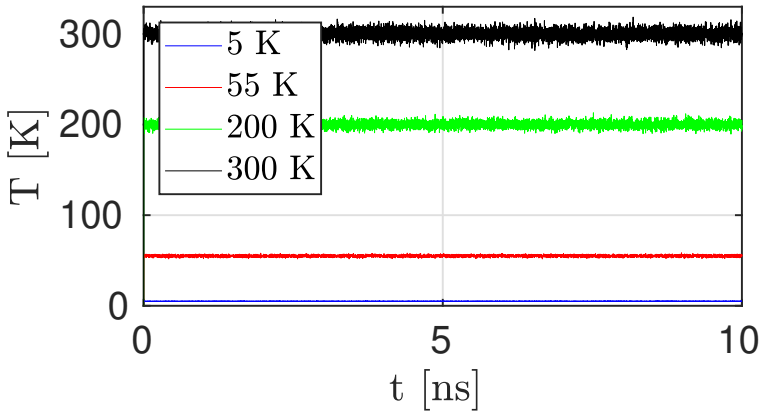

FIGURE A.6: Temperature fluctuation during the termalisation phase for a (8,8) CNT. For the thermostat temperature of 300 K we obtain a mean of 300.031 K and standard deviation of 5.69 K.

of freedom are constrained for all atoms for a length of 5 nm (see Figure A.5). This constraint is applied to obtain a CNT cantilever. Once the equilibrium position is obtained, Newton's equations are integrated using the velocity-Verlet algorithm, with a time-step $dt = 0.1$ fs to determine the variation of the position and velocity of the atoms.

To account for the thermal effects, the system is then equilibrated in a constant volume and temperature ensemble (NVT). The temperature is first brought to a certain value and then kept constant by applying the Nose-Hoover algorithm that thermostats the translational velocity of atoms [187]. The algorithm for the thermalisation is applied for 10 ns to ensure that a stable temperature is obtained (see Fig.A.6). Once thermal equilibrium is reached, the vibration response is studied in an energy-conserving ensemble (NVE). In this context, the thermal fluctuations of the CNT are monitored for 50 ns discarding an initial transient response of 10 ns and the coordinates of all atoms are saved every 2.5 ps.

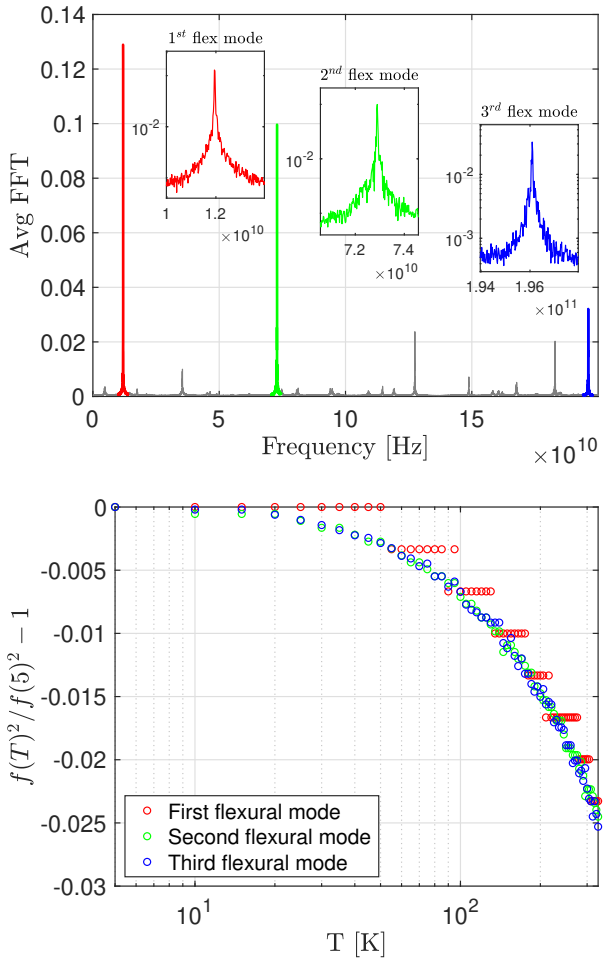

FIGURE A.7: a) The averaged frequency spectrum of all atoms for the (8,8) CNT at $T = 50$ K. b) Relative change of the square of the frequency with temperature for the first three flexural modes of the CNT from 5K to 330 K with a temperature increment of 5 K. The staircase behaviour of the first flexural mode is due to the insufficient resolution in frequency

To obtain the resonance frequencies of the CNT, we compute the FFT of the extracted time signals from molecular dynamics. An example of one such FFT averaged over all atoms is shown in Figure A.7(a) for an (8,8) CNT at 50 K. The thermal influence on the mechanics of the CNT is obtained by tracking the natural frequencies as a function of the thermostat temperature. The relative change of the square of the frequencies for the first three flexural modes for the (8,8) CNT cantilever is shown in Figure A.7(b); this quantity is equal to the relative change of the spring constant $\Delta k(T)/k$. The first three flexural modes highlight the same reduction with respect to the variation of the thermal bath. The staircase behaviour of the first flexural mode is due to the insufficient resolution in frequency (i.e. 20 MHz). Our results are compared to experimental measurements in Fig. 5.6.

We remark that the spectral analysis performed to extract the thermal behaviour of the system does not allow for an immediate classification of the natural modes of the system and their associated eigenfrequencies. However, it is possible to unravel spatial information of the nanotube from the time response data via the proper orthogonal decomposition (POD) method. The details of this technique can be found in [188] and are briefly described in Sec. A.2.1. Using POD, we can identify the eigenmodes corresponding to the resonance peaks of Figure A.7(a). The mode shapes for the first three flexural modes obtained via POD for an (8,8) CNT at 50 K are reported in Figure A.8. The procedure outlined above has been repeated in the temperature range $T \in [5, 330]$ K, for three different chiralities namely (5,10), (8,8) and (10,10) and the results are shown in Figure 5.6(b).

Proper orthogonal decomposition

The MD simulations provide the time response in a vector $\mathbf{u}$ comprising the position of $M-$atoms. The time history consists of N snapshots of the motion as $[\mathbf{u}(t_1), \mathbf{u}(t_2), \ldots, \mathbf{u}(t_N)]$. We remove the time average (mean values) of the responses by obtaining the time-varying part, $\mathbf{x}(t_i) = \mathbf{u}(t_i) - \text{mean}(\mathbf{u})$. To extract the proper orthogonal modes of vibrations, a discrete matrix $\mathbf{X}$ is first built such that each row corresponds to a time response of one atom and each column corresponds to a snapshot of the CNT at a specific time as:

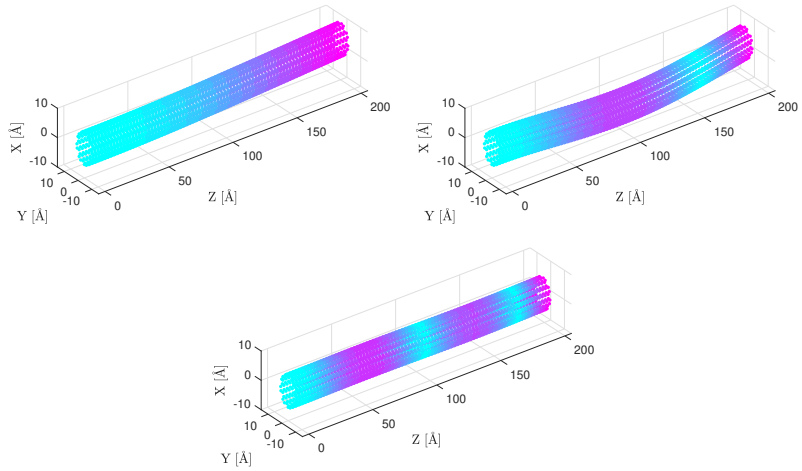

FIGURE A.8: Mode shapes obtained via proper orthogonal decomposition at $T = 50\,\mathrm{K}$. (a) First flexural mode. (b) Second flexural mode. (c) Third flexural mode. Modes are amplified ten times for visualization. Colormap for the norm of x and y displacement.

$$\mathbf{X} = \begin{bmatrix} \mathbf{x}(t_1) & \mathbf{x}(t_2) & \cdots & \mathbf{x}(t_N) \end{bmatrix} = \begin{bmatrix} x_1(t_1) & \cdots & x_1(t_N) \\ \vdots & \ddots & \vdots \\ x_M(t_1) & \cdots & x_M(t_N) \end{bmatrix}, \tag{A.10}$$

where $x_i(t_j)$ is the response of the $i-th$ atom at time t_j. Once matrix $\mathbf{X}$ is constructed, the orthogonal modes are obtained by using the singular-value decomposition (SVD) of the discrete matrix. The SVD operator decomposes $\mathbf{X}$ as:

$$\mathbf{X} = \mathbf{U}\Sigma\mathbf{V}^*, \tag{A.11}$$

where $\mathbf{U}$ is an $M \times M$ real or complex unitary matrix, Σ is a $M \times N$ rectangular diagonal matrix with non-negative real diagonals σ_i that are the singular values of $\mathbf{X}$, and $\mathbf{V}$ is an $N \times N$ real or complex unitary matrix, with $\mathbf{V}^*$ being its conjugate transpose. The columns of $\mathbf{U}$ and $\mathbf{V}$ are the so-called left-singular and right-singular vectors of $\mathbf{X}$, respectively. Among these matrices, $\mathbf{U}$ corresponds to proper orthogonal modes of vibration that can

linearly obtain all the snapshots of the motion with minimum error. Using this matrix we can identify the modes corresponding to the peaks seen in Figure A.7 and report them in Figure A.8.

A.2.2 Quasi-harmonic approximation

The elastic constants of a solid are defined as appropriate derivatives of the free energy with respect to strain tensor components [82]. In particular, the Young's modulus of a nanotube along the axial direction can be computed from:

$$Y(T) = \frac{1}{V_0(T)} \left(\frac{\partial^2 F(T,\epsilon)}{\partial \epsilon^2} \right)_{\epsilon=0}, \tag{A.12}$$

where $F(T,\epsilon)$ is the free energy at temperature T and strain ϵ and $V_0(T)$ is the equilibrium volume at that temperature. It is frequent to assume that the temperature dependence of elastic constants is small and close to their zero-temperature value, which amounts to substituting the internal energy in place of the free energy in Eq. (A.12). However, in this work, we are particularly interested in the temperature-dependence of the Young's modulus. To this end we resort to a quasi-harmonic approximation of the free energy:

$$\begin{aligned} F(T,\epsilon) &\approx F_0(\epsilon) + F_{vib}(T,\epsilon) \\ &\approx F_0(\epsilon) + k_B T \sum_{n\mathbf{k}} \ln \left[2 \sinh \left(\frac{\hbar \omega_{n\mathbf{k}}(\epsilon)}{2 k_B T} \right) \right], \end{aligned} \tag{A.13}$$

where $F_0(\epsilon)$ is the free energy at zero temperature (i.e. the potential energy) at ϵ strain, $\omega_{n\mathbf{k}}(\epsilon)$ is the frequency of vibrational mode n at reciprocal lattice vector $\mathbf{k}$ calculated at strain ϵ. The nanotube phonon frequencies have been calculated using a tight-binding model [189] employing the PHON package [190] (Fig. A.9). From the free energy, we can obtain the temperature-dependent Young's modulus via Eq. (A.12). Our results are compared with experimental measurements in Fig. 5.6.

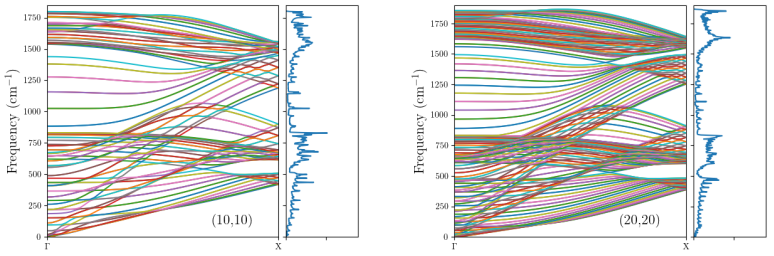

FIGURE A.9: (left) Panel shows the phonon band structure and vibrational density of states for the (10,10) nanotube (see text). (right) panel shows the same information for the (26,0) nanotube.

Bibliography

1. Mertens, H. *et al. Gate-all-around MOSFETs based on vertically stacked horizontal Si nanowires in a replacement metal gate process on bulk Si substrates* in *2016 IEEE Symposium on VLSI Technology* (IEEE, June 2016). https://doi.org/10.1109/vlsit.2016.7573416.
2. Bookholt, A. *iPhone 4 Gyroscope Teardown* https://www.ifixit.com/Teardown/iPhone+4+Gyroscope+Teardown/3156. Accessed: 2021-03-22. 2010.
3. Vijedran, S., Sykulska, H. & Pike, W. T. AFM investigation of Martian soil simulants on micromachined Si substrates. *Journal of Microscopy* **227,** 236–245. https://doi.org/10.1111/j.1365-2818.2007.01806.x (Sept. 2007).
4. Lee, J., Wang, Z., He, K., Shan, J. & Feng, P. X.-L. High Frequency MoS2 Nanomechanical Resonators. *ACS Nano* **7,** 6086–6091. https://doi.org/10.1021/nn4018872 (June 2013).
5. Castellanos-Gomez, A. *et al.* Single-Layer MoS2Mechanical Resonators. *Advanced Materials* **25,** 6719–6723. https://doi.org/10.1002/adma.201303569 (Oct. 2013).
6. Morell, N. *et al.* High Quality Factor Mechanical Resonators Based on WSe2 Monolayers. *Nano Letters* **16,** 5102–5108. https://doi.org/10.1021/acs.nanolett.6b02038 (Aug. 2016).
7. Bunch, J. S. *et al.* Electromechanical Resonators from Graphene Sheets. *Science* **315,** 490–493. https://doi.org/10.1126/science.1136836 (Jan. 2007).
8. Chen, C. *et al.* Performance of monolayer graphene nanomechanical resonators with electrical readout. *Nature Nanotechnology* **4,** 861–867. https://doi.org/10.1038/nnano.2009.267 (Sept. 2009).

9. Eichler, A. *et al.* Nonlinear damping in mechanical resonators made from carbon nanotubes and graphene. *Nature Nanotechnology* **6,** 339–342. https://doi.org/10.1038/nnano.2011.71 (May 2011).

10. Miao, T., Yeom, S., Wang, P., Standley, B. & Bockrath, M. Graphene Nanoelectromechanical Systems as Stochastic-Frequency Oscillators. *Nano Letters* **14,** 2982–2987. https://doi.org/10.1021/nl403936a (May 2014).

11. Singh, V. *et al.* Optomechanical coupling between a multilayer graphene mechanical resonator and a superconducting microwave cavity. *Nature Nanotechnology* **9,** 820–824. https://doi.org/10.1038/nnano.2014.168 (Aug. 2014).

12. Song, X., Oksanen, M., Li, J., Hakonen, P. & Sillanpää, M. Graphene Optomechanics Realized at Microwave Frequencies. *Physical Review Letters* **113.** https://doi.org/10.1103/physrevlett.113.027404 (July 2014).

13. Weber, P., Güttinger, J., Tsioutsios, I., Chang, D. E. & Bachtold, A. Coupling Graphene Mechanical Resonators to Superconducting Microwave Cavities. *Nano Letters* **14,** 2854–2860. https://doi.org/10.1021/nl500879k (Apr. 2014).

14. Cole, R. M. *et al.* Evanescent-Field Optical Readout of Graphene Mechanical Motion at Room Temperature. *Phys. Rev. Applied* **3,** 024004. https://link.aps.org/doi/10.1103/PhysRevApplied.3.024004 (Feb. 2015).

15. Alba, R. D. *et al.* Tunable phonon-cavity coupling in graphene membranes. *Nature Nanotechnology* **11,** 741–746. https://doi.org/10.1038/nnano.2016.86 (June 2016).

16. Mathew, J. P., Patel, R. N., Borah, A., Vijay, R. & Deshmukh, M. M. Dynamical strong coupling and parametric amplification of mechanical modes of graphene drums. *Nature Nanotechnology* **11,** 747–751. https://doi.org/10.1038/nnano.2016.94 (June 2016).

17. Güttinger, J. *et al.* Energy-dependent path of dissipation in nanomechanical resonators. *Nature Nanotechnology* **12,** 631–636. https://doi.org/10.1038/nnano.2017.86 (May 2017).

18. Will, M. *et al.* High Quality Factor Graphene-Based Two-Dimensional Heterostructure Mechanical Resonator. *Nano Letters* **17,** 5950–5955. https://doi.org/10.1021/acs.nanolett.7b01845 (Oct. 2017).
19. Sazonova, V. *et al.* A tunable carbon nanotube electromechanical oscillator. *Nature* **431,** 284–287. https://doi.org/10.1038/nature02905 (Sept. 2004).
20. Lassagne, B., Tarakanov, Y., Kinaret, J., Garcia-Sanchez, D. & Bachtold, A. Coupling Mechanics to Charge Transport in Carbon Nanotube Mechanical Resonators. *Science* **325,** 1107–1110. https://doi.org/10.1126/science.1174290 (July 2009).
21. Steele, G. A. *et al.* Strong Coupling Between Single-Electron Tunneling and Nanomechanical Motion. *Science* **325,** 1103–1107. https://doi.org/10.1126/science.1176076 (July 2009).
22. Gouttenoire, V. *et al.* Digital and FM Demodulation of a Doubly Clamped Single-Walled Carbon-Nanotube Oscillator: Towards a Nanotube Cell Phone. *Small* **6,** 1060–1065. https://doi.org/10.1002/smll.200901984 (Apr. 2010).
23. Chaste, J. *et al.* A Nanomechanical Mass Sensor with Yoctogram Resolution. *Nat Nano* **7,** 301–304 (2012).
24. Stapfner, S. *et al.* Cavity-enhanced optical detection of carbon nanotube Brownian motion. *Applied Physics Letters* **102,** 151910. https://doi.org/10.1063/1.4802746 (Apr. 2013).
25. Moser, J. *et al.* Ultrasensitive force detection with a nanotube mechanical resonator. *Nature Nanotechnology* **8,** 493–496. ISSN: 1748-3395. https://doi.org/10.1038/nnano.2013.97 (2013).
26. Ganzhorn, M. & Wernsdorfer, W. Dynamics and Dissipation Induced by Single-Electron Tunneling in Carbon Nanotube Nanoelectromechanical Systems. *Physical Review Letters* **108.** https://doi.org/10.1103/physrevlett.108.175502 (Apr. 2012).

27. Benyamini, A., Hamo, A., Kusminskiy, S. V., von Oppen, F. & Ilani, S. Real-space tailoring of the electron–phonon coupling in ultraclean nanotube mechanical resonators. *Nature Physics* **10,** 151–156. https://doi.org/10.1038/nphys2842 (Jan. 2014).

28. Tavernarakis, A. *et al.* Optomechanics with a hybrid carbon nanotube resonator. *Nature Communications* **9,** 662. ISSN: 2041-1723. https://doi.org/10.1038/s41467-018-03097-z (Feb. 2018).

29. De Bonis, S. L. *et al.* Ultrasensitive Displacement Noise Measurement of Carbon Nanotube Mechanical Resonators. *Nano Lett.* **18,** 5324–5328. ISSN: 1530-6984. https://doi.org/10.1021/acs.nanolett.8b02437 (Aug. 2018).

30. Khivrich, I., Clerk, A. A. & Ilani, S. Nanomechanical pump–probe measurements of insulating electronic states in a carbon nanotube. *Nature Nanotechnology* **14,** 161–167. https://doi.org/10.1038/s41565-018-0341-6 (Jan. 2019).

31. Ayari, A. *et al.* Self-Oscillations in Field Emission Nanowire Mechanical Resonators: A Nanometric dc-ac Conversion. *Nano Letters* **7,** 2252–2257. https://doi.org/10.1021/nl070742r (Aug. 2007).

32. Gil-Santos, E. *et al.* Nanomechanical mass sensing and stiffness spectrometry based on two-dimensional vibrations of resonant nanowires. *Nature Nanotechnology* **5,** 641. http://dx.doi.org/10.1038/nnano.2010.151 (Aug. 2010).

33. Nichol, J. M., Naibert, T. R., Hemesath, E. R., Lauhon, L. J. & Budakian, R. Nanoscale Fourier-Transform Magnetic Resonance Imaging. *Physical Review X* **3.** https://doi.org/10.1103/physrevx.3.031016 (Sept. 2013).

34. Gloppe, A. *et al. Bidimensional nano-optomechanics and topological backaction in a non-conservative radiation force field* in *2014 International Conference on Optical MEMS and Nanophotonics* (IEEE, Aug. 2014). https://doi.org/10.1109/omn.2014.6924599.

35. Nigùès, A., Siria, A. & Verlot, P. Dynamical backaction cooling with free electrons. *Nature Communications* **6.** https://doi.org/10.1038/ncomms9104 (Sept. 2015).

36. Sansa, M., Fernández-Regúlez, M., Llobet, J., Paulo, Á. S. & Pérez-Murano, F. High-sensitivity linear piezoresistive transduction for nanomechanical beam resonators. *Nature Communications* **5.** https://doi.org/10.1038/ncomms5313 (July 2014).

37. Rossi, N. *et al.* Vectorial scanning force microscopy using a nanowire sensor. *Nature Nanotechnology* **12,** 150. http://dx.doi.org/10.1038/nnano.2016.189 (Oct. 2016).

38. De Lepinay, L. M. *et al.* A universal and ultrasensitive vectorial nanomechanical sensor for imaging 2D force fields. *Nature Nanotechnology* **12,** 156. http://dx.doi.org/10.1038/nnano.2016.193 (Oct. 2016).

39. Hanay, M. S. *et al.* Single-protein nanomechanical mass spectrometry in real time. *Nature Nanotechnology* **7,** 602–608. https://doi.org/10.1038/nnano.2012.119 (Aug. 2012).

40. Wang, Z. *et al.* Phase Transitions of Adsorbed Atoms on the Surface of a Carbon Nanotube. *Science* **327,** 552–555 (2010).

41. Tavernarakis, A. *et al.* Atomic Monolayer Deposition on the Surface of Nanotube Mechanical Resonators. *PRL* **112,** 196103. https://link.aps.org/doi/10.1103/PhysRevLett.112.196103 (May 2014).

42. Losby, J. E. *et al.* Torque-mixing magnetic resonance spectroscopy. *Science* **350,** 798–801. https://doi.org/10.1126/science.aad2449 (Nov. 2015).

43. Mehlin, A. *et al.* Stabilized Skyrmion Phase Detected in MnSi Nanowires by Dynamic Cantilever Magnetometry. *Nano Letters* **15,** 4839–4844. https://doi.org/10.1021/acs.nanolett.5b02232 (June 2015).

44. Thornton, E. A. *Thermal structures for aerospace applications* (American Institute of Aeronautics and Astronautics, 1996).

45. Zudans, Z., Yen, T. C. & Steigelmann, W. H. *Thermal stress techniques in the nuclear industry* (American Elsevier Publishing Company, 1965).

46. Zener, C. Internal Friction in Solids II. General Theory of Thermoelastic Internal Friction. *Phys. Rev.* **53,** 90–99. https://link.aps.org/doi/10.1103/PhysRev.53.90 (1 Jan. 1938).

47. Lifshitz, R. & Roukes, M. L. Thermoelastic damping in micro- and nanomechanical systems. *Phys. Rev. B* **61,** 5600–5609. https://link.aps.org/doi/10.1103/PhysRevB.61.5600 (8 Feb. 2000).

48. Kubo, R. The Fluctuation-Dissipation Theorem. *Rep Prog Phys* **29,** 255 (1966).

49. Cleland, A. N. & Roukes, M. L. Noise Processes in Nanomechanical Resonators. *J Appl Phys* **92,** 2758–2769 (Sept. 2002).

50. Fang, W., Tsai, H.-C. & Lo, C.-Y. Determining thermal expansion coefficients of thin films using micromachined cantilevers. *Sensors and Actuators A: Physical* **77,** 21–27. ISSN: 0924-4247. http://www.sciencedirect.com/science/article/pii/S0924424799000199 (1999).

51. Murozono, M. & Sumi, S. Active Vibration Control of a Flexible Cantilever Beam by Applying Thermal Bending Moment. *Journal of Intelligent Material Systems and Structures* **5,** 21–29. ISSN: 1045-389X. https://doi.org/10.1177/1045389X9400500103 (Jan. 1994).

52. Fugallo, G. *et al.* Thermal Conductivity of Graphene and Graphite: Collective Excitations and Mean Free Paths. *Nano Letters* **14,** 6109–6114. https://doi.org/10.1021/nl502059f (Nov. 2014).

53. Lepri, S. Thermal conduction in classical low-dimensional lattices. *Physics Reports* **377,** 1–80. https://doi.org/10.1016/s0370-1573(02)00558-6 (Apr. 2003).

54. Lindsay, L. *et al.* Phonon thermal transport in strained and unstrained graphene from first principles. *Physical Review B* **89.** https://doi.org/10.1103/physrevb.89.155426 (Apr. 2014).

55. Cepellotti, A. *et al.* Phonon hydrodynamics in two-dimensional materials. *Nature Communications* **6.** https://doi.org/10.1038/ncomms7400 (Mar. 2015).

56. Lee, S., Broido, D., Esfarjani, K. & Chen, G. Hydrodynamic phonon transport in suspended graphene. *Nature Communications* **6.** https://doi.org/10.1038/ncomms7290 (Feb. 2015).

57. Geim, A. K. & Novoselov, K. S. The rise of graphene. *Nature Materials* **6,** 183–191. https://doi.org/10.1038/nmat1849 (Mar. 2007).

58. Cao, Y. *et al.* Unconventional superconductivity in magic-angle graphene superlattices. *Nature* **556,** 43–50. https://doi.org/10.1038/nature26160 (Mar. 2018).

59. Saito, R., Dresselhaus, G. & Dresselhaus, M. S. *Physical Properties of Carbon Nanotubes* https://doi.org/10.1142/p080 (PUBLISHED BY IMPERIAL COLLEGE PRESS AND DISTRIBUTED BY WORLD SCIENTIFIC PUBLISHING CO., July 1998).

60. Iijima, S. Helical microtubules of graphitic carbon. *Nature* **354,** 56–58. https://doi.org/10.1038/354056a0 (Nov. 1991).

61. Zhang, H., Wu, B., Hu, W. & Liu, Y. Separation and/or selective enrichment of single-walled carbon nanotubes based on their electronic properties. *Chem. Soc. Rev.* **40,** 1324–1336. https://doi.org/10.1039/b920457c (2011).

62. Zhao, Q., Nardelli, M. B. & Bernholc, J. Ultimate strength of carbon nanotubes: A theoretical study. *Physical Review B* **65.** https://doi.org/10.1103/physrevb.65.144105 (Mar. 2002).

63. Waissman, J. *et al.* Realization of pristine and locally tunable one-dimensional electron systems in carbon nanotubes. *Nature Nanotechnology* **8,** 569–574. https://doi.org/10.1038/nnano.2013.143 (Aug. 2013).

64. De Bonis, S. L. *et al.* Ultrasensitive Displacement Noise Measurement of Carbon Nanotube Mechanical Resonators. *Nano Letters* **18,** 5324–5328. https://doi.org/10.1021/acs.nanolett.8b02437 (July 2018).

65. Noury, A. *et al.* Layering Transition in Superfluid Helium Adsorbed on a Carbon Nanotube Mechanical Resonator. *Physical Review Letters* **122.** https://doi.org/10.1103/physrevlett.122.165301 (Apr. 2019).

66. Lehman, J. H., Terrones, M., Mansfield, E., Hurst, K. E. & Meunier, V. Evaluating the characteristics of multiwall carbon nanotubes. *Carbon* **49,** 2581–2602. https://doi.org/10.1016/j.carbon.2011.03.028 (July 2011).

67. Ramasubramaniam, A. Large excitonic effects in monolayers of molybdenum and tungsten dichalcogenides. *Physical Review B* **86.** https://doi.org/10.1103/physrevb.86.115409 (Sept. 2012).

68. Novoselov, K. S. *et al.* Two-dimensional atomic crystals. *Proceedings of the National Academy of Sciences* **102,** 10451–10453. https://doi.org/10.1073/pnas.0502848102 (July 2005).

69. Lee, Y.-H. *et al.* Synthesis of Large-Area MoS2Atomic Layers with Chemical Vapor Deposition. *Advanced Materials* **24,** 2320–2325. https://doi.org/10.1002/adma.201104798 (Mar. 2012).

70. Kim, S.-Y., Kwak, J., Ciobanu, C. V. & Kwon, S.-Y. Recent Developments in Controlled Vapor-Phase Growth of 2D Group 6 Transition Metal Dichalcogenides. *Advanced Materials* **31,** 1804939. https://doi.org/10.1002/adma.201804939 (Feb. 2019).

71. Çakır, D., Peeters, F. M. & Sevik, C. Mechanical and thermal properties of TMD monolayers: A comparative study. *Applied Physics Letters* **104,** 203110. https://doi.org/10.1063/1.4879543 (May 2014).

72. Bertolazzi, S., Brivio, J. & Kis, A. Stretching and Breaking of Ultrathin MoS2. *ACS Nano* **5,** 9703–9709. https://doi.org/10.1021/nn203879f (Nov. 2011).

73. Cooper, R. C. *et al.* Nonlinear elastic behavior of two-dimensional molybdenum disulfide. *Physical Review B* **87.** https://doi.org/10.1103/physrevb.87.035423 (Jan. 2013).

74. Kang, M. *et al.* Universal Mechanism of Band-Gap Engineering in Transition-Metal Dichalcogenides. *Nano Letters* **17,** 1610–1615. https://doi.org/10.1021/acs.nanolett.6b04775 (Feb. 2017).

75. Knox, R. S. in *Collective Excitations in Solids* 183–245 (Springer US, 1983). https://doi.org/10.1007/978-1-4684-8878-4_5.

76. Wang, G. *et al.* Colloquium : Excitons in atomically thin transition metal dichalcogenides. *Reviews of Modern Physics* **90.** https://doi.org/10.1103/revmodphys.90.021001 (Apr. 2018).

77. Chernikov, A. *et al.* Electrical Tuning of Exciton Binding Energies in MonolayerWS2. *Physical Review Letters* **115.** https://doi.org/10.1103/physrevlett.115.126802 (Sept. 2015).

78. Ugeda, M. M. *et al.* Giant bandgap renormalization and excitonic effects in a monolayer transition metal dichalcogenide semiconductor. *Nature Materials* **13,** 1091–1095. https://doi.org/10.1038/nmat4061 (Aug. 2014).

79. Ye, Z. *et al.* Probing excitonic dark states in single-layer tungsten disulphide. *Nature* **513,** 214–218. https://doi.org/10.1038/nature13734 (Aug. 2014).

80. Lopez-Sanchez, O., Lembke, D., Kayci, M., Radenovic, A. & Kis, A. Ultrasensitive photodetectors based on monolayer MoS2. *Nature Nanotechnology* **8,** 497–501. https://doi.org/10.1038/nnano.2013.100 (June 2013).

81. Mak, K. F., Lee, C., Hone, J., Shan, J. & Heinz, T. F. Atomically ThinMoS2: A New Direct-Gap Semiconductor. *Physical Review Letters* **105.** https://doi.org/10.1103/physrevlett.105.136805 (Sept. 2010).

82. Landau, L. & Lifshitz, E. *Theory of Elasticity* 3rd (Butterworth-Heinemann Ltd., Oxford, 1986).

83. Poot, M. & van der Zant, H. S. Mechanical systems in the quantum regime. *Physics Reports* **511,** 273–335. https://doi.org/10.1016/j.physrep.2011.12.004 (Feb. 2012).

84. Tsioutsios, I. *Mechanical Resonators Based on Graphene and Carbon Nan- otubes* PhD thesis (Universitat de Autónoma de Barcelona, 2016).

85. Nyquist, H. Thermal Agitation of Electric Charge in Conductors. *Physical Review* **32,** 110–113. https://doi.org/10.1103/physrev.32.110 (July 1928).

86. Brennan, M., Kovacic, I., Carrella, A. & Waters, T. On the jump-up and jump-down frequencies of the Duffing oscillator. *Journal of Sound and Vibration* **318,** 1250–1261. https://doi.org/10.1016/j.jsv.2008.04.032 (Dec. 2008).

87. Lifshitz, R. & Cross, M. C. in *Reviews of Nonlinear Dynamics and Complexity* 1–52 (Wiley-VCH Verlag GmbH & Co. KGaA). https://doi.org/10.1002/9783527626359.ch1.

88. Imboden, M., Williams, O. & Mohanty, P. Nonlinear dissipation in diamond nanoelectromechanical resonators. *Applied Physics Letters* **102,** 103502. https://doi.org/10.1063/1.4794907 (Mar. 2013).

89. Ekinci, K. L. & Roukes, M. L. Nanoelectromechanical systems. *Review of Scientific Instruments* **76,** 061101. https://doi.org/10.1063/1.1927327 (June 2005).

90. Balachandran, B. & Magrab, E. *Vibrations* (Nelson Education, 2008).

91. Morell, N. *et al.* Optomechanical Measurement of Thermal Transport in Two-Dimensional MoSe2 Lattices. *Nano Letters* **19,** 3143–3150. https://doi.org/10.1021/acs.nanolett.9b00560 (Apr. 2019).

92. Chen, C. & Hone, J. Graphene nanoelectromechanical systems. *Proceedings of the IEEE* **101,** 1766–1779. https://doi.org/10.1109/jproc.2013.2253291 (July 2013).

93. Metzger, C. H. & Karrai, K. Cavity cooling of a microlever. *Nature* **432,** 1002–1005. https://doi.org/10.1038/nature03118 (Dec. 2004).

94. Restrepo, J., Gabelli, J., Ciuti, C. & Favero, I. Classical and quantum theory of photothermal cavity cooling of a mechanical oscillator. *Comptes Rendus Physique* **12,** 860–870. https://doi.org/10.1016/j.crhy.2011.02.005 (Dec. 2011).

95. Barton, R. A. *et al.* Photothermal Self-Oscillation and Laser Cooling of Graphene Optomechanical Systems. *Nano Letters* **12,** 4681–4686. https://doi.org/10.1021/nl302036x (Aug. 2012).

96. Metzger, C., Favero, I., Ortlieb, A. & Karrai, K. Optical self cooling of a deformable Fabry-Perot cavity in the classical limit. *Physical Review B* **78.** https://doi.org/10.1103/physrevb.78.035309 (July 2008).

97. Arcizet, O. *Ultrasensitive optical readout and radiation pressure cooling of a micro-mechanical resonator* PhD thesis (2006).

98. Kippenberg, T. J. & Vahala, K. J. Cavity Optomechanics: Back-Action at the Mesoscale. *Science* **321,** 1172–1176. https://doi.org/10.1126/science.1156032 (Aug. 2008).

99. Ramos, D. *et al.* Optomechanics with Silicon Nanowires by Harnessing Confined Electromagnetic Modes. *Nano Letters* **12,** 932–937. https://doi.org/10.1021/nl204002u (Jan. 2012).

100. De Lépinay, L. M. *et al.* A universal and ultrasensitive vectorial nanomechanical sensor for imaging 2D force fields. *Nature Nanotechnology* **12,** 156–162. https://doi.org/10.1038/nnano.2016.193 (Oct. 2016).

101. Treacy, M. M. J., Ebbesen, T. W. & Gibson, J. M. Exceptionally high Young's modulus observed for individual carbon nanotubes. *Nature* **381,** 678–680. https://doi.org/10.1038/381678a0 (June 1996).

102. Babić, B., Furer, J., Sahoo, S., Farhangfar, S. & Schönenberger, C. Intrinsic Thermal Vibrations of Suspended Doubly Clamped Single-Wall Carbon Nanotubes. *Nano Letters* **3,** 1577–1580. https://doi.org/10.1021/nl0344716 (Nov. 2003).

103. Wang, M. C. & Uhlenbeck, G. E. On the Theory of the Brownian Motion II. *Reviews of Modern Physics* **17,** 323–342. https://doi.org/10.1103/revmodphys.17.323 (Apr. 1945).

104. Krishnan, A., Dujardin, E., Ebbesen, T. W., Yianilos, P. N. & Treacy, M. M. J. Young's modulus of single-walled nanotubes. *Physical Review B* **58,** 14013–14019. https://doi.org/10.1103/physrevb.58.14013 (Nov. 1998).

105. Buks, E. & Roukes, M. L. Stiction, adhesion energy, and the Casimir effect in micromechanical systems. *Physical Review B* **63.** https://doi.org/10.1103/physrevb.63.033402 (Jan. 2001).

106. Tsioutsios, I., Tavernarakis, A., Osmond, J., Verlot, P. & Bachtold, A. Real-time measurement of nanotube resonator fluctuations in an electron microscope. *Nano letters* **17,** 1748–1755. https://doi.org/10.1021/acs.nanolett.6b05065 (2017).

107. Wnuk, J. D. *et al.* Electron Induced Surface Reactions of the Organometallic Precursor Trimethyl(methylcyclopentadienyl)platinum(IV). *The Journal of Physical Chemistry C* **113,** 2487–2496. https://doi.org/10.1021/jp807824c (Jan. 2009).

108. Gruber, G. *et al.* Mass sensing for the advanced fabrication of nanomechanical resonators. *Nano letters* **19,** 6987–6992. https://doi.org/10.1021/acs.nanolett.9b02351 (2019).

109. Morell, N. *Optomechanical resonators based on transition metal dichalcogenide monolayers* PhD thesis (ICFO, 2016).

110. Saulson, P. R. Thermal Noise in Mechanical Experiments. *Phys. Rev. D* **42,** 2437–2445 (Oct. 1990).

111. Albrecht, T. R., Grütter, P., Horne, D. & Rugar, D. Frequency Modulation Detection Using High Q Cantilevers for Enhanced Force Microscope Sensitivity. *J Appl Phys* **69,** 668–673 (1991).

112. Barmatz, M., Testardi, L. R. & Di Salvo, F. J. Elasticity measurements in the layered dichalcogenides $TaSe_2$ and $NbSe_2$. *Phys. Rev. B* **12,** 4367–4376. https://link.aps.org/doi/10.1103/PhysRevB.12.4367 (10 Nov. 1975).

113. Brill, J. W. & Roark, W. Electric Field Dependence of Elastic Properties of TaS_3. *Phys. Rev. Lett.* **53,** 846–849. https://link.aps.org/doi/10.1103/PhysRevLett.53.846 (8 Aug. 1984).

114. Hoen, S., Bourne, L. C., Kim, C. M. & Zettl, A. Elastic response of polycrystalline and single-crystal $YBa_2Cu_3O_7$. *Phys. Rev. B* **38,** 11949–11951. https://link.aps.org/doi/10.1103/PhysRevB.38.11949 (16 Dec. 1988).

115. Chiu, H.-Y., Hung, P., Postma, H. W. C. & Bockrath, M. Atomic-Scale Mass Sensing Using Carbon Nanotube Resonators. *Nano Lett* **8,** 4342–4346 (2008).

116. Yeo, I. *et al.* Strain-mediated coupling in a quantum dot-mechanical oscillator hybrid system. *Nature Nanotechnology* **9,** 106. http://dx.doi.org/10.1038/nnano.2013.274 (Dec. 2013).

117. Siria, A. *et al.* Electron Fluctuation Induced Resonance Broadening in Nano Electromechanical Systems: The Origin of Shear Force in Vacuum. *Nano Lett* **12,** 3551–3556 (June 2012).

118. Weber, P., Güttinger, J., Noury, A., Vergara-Cruz, J. & Bachtold, A. Force Sensitivity of Multilayer Graphene Optomechanical Devices. *Nat. Commun.* **7,** 12496 (Aug. 2016).

119. Dolleman, R. J. *et al.* Optomechanics for thermal characterization of suspended graphene. *PRB* **96,** 165421. https://link.aps.org/doi/10.1103/PhysRevB.96.165421 (Oct. 2017).

120. Blaikie, A., Miller, D. & Aleman, B. J. A fast and sensitive room-temperature graphene nanomechanical bolometer. *Nature Communications* **10,** 4726. ISSN: 2041-1723. https://doi.org/10.1038/s41467-019-12562-2 (2019).

121. Rossi, N., Gross, B., Dirnberger, F., Bougeard, D. & Poggio, M. Magnetic Force Sensing Using a Self-Assembled Nanowire. *Nano Lett.* **19,** 930–936. ISSN: 1530-6984. https://doi.org/10.1021/acs.nanolett.8b04174 (Feb. 2019).

122. Sahafi, P. *et al.* Ultralow Dissipation Patterned Silicon Nanowire Arrays for Scanning Probe Microscopy. *Nano Lett.* **20,** 218–223. ISSN: 1530-6984. https://doi.org/10.1021/acs.nanolett.9b03668 (Jan. 2020).

123. Fogliano, F. *et al.* Ultrasensitive nano-optomechanical force sensor at dilution temperatures. *arXiv preprint arXiv:2009.02912* (2020).

124. Lifshitz, R. & Cross, M. C. in *Reviews of Nonlinear Dynamics and Complexity* (ed Schuster, H. G.) 1–52 (Wiley, Weinheim, 2008).

125. Wachtman, J. B., Tefft, W. E., Lam, D. G. & Apstein, C. S. Exponential Temperature Dependence of Young's Modulus for Several Oxides. *Phys. Rev.* **122,** 1754–1759. https://link.aps.org/doi/10.1103/PhysRev.122.1754 (6 June 1961).

126. Salvetat, J.-P. *et al.* Elastic and Shear Moduli of Single-Walled Carbon Nanotube Ropes. *Physical Review Letters* **82,** 944–947. https://doi.org/10.1103/physrevlett.82.944 (Feb. 1999).

127. Lu, J. P. Elastic Properties of Carbon Nanotubes and Nanoropes. *Phys. Rev. Lett.* **79,** 1297–1300. https://link.aps.org/doi/10.1103/PhysRevLett.79.1297 (7 Aug. 1997).

128. Hernández, E., Goze, C., Bernier, P. & Rubio, A. Elastic Properties of C andBxCyNzComposite Nanotubes. *Physical Review Letters* **80,** 4502–4505. https://doi.org/10.1103/physrevlett.80.4502 (May 1998).

129. Sánchez-Portal, D., Artacho, E., Soler, J. M., Rubio, A. & Ordejón, P. Ab initiostructural, elastic, and vibrational properties of carbon nanotubes. *Physical Review B* **59,** 12678–12688. https://doi.org/10.1103/physrevb.59.12678 (May 1999).

130. Robertson, J. Diamond-like amorphous carbon. *Materials Science and Engineering: R: Reports* **37,** 129–281. ISSN: 0927-796X (2002).

131. Yang, Y. T., Callegari, C., Feng, X. L. & Roukes, M. L. Surface Adsorbates Fluctuations and Noise in Nanoelectromechanical Systems. *Nano Lett* **11,** 1753 (2011).

132. Atalaya, J., Kenny, T. W., Roukes, M. L. & Dykman, M. I. Nonlinear damping and dephasing in nanomechanical systems. *Phys. Rev. B* **94,** 195440. https://link.aps.org/doi/10.1103/PhysRevB.94.195440 (19 Nov. 2016).

133. Akhiezer, A. On the Sound Absorption in Solids. *Zh. Eksp. Teor. Fiz* **8,** 1318–1329 (1938).

134. LeRoy, B. J., Lemay, S. G., Kong, J. & Dekker, C. Electrical generation and absorption of phonons in carbon nanotubes. *Nature* **432,** 371–374. ISSN: 1476-4687. https://doi.org/10.1038/nature03046 (Nov. 2004).

135. De Martino, A., Egger, R. & Gogolin, A. O. Phonon-phonon interactions and phonon damping in carbon nanotubes. *Phys. Rev. B* **79,** 205408. https://link.aps.org/doi/10.1103/PhysRevB.79.205408 (20 May 2009).

136. Suzuura, H. & Ando, T. Phonons and electron-phonon scattering in carbon nanotubes. *Phys. Rev. B* **65,** 235412. https://link.aps.org/doi/10.1103/PhysRevB.65.235412 (23 May 2002).

137. Faust, T., Rieger, J., Seitner, M. J., Kotthaus, J. P. & Weig, E. M. Signatures of two-level defects in the temperature-dependent damping of nanomechanical silicon nitride resonators. *Phys. Rev. B* **89,** 100102. https://link.aps.org/doi/10.1103/PhysRevB.89.100102 (10 Mar. 2014).

138. Hamoumi, M. *et al.* Microscopic Nanomechanical Dissipation in Gallium Arsenide Resonators. *Phys. Rev. Lett.* **120,** 223601. https://link.aps.org/doi/10.1103/PhysRevLett.120.223601 (22 May 2018).

139. Vacher, R., Courtens, E. & Foret, M. Anharmonic versus relaxational sound damping in glasses. II. Vitreous silica. *Phys. Rev. B* **72,** 214205. https://link.aps.org/doi/10.1103/PhysRevB.72.214205 (21 Dec. 2005).

140. Rodriguez, J. *et al.* Direct Detection of Akhiezer Damping in a Silicon MEMS Resonator. *Sci. Rep.* **9,** 1–10 (Feb. 2019).

141. Iyer, S. S. & Candler, R. N. Mode- and Direction-Dependent Mechanical Energy Dissipation in Single-Crystal Resonators Due to Anharmonic Phonon-Phonon Scattering. *Phys Rev Appl.* **5,** 034002 (Mar. 2016).

142. Lee, J. *et al.* Electrically tunable single- and few-layer MoS2nanoelectromechanical systems with broad dynamic range. *Science Advances* **4,** eaao6653. https://doi.org/10.1126/sciadv.aao6653 (Mar. 2018).

143. Bleszynski-Jayich, A. C. *et al.* Persistent Currents in Normal Metal Rings. *Science* **326,** 272–275. https://doi.org/10.1126/science.1178139 (Oct. 2009).

144. Schwab, K., Henriksen, E. A., Worlock, J. M. & Roukes, M. L. Measurement of the quantum of thermal conductance. *Nature* **404,** 974–977. https://doi.org/10.1038/35010065 (Apr. 2000).

145. Li, N. *et al.* Colloquium: Phononics: Manipulating heat flow with electronic analogs and beyond. *Reviews of Modern Physics* **84,** 1045–1066. https://doi.org/10.1103/revmodphys.84.1045 (July 2012).

146. Tavakoli, A. *et al.* Heat conduction measurements in ballistic 1D phonon waveguides indicate breakdown of the thermal conductance quantization. *Nature Communications* **9.** https://doi.org/10.1038/s41467-018-06791-0 (Oct. 2018).

147. Bauer, G. E. W., Saitoh, E. & van Wees, B. J. Spin caloritronics. *Nature Materials* **11,** 391–399. https://doi.org/10.1038/nmat3301 (Apr. 2012).

148. Giazotto, F., Heikkilä, T. T., Luukanen, A., Savin, A. M. & Pekola, J. P. Opportunities for mesoscopics in thermometry and refrigeration: Physics and applications. *Reviews of Modern Physics* **78,** 217–274. https://doi.org/10.1103/revmodphys.78.217 (Mar. 2006).

149. Jezouin, S. *et al.* Quantum Limit of Heat Flow Across a Single Electronic Channel. *Science* **342,** 601–604. https://doi.org/10.1126/science.1241912 (Oct. 2013).

150. Pekola, J. P. Towards quantum thermodynamics in electronic circuits. *Nature Physics* **11,** 118–123. https://doi.org/10.1038/nphys3169 (Feb. 2015).

151. Xu, X. *et al.* Length-dependent thermal conductivity in suspended single-layer graphene. *Nature Communications* **5.** https://doi.org/10.1038/ncomms4689 (Apr. 2014).

152. Kim, P., Shi, L., Majumdar, A. & McEuen, P. L. Thermal Transport Measurements of Individual Multiwalled Nanotubes. *Physical Review Letters* **87.** https://doi.org/10.1103/physrevlett.87.215502 (Oct. 2001).

153. Yu, C., Shi, L., Yao, Z., Li, D. & Majumdar, A. Thermal Conductance and Thermopower of an Individual Single-Wall Carbon Nanotube. *Nano Letters* **5,** 1842–1846. https://doi.org/10.1021/nl051044e (Sept. 2005).

154. Balandin, A. A. Thermal properties of graphene and nanostructured carbon materials. *Nature Materials* **10,** 569–581. https://doi.org/10.1038/nmat3064 (July 2011).

155. Yan, R. *et al.* Thermal Conductivity of Monolayer Molybdenum Disulfide Obtained from Temperature-Dependent Raman Spectroscopy. *ACS Nano* **8,** 986–993. https://doi.org/10.1021/nn405826k (Jan. 2014).

156. Balandin, A. A. *et al.* Superior Thermal Conductivity of Single-Layer Graphene. *Nano Letters* **8,** 902–907. https://doi.org/10.1021/nl0731872 (Mar. 2008).

157. Cai, W. *et al.* Thermal Transport in Suspended and Supported Monolayer Graphene Grown by Chemical Vapor Deposition. *Nano Letters* **10,** 1645–1651. https://doi.org/10.1021/nl9041966 (May 2010).

158. Ghosh, S. *et al.* Dimensional crossover of thermal transport in few-layer graphene. *Nature Materials* **9,** 555–558. https://doi.org/10.1038/nmat2753 (May 2010).

159. Faugeras, C. *et al.* Thermal Conductivity of Graphene in Corbino Membrane Geometry. *ACS Nano* **4,** 1889–1892. https://doi.org/10.1021/nn9016229 (Mar. 2010).

160. Lee, J.-U., Yoon, D., Kim, H., Lee, S. W. & Cheong, H. Thermal conductivity of suspended pristine graphene measured by Raman spectroscopy. *Physical Review B* **83.** https://doi.org/10.1103/physrevb.83.081419 (Feb. 2011).

161. Zhang, X. *et al.* Measurement of Lateral and Interfacial Thermal Conductivity of Single- and Bilayer MoS2 and MoSe2 Using Refined Optothermal Raman Technique. *ACS Applied Materials & Interfaces* **7,** 25923–25929. https://doi.org/10.1021/acsami.5b08580 (Nov. 2015).

162. Sledzinska, M. *et al.* Record Low Thermal Conductivity of Polycrystalline MoS2 Films: Tuning the Thermal Conductivity by Grain Orientation. *ACS Applied Materials & Interfaces* **9,** 37905–37911. https://doi.org/10.1021/acsami.7b08811 (Oct. 2017).

163. Ye, F., Lee, J. & Feng, P. X.-L. Electrothermally Tunable Graphene Resonators Operating at Very High Temperature up to 1200 K. *Nano Letters* **18,** 1678–1685. https://doi.org/10.1021/acs.nanolett.7b04685 (Jan. 2018).

164. Shi, L. *et al.* Thermal probing of energy dissipation in current-carrying carbon nanotubes. *Journal of Applied Physics* **105,** 104306. https://doi.org/10.1063/1.3126708 (May 2009).

165. Pumarol, M. E. *et al.* Direct Nanoscale Imaging of Ballistic and Diffusive Thermal Transport in Graphene Nanostructures. *Nano Letters* **12,** 2906–2911. https://doi.org/10.1021/nl3004946 (May 2012).

166. Bae, M.-H. *et al.* Ballistic to diffusive crossover of heat flow in graphene ribbons. *Nature Communications* **4.** https://doi.org/10.1038/ncomms2755 (Apr. 2013).

167. Crossno, J. *et al.* Observation of the Dirac fluid and the breakdown of the Wiedemann-Franz law in graphene. *Science* **351,** 1058–1061. https://doi.org/10.1126/science.aad0343 (Feb. 2016).

168. Efetov, D. K. *et al.* Fast thermal relaxation in cavity-coupled graphene bolometers with a Johnson noise read-out. *Nature Nanotechnology* **13,** 797–801. https://doi.org/10.1038/s41565-018-0169-0 (June 2018).

169. Schwarz, C. *Optomechanical, vibrational and thermal properties of suspended graphene membranes* Theses (Université Grenoble Alpes, Jan. 2016). https://tel.archives-ouvertes.fr/tel-01493121.

170. Castellanos-Gomez, A. *et al.* Deterministic transfer of two-dimensional materials by all-dry viscoelastic stamping. *2D Materials* **1,** 011002. https://doi.org/10.1088/2053-1583/1/1/011002 (Apr. 2014).

171. Ross, J. S. *et al.* Electrical control of neutral and charged excitons in a monolayer semiconductor. *Nature Communications* **4.** https://doi.org/10.1038/ncomms2498 (Feb. 2013).

172. Wang, G. *et al.* Polarization and time-resolved photoluminescence spectroscopy of excitons in MoSe2 monolayers. *Applied Physics Letters* **106,** 112101. https://doi.org/10.1063/1.4916089 (Mar. 2015).

173. Fugallo, G., Lazzeri, M., Paulatto, L. & Mauri, F. Ab initio variational approach for evaluating lattice thermal conductivity. *Physical Review B* **88.** https://doi.org/10.1103/physrevb.88.045430 (July 2013).

174. Taube, A., Judek, J., Łapińska, A. & Zdrojek, M. Temperature-Dependent Thermal Properties of Supported MoS2 Monolayers. *ACS Applied Materials & Interfaces* **7,** 5061–5065. https://doi.org/10.1021/acsami.5b00690 (Feb. 2015).

175. Hone, J. Quantized Phonon Spectrum of Single-Wall Carbon Nanotubes. *Science* **289,** 1730–1733. https://doi.org/10.1126/science.289.5485.1730 (Sept. 2000).

176. Kiwia, H. L. & Westrum, E. F. Low-temperature heat capacities of molybdenum diselenide and ditelluride. *The Journal of Chemical Thermodynamics* **7,** 683–691. https://doi.org/10.1016/0021-9614(75)90009-9 (July 1975).

177. Johnson, J. A. *et al.* Direct Measurement of Room-Temperature Nondiffusive Thermal Transport Over Micron Distances in a Silicon Membrane. *Physical Review Letters* **110.** https://doi.org/10.1103/physrevlett.110.025901 (Jan. 2013).

178. Cepellotti, A. & Marzari, N. Boltzmann Transport in Nanostructures as a Friction Effect. *Nano Letters* **17,** 4675–4682. https://doi.org/10.1021/acs.nanolett.7b01202 (July 2017).

179. Islam, A., van den Akker, A. & Feng, P. X.-L. Anisotropic Thermal Conductivity of Suspended Black Phosphorus Probed by Opto-Thermomechanical Resonance Spectromicroscopy. *Nano Letters* **18,** 7683–7691. https://doi.org/10.1021/acs.nanolett.8b03333 (Oct. 2018).

180. Melcher, J., Hu, S. & Raman, A. Equivalent point-mass models of continuous atomic force microscope probes. *Applied Physics Letters* **91,** 053101 (2007).

181. Plimpton, S., Crozier, P. & Thompson, A. LAMMPS-large-scale atomic/molecular massively parallel simulator. Sandia National Laboratories 18 (2007) (2007).

182. Tersoff, J. New empirical approach for the structure and energy of covalent systems. *Phys. Rev. B* **37,** 6991–7000. https://link.aps.org/doi/10.1103/PhysRevB.37.6991 (12 Apr. 1988).

183. Lindsay, L. & Broido, D. A. Optimized Tersoff and Brenner empirical potential parameters for lattice dynamics and phonon thermal transport in carbon nanotubes and graphene. *Phys. Rev. B* **81,** 205441. https://link.aps.org/doi/10.1103/PhysRevB.81.205441 (20 May 2010).

184. Tang, C., Guo, W. & Chen, C. Molecular dynamics simulation of tensile elongation of carbon nanotubes: Temperature and size effects. *Phys. Rev. B* **79,** 155436. https://link.aps.org/doi/10.1103/PhysRevB.79.155436 (15 Apr. 2009).

185. Yakobson, B. I., Brabec, C. J. & Bernholc, J. Nanomechanics of Carbon Tubes: Instabilities beyond Linear Response. *Phys. Rev. Lett.* **76,** 2511–2514. https://link.aps.org/doi/10.1103/PhysRevLett.76.2511 (14 Apr. 1996).

186. Klessig, R. & Polak, E. Efficient Implementations of the Polak–Ribière Conjugate Gradient Algorithm. *SIAM Journal on Control* **10,** 524–549 (1972).

187. Evans, D. J. & Holian, B. L. The Nose–Hoover thermostat. *The Journal of Chemical Physics* **83,** 4069–4074 (1985).

188. Sajadi, B. *et al.* Nonlinear dynamic identification of graphene's elastic modulus via reduced order modeling of atomistic simulations. *Journal of the Mechanics and Physics of Solids* **122,** 161–176. `http://www.sciencedirect.com/science/article/pii/S0022509618305180` (2019).

189. Porezag, D., Th., F., Köhler, T., Seifert, G. & Kraschner, R. Construction of tight-binding-like potentials on the basis of density-functional theory: Application to carbon. *Physical Review B* **51,** 12947–12957 (1995).

190. Alfè, D. PHON: A program to calculate phonons using the small displacement method. *Computer Physics Communications* **180,** 12947–2633 (2009).